Thesis for the degree

Doctor of Philosophy

Submitted to the Scientific Council of

the

Weizmann Institute of Science

עבודת גמר (תזה) לתואר

דוקטור לפילוסופיה

מוגשת למועצה המדעית של

מכון ויצמן למדע

רחובות, ישראל

By

Dorri Halbertal

מאת

דורי הלברטל

דימות תרמי של דיסיפציה במערכות קוונטיות

Nanoscale thermal imaging of dissipation in quantum systems

Advisor:

Prof. Eli Zeldov

מנחה:

פרופ' אלי זלדוב

May 2017

אייר תשע"ז

Acknowledgments

I would like to express my gratitude to my advisor, Prof. Eli Zeldov, from whom I've learnt all I know about experimental condensed matter physics. Whenever we reached a wall, he was somehow able to carve a door and proceed.

I thank Dr. Lior Embon who closely guided me in the early clueless days, and whose expertly designed microscope enabled the work. Dr. Yonathan Anahory enabled the Pb SOT technology and provided his expert guidance and friendship along the way. Dr. Jo Cuppens joined me at the early uncertain days of developing the SQUID based thermometry, when it was a mere shot in the dark.

I would also like to thank Yuval Ronen, who came to the rescue at a crucial point, and helped to win the greatest battle of my PhD.

I thank Dr. Yuri Myasoedov and Dr. Michael Rappaport on whom I could always rely to come up with a creative solution to any technical problem.

I thank my collaborators Dr. Moshe Ben-Shalom, John Birkbeck and Prof. Andre Geim, Prof. Leonid Levitov, Dr. Nitzan Shadmi and Prof. Ernesto Joselevich whose expertise pushed us to the frontier of science.

Throughout this long journey I had the pleasure of working with a long list of great people of our group: Aviram Uri, Dr. Ella Lachman, Dr. Denis Vasyukov, Dr. Naren R Hoovinakatte, Dr. Jayanta Sarkar, Dr. Kousik Bagani, Dr. Alexander Meltzer, Ido Marcus, Elad Yaakobi, Jonathan Drori and Jonathan Reiner, from whom I have learnt much, enjoyed their company and will cherish our adventures.

I would also like to express my gratitude to the members of the Physics Instrumentation workshop and the department's staff for support of our scientific efforts while creating a warm work environment.

Last but not least, I thank my wife, Nina, who walked along me during the good and the bad. I doubt I could have reached this point without her support and encouragement.

Declaration

This work summarizes my independent research. However, this work is a result of collaborations with lab-members as well as external collaborators, as listed below.

SOT scanning microscopy: The scanning SOT microscope and the vibration isolation system were designed and realized by Dr. Lior Embon. Dr. Yonathan Anahory developed the Pb SOT fabrication technique with the assistance of Drs. Denis Vasyukov, Yuri Myassoedov and Michael Rappaport. Elaad Yaacoby investigated the concept of deposition of a shunt resistor in the vicinity of the apex of the SOT. The SSAA was fabricated in NIST by Prof. Martin E. Huber from the University of Colorado, Denver. The feedback electronics were originally designed by Prof. John M. Martinis and modified by Prof. Huber. The Pb-tSOT tuning-fork based height control was developed by Aviram Uri, Dr. Yuri Myasoedov and the author (following earlier attempts by Dr. Embon and Dr. Amit Finkler).

Sample fabrication: Dr. Moshe Ben Shalom and Prof. Andre K. Geim of the University of Manchester provided the hBN encapsulated graphene samples used in this work (part II). Dr. Nitzan Shadmi and Prof. Ernesto Joselevich fabricated the CNT samples (section 3.3). Dr. Jo Cuppens fabricated the Cu/Py sample (used for thermal measurement throughout section 3.2) with facilitation of Dr. Marius V. Costache and Prof. Sergio O. Valenzuela at ICN2, Barcelona. Dr. HR Naren, Dr. Jayanta Sarkar and the author fabricated the a:In_2O_3 sample with assistance and facilitation from Prof. Dan Shahar (3.2.4). Yuval Ronen and the author designed and fabricated the spatial resolution demonstration sample (section 3.2.5).

Device fabrication: tSOT sensors throughout the work were fabricated by Dr. HR Naren, Dr. Yonathan Anahory, Aviram Uri and Dr. Kousik Bagani.

The tSOT technique was conceived by the author together with Dr. Jo Cuppens and Prof. Eli Zeldov.

Experiments: All experiments were conceived and designed by the author and Prof. Zeldov. All experiments were performed by the author. All data analysis was done by the author with the exception of the bell-shape reconstruction of Figure A7b performed by Dr. Alex Meltzer. Mia Solodky assisted with manual reconstruction.

Theory: Prof. Leonid S. Levitov of MIT performed parts of the theoretical analysis, and contributed to understanding of the thermal model of the tSOT.

Table of Contents

Acknowledgments 2

Declaration 3

Table of Contents 4

List of Figures 6

List of Abbreviations 7

1 Abstract 8

2 Hebrew abstract 9

3 Part I – nanoscale scanning SQUID on tip thermometry 10

3.1 Introduction 10

3.2 Methods 13

3.2.1 Device fabrication 13

3.2.2 tSOT thermal properties and characterization 14

3.2.3 Utilization for scanning 15

3.2.4 Correlation between the sample and tSOT temperatures 16

3.2.5 Spatial resolution 19

3.2.6 Demonstration of tSOT temperature sensitivity 28

3.2.7 Simultaneous magnetic and thermal imaging 29

3.2.8 Bandwidth of the tSOT thermal imaging 31

3.2.9 Approaching the sample 32

3.2.10 Tuning-fork based height control 33

3.2.11 tSOT heater measurement mode 34

3.3 Results - Thermal imaging of dissipation in Carbon nanotube devices 37

3.4 Discussion 39

4 Part II - Imaging and controlling dissipation from individual atomic defects in graphene 41

4.1 Introduction 41
4.2 Methods 42
4.2.1 Sample fabrication 42
4.2.2 Characterization of tSOT device used for part II 43
4.2.3 Thermal imaging schemes 45
4.3 Results 47
4.3.1 Dissipation sources in a graphene heterostructure 47
4.3.2 Dissipative localized states in graphene heterostructures 49
4.4 Discussion 54
4.4.1 Derivation of local CNP and of energy level of bulk localized state 54
4.4.2 Derivation of the LDOS of the localized state 57
4.4.3 Summary of conclusions regarding localized states in graphene heterostructures 59
4.4.4 Prevalence of localized states at the edges of graphene structures 60
4.4.5 Summary 61
Appendix 1: Thermodynamic limit of the thermal noise 62
Appendix 2: Assessment of thermal resistances of the tSOT 64
Appendix 3: Carbon nanotube fabrication 68
Appendix 4: Ring-like patterns in scanning gate thermometry due to localized states 69
Appendix 5: Simulations of the electrostatic interaction between the tSOT and the sample 73
Appendix 6: Search for additional energy levels of a localized state 76
Appendix 7: Analysis of localized states along the graphene edges 78
5 Bibliography 80
6 List of publications derived from the doctoral research 86

List of Figures

Figure 1 | tSOT characteristics and performance. 11
Figure 2 | Characteristics of the 46 nm diameter tSOT. 15
Figure 3 | Comparison between the sample and tSOT temperatures. 18
Figure 4 | Theoretical analysis of the spatial resolution of tSOT. 21
Figure 5 | Comparison of heat profiles above a 1D heater: simulation vs. experimental results. 22
Figure 6 | Experimental demonstration of spatial resolution of tSOT. 25
Figure 7 | Theoretical comparison of different heating schemes. 27
Figure 8 | Demonstration of tSOT temperature sensitivity. 29
Figure 9 | Simultaneous scanning tSOT thermal and magnetic imaging. 31
Figure 10 | Bandwidth characterization of the tSOT. 32
Figure 11 | Quartz crystal tuning fork resonator for tSOT height control. 34
Figure 12 | tSOT heater measurement mode: Resolving topography. 35
Figure 13 | tSOT heater measurement of graphene. 36
Figure 14 | Thermal imaging of single-walled carbon nanotubes and scanning gate thermometry of quantum dots. 38
Figure 15 | Thermal imaging by scanning *ac* gate thermometry of quantum dot dissipation in SWCNT. 39
Figure 16 | Magneto transport characterization of the graphene sample. 43
Figure 17 | tSOT of part II characterization. 45
Figure 18 | Demonstration of simultaneous measurement by three thermal imaging methods. 47
Figure 19 | Observing individual dissipation sources in a graphene heterostructure. 48
Figure 20 | Thermal imaging of resonant dissipation of three bulk localized states. 49
Figure 21 | Thermal nanospectroscopy of dissipative localized states. 50
Figure 22 | Origin of the resonant ring structures. 52
Figure 23 | Thermal spectroscopy of a single localized state. 53
Figure 24 | Numerical simulation of resonance lines of LS. 55
Figure 25 | Calculated and measured resonance lines of LS. 56
Figure 26 | Estimating the spectral width of the localized state. 58
Figure 27 | Thermal spectroscopy of individual edge localized states. 60

List of Abbreviations

SQUID – Superconducting Quantum Interference Device.

SOT – SQUID On Tip.

tSOT – SQUID On Tip Thermometer.

SSAA – SQUID Series Array Amplifier.

(SW)CNT – (Single Walled) Carbon Nanotube.

hBN – Hexagonal Boron Nitride.

Gr – Graphene.

SPM – Scanning Probe Microscopy.

Py – Permalloy.

LIA – Lock-in Amplifier.

IR – Infrared.

SNOM – Scanning Near-field Optical Microscopy.

TEM – Transmission Electron Microscopy.

SEM – Scanning Electron Microscopy.

SThM – Scanning Thermal Microscopy.

STM – Scanning Tunneling Microscopy.

TF – Tuning Fork.

CNP – Charge Neutrality Point.

LS – Localized State.

LDOS – Local Density of States.

1 Abstract

Energy dissipation is a fundamental process governing the dynamics of physical systems. In condensed matter physics, in particular, scattering mechanisms, loss of quantum information, or breakdown of topological protection are deeply rooted in the intricate details of how and where the dissipation occurs. Despite its vital importance the microscopic behavior of a system is usually not formulated in terms of dissipation because the latter is not a readily measureable quantity on the microscale. While the motivation is clear, existing thermal imaging methods lack the necessary sensitivity and are unsuitable for low temperature operation required for study of quantum systems[1–15].

In Part I of this research a novel technique for imaging of dissipation has been developed. It provides a thermal sensitivity of less than 1 $\frac{\mu K}{\sqrt{Hz}}$ with a sub 50 nm spatial resolution. The non-contact non-invasive thermometry scheme allows thermal imaging of very low nanoscale energy dissipation down to the fundamental Landauer limit[16–18] of 40 fW for continuous readout of a single qubit at 1 GHz at 4.2 K. Furthermore, it is optimal for low temperature applications. These advances enabled the observation of dissipation due to single electron charging of individual quantum dots in carbon nanotubes, opening the door to direct imaging of nanoscale dissipation processes in quantum matter.

Conversion of electric current into heat involves microscopic processes that operate on nanometer length scales and release minute amounts of power. While central to our understanding of the electrical properties of materials, individual mediators of energy dissipation have so far eluded direct examination. In Part II of this research, we utilized the novel dissipation imaging technique to visualize and control the local release of heat, by manipulating individual atomic defects and identifying the dominant dissipation pathway in ballistic graphene. We directly observed resonant inelastic scattering at such defects and determined their spectral characteristics. Originating from highly-localized states near the Dirac point, the defects act as switchable phonon emitters providing energy sinks when the Fermi level comes in resonance with defects' energy levels. This work (Part II) offers new insights for addressing key materials challenges in modern electronics and engineering dissipation at the nanoscale.

2 Hebrew abstract

פיזור אנרגיה הוא תהליך בסיסי השולט בדינמיקה של מערכות פיזיקליות. בפיסיקה של חומר מעובה, בפרט, תהליכי פיזור, אובדן מידע קוונטי, או קריסה של ההגנה הטופולוגית מושרשים עמוק בפרטים המורכבים של היכן ובאיזה אופן פיזור החום מתרחש. למרות חשיבותו, התיאור המיקרוסקופי של מערכת לרוב איננו מנוסח במונחים של פיזור חום, שכן גודל זה איננו ניתן למדידה בסקלה המיקרוסקופית. בעוד המוטיבציה ברורה, שיטות הדמיה תרמית קיימות חסרות את הרגישות הנדרשת וכמו כן, אינן מתאימות לפעולה בטמפרטורה נמוכה הנדרשת לחקר מערכות קוונטיות.

בחלקו הראשון של המחקר פותחה טכניקה חדשה להדמיה של פיזור חום. הטכניקה מספקת רגישות תרמית של פחות מ- $1\ \frac{\mu K}{\sqrt{Hz}}$ עם רזולוציה מרחבית של פחות מ- 50 ננומטר. הסריקה מתבצעת שלא במגע פיזי, היא לא פולשנית ומאפשרת ליצור הדמיה תרמית של רמות פיזור חום נמוכות מאוד בסקלה הננומטרית עד לחסם התיאורטי הבסיסי של גבול לנדאור של 40 fW עבור קריאה רציפה של ביט קוונטי יחיד בתדר של GHz בטמפרטורה של הליום נוזלי. בנוסף, ההתקן אופטימלי עבור יישומים בטמפרטורות נמוכות. התקדמות זו אפשרה תצפית של פיזור חום בעקבות מעברים הכוללים אלקטרון בודד בנקודות קוונטיות בננו-צינוריות פחמן. פיתוח זה סולל את הדרך להדמיה ישירה של תהליכי פיזור חום בסקלה הננומטרית במערכות קוונטיות.

ההמרה של זרם חשמלי לחום כרוכה בתהליכים מיקרוסקופיים שפועלים בסקלה ננומטרית ובשחרור כמויות מזעריות של הספק. למרות היותם מרכזיים להבנת התכונות החשמליות של חומרים, מתווכים בודדים של פיזור חום לא היו נגישים עד כה למדידה ישירה. בחלקו השני של מחקר זה, השתמשנו בטכניקה החדשנית שפתחנו להדמיית פיזור חום כדי לדמות ואף לשלוט על פיזור חום מקומי. זאת, על ידי מניפולציה של פגמים אטומיים בודדים וזיהוי מסלולי פיזור החום המרכזיים בהתקן של גרפן בליסטי. מדדנו באופן ישיר פיזור לא-אלסטי המאופיין במצבי תהודה כתוצאה מפיזור בפגמים כאלו, ואפיינו את התכונות הספקטרליות שלהם. הפגמים הללו יוצרים מצבים אלקטרוניים מאוד ממוקמים בקרבת נקודת דיראק, ומהווים מקורות פונונים, שמהווים מסלול לפיזור אנרגית אלקטרונים, אשר נדלקים כאשר מתקיימים תנאי תהודה בין האלקטרונים לרמות האנרגיה של המצבים הממוקמים. חלקה השני של עבודה זו מציע תובנות חדשות להתמודדות עם אתגרים מרכזיים בתחומי מדע החומרים עבור אלקטרוניקה מודרנית, ועבור הנדסה של פיזור חום בסקלה הננומטרית.

3 Part I – nanoscale scanning SQUID on tip thermometry

3.1 Introduction

Investigation of energy dissipation on the nanoscale is of major fundamental interest for a wide range of disciplines, ranging from biological processes, through chemical reactions, to energy-efficient computing[1–5]. Study of dissipation mechanisms in quantum systems is of particular importance because dissipation demolishes quantum information. In order to preserve a quantum state, the dissipation has to be extremely weak and hence hard to measure. As a figure of merit for detection of low-power dissipation in quantum systems[16], we consider an ideal qubit operating at a typical read-out frequency of 1 GHz. Landauer's principle states that the lowest bound on energy dissipation in an irreversible qubit operation is $E_0 = k_B T \ln 2$, where k_B is Boltzmann's constant and T is the temperature[17,18]. At $T = 4.2$ K, $E_0 = 4 \times 10^{-23}$ J, several orders of magnitude below both the 10^{-19} J of dissipation per logical operation in present-day superconducting electronics and the 10^{-15} J in CMOS devices[19,20]. Hence the power dissipated by an ideal qubit operating at a read-out rate of $f = 1$ GHz will be as low as $P = E_0 f = 40.2$ fW. The resulting temperature increase of the qubit will depend on its size and the thermal properties of the substrate. For example, a 120 nm × 120 nm device on a 1-µm-thick SiO_2/Si substrate dissipating 40 fW will heat up by about 3 µK (Figure 1). Such signals are several orders of magnitude below the best sensitivity (several mK $Hz^{-1/2}$) of any of the existing imaging techniques[1–15] (Figure 1a), including radiation-based thermometry using infrared (IR), fluorescence in nanodiamonds[4,7,8], Raman spectroscopy[9], scanning near-field optical microscopy[10] (SNOM), or the electron beam induced plasmons in transmission electron microscopy[5] (TEM), and atomic force microscopy (AFM) equipped with thermocouple (TC SThM) or resistive (Res. SThM) thermometers[10–15,21–24]. Moreover, none of the existing imaging techniques has been demonstrated to operate at the low temperatures that are essential for study of quantum systems.

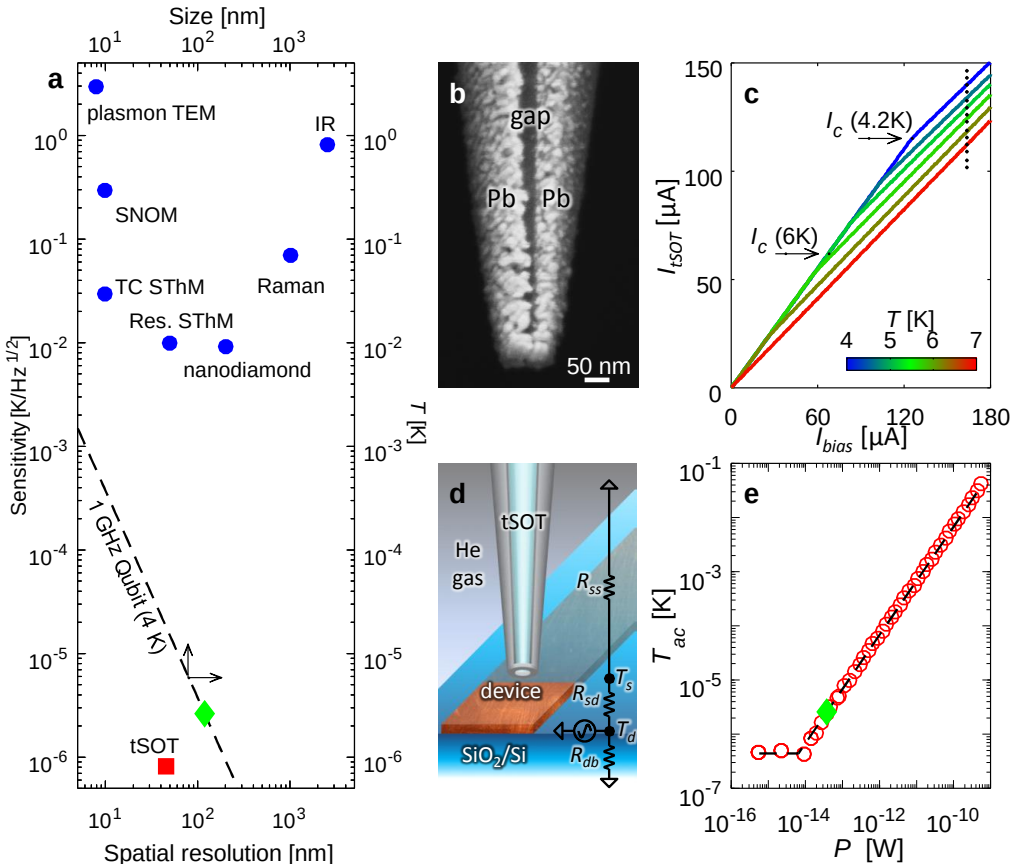

Figure 1 | tSOT characteristics and performance.

a, Sensitivities of different thermal imaging techniques (blue) and of the tSOT (red) vs. their spatial resolution (bottom-left axes). Green diamond: the measured temperature increase due to 40 fW dissipation (taken from (**e**)) corresponding to Landauer's limit for qubit operation at 4.2 K at 1 GHz along with the theoretical scaling of the temperature with the qubit size (dashed line, top-right axes). **b**, SEM image of the 46 nm effective diameter Pb tSOT. **c**, Electrical characteristics of the tSOT for temperatures ranging from 4.2 K to 7.2 K with marked values of the critical current I_c at representative temperatures. **d**, Schematic drawing of the measurement setup and a simplified effective thermal circuit. **e**, Measurement of the tSOT temperature T_{ac} at 13.1 kHz above a 120 nm wide Cu nanowire with sheet resistance 0.46 Ω/□ vs. the ac power P dissipated by a variable I_{ac} in 120×120 nm^2 unit segment of the nanowire. The dashed line shows a linear fit (with slope $R_{db} = 6.8\times10^7$ K/W) and a noise floor of $T_{ac} \simeq 440$ nK below $P \simeq 6$ fW using lock-in amplifier time constant of 1 sec.

On a more fundamental level, when discussing nanoscale scanning thermal imaging, in which a thermal probe attempts to provide a local thermal measurement, the notion of temperature itself is not well-defined. This is especially true if the measured system itself is perturbed out of equilibrium. The naive definition of a local temperature, which is commonly used in molecular dynamics simulations, would be to extract it from the kinetic energy averaged over some volume. This definition is problematic in

our case, both because of its assumptions on the quadratic form of the energy, but also because it assumes a smooth temperature on some length-scale. More commonly considered approaches, as described in a recent review on the subject[25], consider an external probe that couples to a local region of a sample, and define the local temperature of the sample according to some minimal disturbance conditions by the probe. In most of the reviewed approaches the probe is considered as a bath, which locally couples to the system. The temperature of the bath is tuned as to minimize heat flux to the system. The local temperature is then defined as the required temperature to reach this condition[25]. The approaches differ by the nature of the coupling between the bath and the system and the nature of the bath itself. This definition for the local temperature suffers from being system and coupling dependent, but is still characteristic of dissipative processes within the sample under inspection. However, this argument currently is mostly philosophical, since all leading SThM techniques, with the exception of a rarely used concept of the null-point SThM method[26] (which directly follows along the above lines by nulling heat transport through probe), scan under strongly out-of-equilibrium conditions between the probe and sample. The concept of a scanning thermal probe which is in local thermal equilibrium with a sample region was not realized prior to this work.

Superconducting junctions are commonly used as highly sensitive thermometers[2,27], relying on the strong temperature dependence of their critical current $I_c(T)$, which in the vicinity of the critical temperature T_c can be approximated by $I_c(T) \approx I_0(1 - T/T_c)$. Conventional junction configurations, however, are not suitable for scanning probe thermometry owing to their planar geometry and strong thermal coupling to the substrate.

In this work we introduced a non-contact cryogenic scanning probe microscopy technique based on a superconducting quantum interference device (SQUID) positioned on a tip[28,29]. We utilized a novel approach in which either a single Pb (T_c = 7.2 K) superconducting junction or a SQUID is fabricated on the apex of a sharp quartz pipette (SQUID on tip, SOT**)** and can be made as small as a few tens of nanometers in diameter. The first part of the research aimed at utilizing the SOT technology, which was previously reported and used for magnetometry[28,29], into the world of scanning thermal microscopy, which would be applicable to probe quantum states of matter, and to reveal new insights about dissipation processes in systems of condensed matter physics.

As a derivative of this goal we had to address several sub-goals:

- Developing a highly sensitive thermometer of nanoscale resolution which can be used for scanning, and which is optimal for the low temperature required for most applications. No previously existing technique has even remotely sufficient sensitivity and none is applicable, even in principle to cryogenic temperatures (as a figure of merit <10 K).
- Coupling the thermometer to a sample: The thermometer has to be thermally coupled to the sample, such that it is in thermal equilibrium with a local sample region. Only under such a condition its reading would resemble the sample's local temperature, while minimally affecting the sample (a non-invasive sensor). All previously existing scanning probe thermal imaging technologies fail miserably in this aspect.

Part I describes the scanning SOT thermometer (tSOT) along the lines of Ref. [30].

3.2 Methods

3.2.1 Device fabrication

The tSOT fabrication methods, as well as the measurement circuitry and readout techniques, are based on the SOT technology[28,29,31] with several modifications. The tSOTs are fabricated by self-aligned three stage in-situ Pb deposition onto a pulled quartz pipette with apex diameter between 40 and 300 nm cooled to about 8 K. Pb has a very high surface diffusion and as a result grows in a form of isolated islands if deposited at room temperature or even at 77 K. A low temperature deposition is therefore required in order to attain sufficiently uniform thin Pb films on the surface of the quartz pipettes as described in Ref. 28.

Figure 1b shows a scanning electron microscopy (SEM) image of a thermometer using this SQUID-on-tip technique (a tSOT) with an effective diameter of 46 nm, as determined from its quantum interference pattern. Similar SOT devices have previously been reported[28,29] to be extremely sensitive magnetic sensors, reaching a magnetic spin sensitivity below 0.4 μ_B $Hz^{-1/2}$.

The two main modifications in tSOT fabrication are the use of grooved quartz tubes, which facilitate reliable fabrication of small tSOTs, and deposition of an integrated Au shunt resistor in the vicinity of the apex, which adds damping resulting in linear characteristics above I_c (Figure 1c) that are advantageous for thermal imaging.

3.2.2 tSOT thermal properties and characterization

Figure 2 shows the characteristics of the tSOT device used for the measurements in Figure 1. The tSOT effective diameter of 46 nm was extracted from the interference pattern as in Ref. 28. The current through the sensor I_{tSOT} is measured using a SQUID series array amplifier (SSAA)[32] as shown in the inset of Figure 2c. The electrical characteristics of the tSOT (Figure 1c) show the current through the sensor (I_{tSOT}) versus externally applied bias current (I_{bias}) at various temperatures (see electrical diagram in Figure 2c). Figure 2a presents a set of 200 I_{tSOT} vs. I_{bias} curves at different temperatures T, color-coded between 4.2 K and $T_c = 7.2$ K, showing the monotonous decrease of I_c with temperature.

For $I_{\mathrm{tSOT}} < I_{\mathrm{c}}$, essentially all the applied current flows through the tSOT, while at higher bias a substantial part of the current diverts to a parallel shunt resistor.

When biasing the tSOT at a fixed I_{bias} =160 μA > I_{c} (dashed line in Figure 1c), the temperature dependence of $I_{\mathrm{tSOT}}(T)$ gives rise to a thermal response $\mathrm{d}I_{\mathrm{tSOT}}/\mathrm{d}T = -9.5\ \mu\mathrm{A\ K}^{-1}$ at the base temperature (Figure 2b); when this is combined with the very low white noise of the tSOT ($S_I^{1/2} = 8.3\ \mathrm{pA\ Hz}^{-1/2}$; Figure 2c) it translates into a remarkably low thermal noise of $S_T^{1/2} = 870\ \mathrm{nK\ Hz}^{-1/2}$, an improvement of four orders of magnitude over existing thermal imaging methods (Figure 1a). This remarkable number is still about 2 orders of magnitude larger than the thermodynamic limit for the thermal sensitivity (see Appendix 1), allowing further improvement. Figure 2d shows the thermal noise vs. the temperature attained by measuring the noise spectra and the thermal response at various temperatures. This result demonstrates that the tSOT can operate over a wide temperature range, up to 7 K, with outstanding thermal sensitivity, down to 600 nK/Hz$^{1/2}$. Very close to T_c the thermal noise diverges due to a decrease in the thermal response. In general, the most sensitive temperature range of the tSOT is $\sim T_c/2 < T < T_c$ where the critical current has an approximately linear T dependence $I_c(T) \cong I_0(1 - T/T_c)$. At lower temperatures the $|dI_c(T)/dT|$ usually decreases and hence the sensitivity is expected to drop. This limitation can be readily addressed by using SOTs made of lower T_c superconductors including Al [29] and In [33].

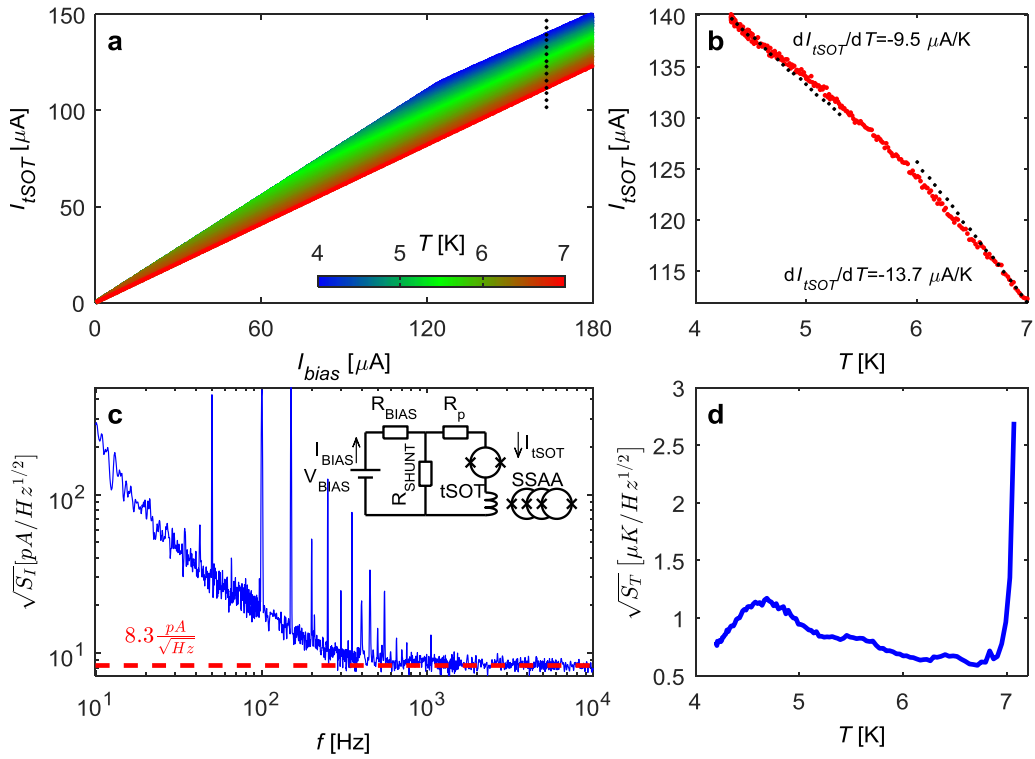

Figure 2 | Characteristics of the 46 nm diameter tSOT.

a, Set of 200 I_{tSOT} vs. I_{bias} characteristics at various temperatures T color coded from 4.2 to 7 K. **b**, Monotonically decreasing I_{tSOT} vs. T for $I_{bias} = 160$ μA giving rise to thermal response of –9.5 μA/K at the base temperature and –13.7 μA/K close to T_c. **c**, tSOT current noise spectral density at the working point at 4.2 K reaching a white noise level of 8.3 pA/Hz$^{1/2}$. Inset: schematics of the measurement circuit. **d**, Thermal noise as a function of temperature showing the very high thermal sensitivity of the tSOT in the entire range of temperatures up to 7 K.

3.2.3 Utilization for scanning

To enable effective thermal imaging, the thermal properties of the sensor, including its coupling to the sample, are crucial. For non-invasive imaging, the thermal resistance between the sensor and the investigated device, R_{sd}, has to be considerably larger than the thermal resistance between the device and the bulk of its substrate, R_{db} (Figure 1d). On the other hand, in order for the temperature of the sensor T_s to accurately describe the local temperature of the device T_d, a high thermal resistance R_{ss} is required between the sensor and its support structure. The resulting overall requirement of $R_{ss} \gg R_{sd} \gg R_{db}$ is usually hard to achieve in AFM-type scanning thermal probes[12], leading to invasive in-contact imaging[13,14]. In a tSOT, in contrast, R_{ss} is extremely high, owing to the unique nanoscale cross-section geometry of the device (see theoretical estimate in Appendix 2), giving rise to a quantum-limited

phonon thermal conductivity[34], and to the absence of electronic heat conductivity along the superconducting leads. As a result, our smaller tSOT's attain $R_{ss} \approx 10^{11}$ K W^{-1} (see experimental assessment in Appendix 2) as compared to $R_{db} \approx 10^{7}$ K W^{-1} for a 120 nm × 120 nm Cu device on a SiO_2/Si substrate at 4.2 K (Figure 1 e). The corresponding optimal R_{sd} of 10^{8} to 10^{10} K W^{-1} is readily achieved in our configuration at 4 K using a few mbar of He exchange gas (see Appendix 2 for more details). Regarding implementation of the technique for lower temperatures, our preliminary studies show that In tSOT exhibits good thermal sensitivity in ^{3}He exchange gas down to 700 mK. Reducing the working temperature further may be achieved by immersion in liquid ^{3}He which should allow operation in ^{3}He cryostat down to 250 mK and at even lower temperatures in a dilution fridge. For operation at higher temperatures NbN, MgB_2, and high-temperature superconductors could be potentially used, thus covering the full range of temperatures of interest for quantum systems.

3.2.4 Correlation between the sample and tSOT temperatures

Unlike most other scanning thermal microscopy (SThM) techniques, the tSOT is not in physical contact with the sample device under inspection. The heat mediation between the device and the sensor is carried by variable pressure He exchange gas. A dedicated multi-layer device (Figure 3a) was fabricated in order to test the correlation between the temperature measured by the tSOT and the temperature of the device. The device comprised a SiO_2/Si substrate on which Au/Cr micro-heater (25 nm/5 nm thickness) was deposited and patterned into 12 μm wide strip (green in Figure 3a), coated by 20 nm of Al_2O_3 insulating layer using atomic layer deposition (ALD). An amorphous In_2O_3 film[35] was deposited on top (33 nm thick, deposited in 1.5×10^{-5} mtorr of O_2 and annealed in vacuum for 48 hours at 40° C) and patterned into an 8 μm wide strip with multiple contacts (red) connected to Au/Cr (25 nm/5 nm) metallic contact pads (blue).

The metal-insulator transition of the a:In_2O_3 gives rise to a strongly temperature dependent resistance $R(T)$ which we utilize for self-thermometry. By globally varying the system temperature T we measure concurrently $R(T)$ of the device and $I_{tSOT}(T)$ of the tSOT under thermal equilibrium conditions between the device and the sensor as shown in Figure 3b. From these data the corresponding thermal

responses $dR/dT = -2.4$ kΩ/K and $dI_{tSOT}/dT = -10$ μA/K at 4.2 K are derived (Figure 3b). Then, by driving a low frequency *ac* current in the Au micro-heater we induce local *ac* heating in the device and measure the resulting *ac* temperatures of the In_2O_3 film, T_{ac}^{d}, and of the tSOT sensor, T_{ac}^{s}, under steady state non-equilibrium thermal conditions.

Imaging was done, here and elsewhere, using an in-house-built scanning microscope operating at 4.2 K as described in Ref. 28. SOT magnetic imaging in this microscope has recently yielded significant insight into several systems of interest[36–38]. In our case, an *ac* current was applied through the underlying Au micro-heater of 142 Ω resistance with an amplitude up to 0.35 mA at $f = 10$ Hz. The use of a low frequency is a result of the high RC time constant of the a:In_2O_3 device due to its high resistance (2-probe resistance of 200 kΩ). The resulting *ac* temperature variation of the device T_{ac}^{d} at $2f$ (due to Joule heating, see section 3.2.7 for more details) was measured by applying a probing *dc* current of 1 μA to the current leads of the In_2O_3 device and measuring the second-harmonic voltage signal on the central segment of the device using a lock-in amplifier. A tSOT of 110 nm diameter and 2.1 μK/Hz$^{1/2}$ temperature sensitivity (in the white noise region above few hundred Hz) was positioned 500 nm above the center of the central segment of the device (Figure 3c inset) in 16 mbar of He exchange gas. The relatively large height of the tSOT was used for convenience since only the average local temperature measured by the tSOT was of importance for direct comparison with the temperature reading of the device. Figure 3c shows the simultaneously measured T_{ac}^{d} and T_{ac}^{s} vs. the total power P dissipated in the micro-heater. The dashed lines show a linear fit on a log-log scale to the data and also mark the noise levels of 200 μK and 4 μK of the two measurements using 1 sec time constant of the lock-in amplifiers. The two signals scale linearly with P as expected with T_{ac}^{s} closely following T_{ac}^{d} thus establishing a measurement of the actual device temperature by the tSOT.

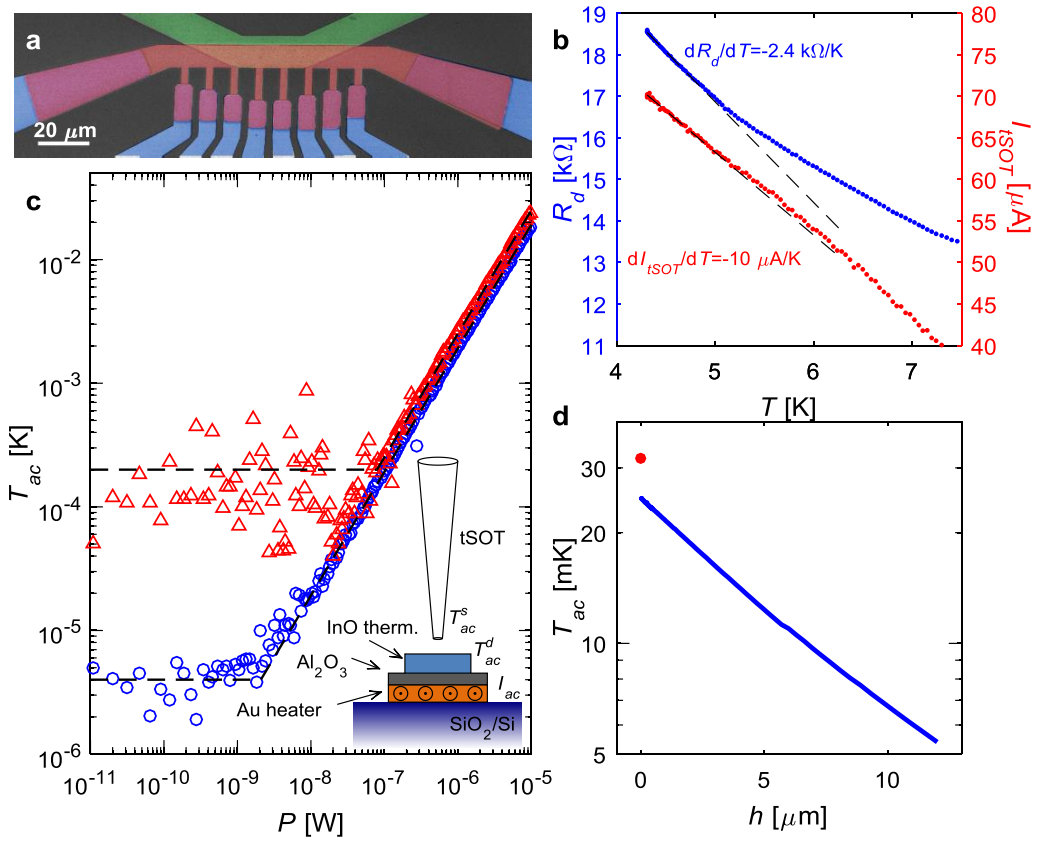

Figure 3 | Comparison between the sample and tSOT temperatures.

a, False-color SEM image of the sample consisting of Cr/Au micro-heater (green), 33 nm thick a:In_2O_3 thin film thermometer with series of contacts (red), and Au/Cr leads (blue). The micro-heater is insulated from the a:In_2O_3 by 20 nm layer of Al_2O_3. **b**, Simultaneous four probe measurement of the resistance $R(T)$ of the central In_2O_3 segment of the device (blue) and of the current $I_{tSOT}(T)$ through the tSOT (red) vs. temperature T under thermal equilibrium conditions. The dashed lines show the corresponding slopes and the thermal responses at 4.2 K. **c,** Simultaneously measured second-harmonic T_{ac}^{d} (red) of the In_2O_3 thermometer and T_{ac}^{s} (blue) of the tSOT vs. the total power P dissipated in the Au heater by *ac* current at 10 Hz demonstrating the close conformity of the local temperature measurement of the tSOT. Dashed lines are linear fits to the data and demarcate the thermal noise levels of the two measurements. Inset: Schematic cross section of the sample and of the tSOT positioned at a relatively large height of 500 nm above the central segment of the In_2O_3 film. **d**, T_{ac}^{s} as a function of tSOT height h above the device (blue) and T_{ac}^{d} of the central segment of the device (red).

Next we applied 0.35 mA *ac* current in the heater and measured the T_{ac}^{s} of the tSOT vs. the height h above the device surface up to $h = 12$ μm. Figure 3d shows an exponential decay of T_{ac}^{s} with the height with a characteristic length scale of 7 μm. Similar results were attained for He gas pressures in the range of 2 to 26 mbar. Interestingly, on approaching $h = 0$ the data show a higher T_{ac}^{d} by about 22% than

T_{ac}^{s}. A similar 24% systematic difference is also observed in the data of Figure 3c (that was taken 500 nm above the device). Such a difference can be readily accounted for by taking into account the thermal Kapitza resistance R_K at the In_2O_3/He gas interface which leads to temperature discontinuity at the solid/gas interface due to phonon mismatch[39]. Considering the measured temperature discontinuity and an estimate for the heat flow to the gas in our geometry we attain $R_K \cong 6$ K·cm^2/W which is consistent with the values of the Kapitza resistance between solids and helium gas at 4.2 K available in the literature[40].

3.2.5 Spatial resolution

Theoretical analysis of the tSOT spatial resolution

In the presence of local dissipation we define $\delta T(x,y)$ to describe the spatially varying surface temperature of the sample taken relative to the bath temperature T_0. Without loss of generality we will work in the limit $\delta T(x,y) \ll T_0$. The corresponding temperature $\delta T_{tSOT}(x,y)$ measured by the tSOT (relative to T_0) will be determined by a convolution of $\delta T(x,y)$ with a heat transfer kernel $W(r)$, where r is the radial distance from the tip center. The effective spatial resolution is then determined by the kernel $W(r)$ which depends on the diameter D of the tip and the scanning height h above the surface.

Our analysis is based on the assumption of ballistic flow of He atoms between the sample surface and the tSOT which for our geometry holds for He gas pressures of up to about 50 mbar [41]. We assume for simplicity that each atom carries an excess energy proportional to the surface temperature $\delta T(x,y)$ at the point of its origin and deposits this entire excess energy to the tSOT upon first encounter with its surface. We also assume that helium atoms are scattered from the sample surface with a uniform angular distribution into the half space above the surface. These assumptions make our estimate a worst case scenario, while a more complete analysis should predict a better resolution. This is because the scattering probability is expected to be higher for smaller azimuthal angles and also because we ignore the contributions of multiple atom collisions between the sample and the tSOT which are more likely to happen for atoms trapped in the narrow gap between the tip apex and the sample.

We model the tSOT as a disc of diameter D that resides in the $z = h$ plane, centered at $x = y = 0$. A planar sample is positioned at the $z = 0$ plane. Following the above assumptions the probability density distribution of atoms departing from the origin

within a small solid angle $\Delta\Omega$ that covers an area ΔS on the $z = h$ plane positioned at a radial distance r is $\Delta\Omega/\Delta S = h(h^2+r^2)^{-3/2}$. Using this expression we estimate the probability of an atom originating at $\boldsymbol{r} = (x, y)$ on the sample surface to collide with the tSOT. The resulting 2D heat transfer kernel $W(r)$ is given by

$$W(\boldsymbol{r}) = \int_0^{D/2} d\rho\rho \int_0^{2\pi} d\alpha h(h^2 + (x - \rho\cos\alpha)^2 + (y - \rho\sin\alpha)^2)^{-3/2}/2\pi$$

Accordingly, the corresponding tSOT temperature is given by

$$\delta T_{tSOT}(x, y) = (4\eta/\pi D^2) \int dx' \int dy' W(x - x', y - y')\delta T(x', y'),$$

where η is a proportionality constant determined by the heat flow balance conditions. Since in this section we are interested only in the spatial resolution of the tSOT response function in the ballistic regime we take $\eta = 1$ for simplicity. Accordingly, the kernel $W(r)$ is properly normalized such that a uniform surface temperature $\delta T(x, y) = \delta T$ results in $\delta T_{tSOT}(x, y) = \delta T$.

In the same vein, for the case of a 1D heat source, where $\delta T(x, y) = \delta T(x)$, we deduce a 1D tSOT kernel function

$$W_1(x) = \int dy\, W(x, y) = (h/\pi) \int_0^{D/2} d\rho\rho \int_0^{2\pi} d\alpha\, (h^2 + (x - \rho\cos\alpha)^2)^{-1}$$

and

$$\delta T_{tSOT}(x) = (4\eta/\pi D^2) \int dx'\, W_1(x - x')\delta T(x').$$

Figure 4a presents the 2D kernel $W(r)$ at different normalized heights h/D, indicating a highly localized behavior up to $h/D \cong 0.5$. We define the spatial resolution of the sensor for given tSOT diameter D and scanning height h as the full width at half maximum (FWHM) of $W(x, y = 0)$. Figure 4b plots the resulting spatial resolution as a function of D and h with dashed lines indicating contours of 50, 100 and 150 nm spatial resolution. Note that for small h the contours are essentially vertical, showing that for $h \ll D$ the spatial resolution is equal to D. Even at larger heights of $h \cong D/2$ a fair resolution is attained. For example, a tSOT of $D = 75$ nm at $h = 50$ nm provides a spatial resolution of close to 100 nm.

Figure 4c presents the calculated tSOT signal for a $D = 100$ nm device at different heights above a 100 nm square-shaped surface temperature profile $\delta T(x)$ as indicated by the black line. The tSOT of 100 nm diameter can clearly resolve such temperature profile at low scan heights. However, in practical planar samples, such square-shaped surface temperature profile cannot be readily realized due to heat diffusion in the substrate which causes a significant broadening of the surface temperature. This

broadening can be understood by noting that the diffusion equation for a 1D heat source and a homogeneous 3D substrate gives a heat flux that drops as $1/r$, where r is the radial distance from the line-source. This results in a $\log(r)$ temperature decay. Note that this long-range temperature decay is universal and is independent of the thermal conductivity of the substrate.

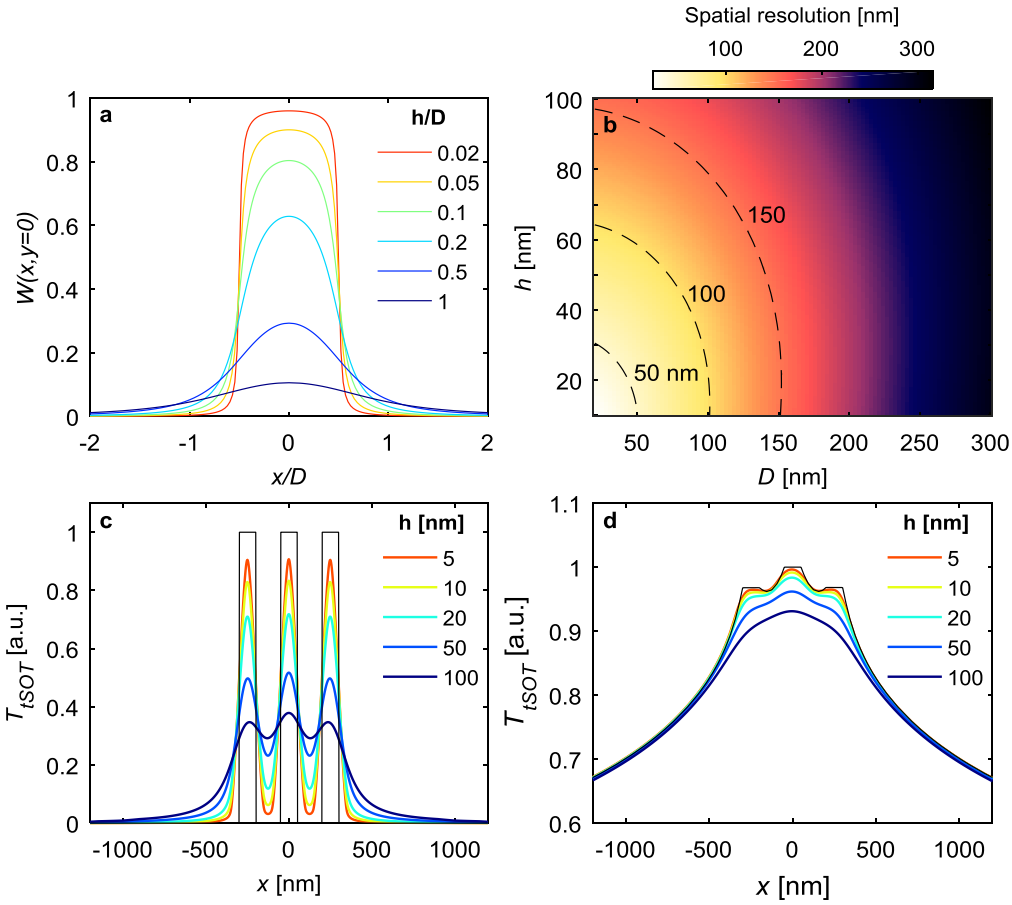

Figure 4 | Theoretical analysis of the spatial resolution of tSOT.

a, The tSOT 2D heat transfer kernel function for different heights h above a planar sample for ballistic transport of helium atoms. **b,** The resulting spatial resolution of the tSOT technique (defined as FWHM of the kernel function) as a function of tSOT diameter D and scanning height h with contour lines marking resolution of 50, 100, and 150 nm. **c,** Calculated thermal signal measured by tSOT of $D = 100$ nm at several scan heights above a square surface temperature profile $\delta T(x, y)$ with 100 nm wide steps and 150 nm gaps without heat diffusion in the substrate as indicated by black line. **d,** Calculated surface temperature (black line) and the tSOT thermal signal as in **c** in presence of heat diffusion in the substrate. The shape of the thermal profiles is independent of heat conductivity of the substrate.

Figure 5a presents a numerical solution of the heat diffusion equation showing the temperature distribution $\delta T(x,z)$ in the bulk of a semi-infinite sample containing a 1D heater of 110 nm × 30 nm cross section extending in the y direction. The black curve in Figure 5b shows the corresponding surface temperature $\delta T(x)$ of the sample displaying the long-range decaying tail that is well described by $\log(r)$ dependence (dashed curve). The colored curves in Figure 5b show the calculated $\delta T_{tSOT}(x)$ profiles for a $D = 100$ nm tSOT at various heights h above the surface. For small h values the tSOT kernel causes rounding of the sharp features on the scale $x < D$ but otherwise $\delta T_{tSOT}(x)$ closely follows the surface $\delta T(x)$. In particular, for $x > \sim 2D$ in the slow $\log(r)$ tail region, the profile $\delta T_{tSOT}(x)$ is almost indistinguishable from the surface $\delta T(x)$ for up to $h \cong 100$ nm. This result demonstrates that at larger distances the measured $\delta T_{tSOT}(x)$ is dominated by heat diffusion in the substrate rather than the intrinsic spatial resolution of the tSOT. Moreover, the $\log(r)$ tail is a characteristic fingerprint of the actual surface temperature of the sample and cannot arise from the tSOT heat transfer kernel.

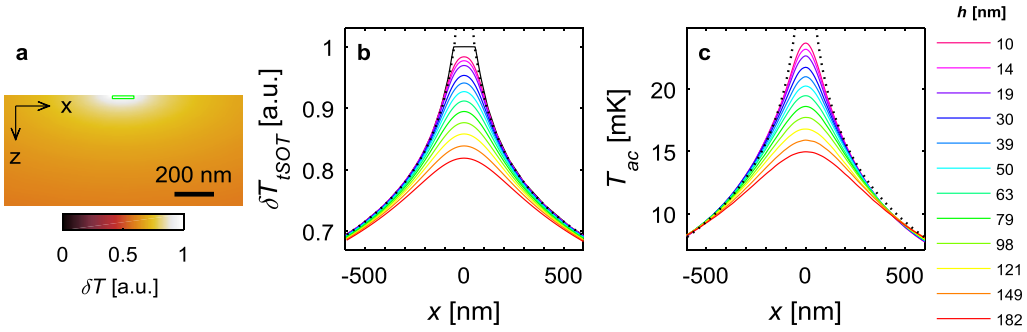

Figure 5 | Comparison of heat profiles above a 1D heater: simulation vs. experimental results.

a, Numerical solution of the temperature distribution in the bulk of the sample $\delta T(x,z)$ comprising of an infinite slab heater of 110 nm width and 30 nm thickness (outlined in green), embedded in a semi-infinite homogeneous substrate. The heat conductivity within the heater cross section is taken to be much higher than that of the substrate. The resulting functional dependence of the temperature distribution in the bulk is characterized by a universal $\log(r)$ dependence independent of the heat conductivity of the substrate. **b,** The surface temperature of the sample $\delta T(x, z = 0)$ (black line) and the calculated temperature $\delta T_{tSOT}(x)$ of a D =100 nm tSOT scanned at different heights h (as indicated). **c,** The experimentally measured temperature profiles $T_{ac}(x)$ at different scan heights above a nanowire heater. The sample and the tSOT are described in Figure 6, where the current I_{ac} was applied only to the central nanowire. The dotted lines in (b) and (c) are fits to $a + b \cdot \log(r)$ asymptotic behavior, characterizing the long-range heat diffusion in the substrate.

Figure 4d shows a similar calculation for the case where three such 1D heaters are placed 150 nm apart of each other in a semi-infinite substrate. The black curve, which describes the surface $\delta T(x)$, indicates that the heat signals of the three heaters strongly overlap due to the slow $\log(r)$ tail, producing only weak shoulders at the heater positions. We emphasize that the surface $\delta T(x)$ in this case is independent of the value of the heat conductivity of the substrate (up to a constant factor). The corresponding $\delta T_{tSOT}(x)$ well resolves the shoulders up to $h \cong D/2$ while further away from the heaters the profile $\delta T_{tSOT}(x)$ is essentially indistinguishable from $\delta T(x)$ at even higher scan heights, demonstrating once more the dominance of substrate heat diffusion in the thermal signal.

Experimental demonstration of the tSOT spatial resolution

In order to demonstrate the actual spatial resolution limit of the tSOT sensor, one has to design an experiment in which the surface temperature changes on short length scales and the dominant role of the heat diffusion in the substrate is reduced. For this purpose three parallel Pd-Au nanowire structures were fabricated on SiO_2/Si substrate (SiO_2 thickness of 150 nm). Each nanowire is 110 nm wide and 30 nm thick including 5 nm Ti adhesion layer, with 155 nm gap between the nanowires. A trench of 1.4 μm width and 117 nm depth was then etched into the SiO_2 layer using buffered HF solution, resulting in a suspended segment of the three nanowires as shown in tilted SEM image in Figure 6a. The device was thermally imaged in various current configurations with a tSOT of effective magnetic diameter of 55 nm (determined from the period of tSOT quantum interference) and physical inner and outer diameters of 20 nm and 100 nm respectively.

We first drive an *ac* current $I_{ac} = 0.7$ μA at 663 Hz through the central nanowire resulting in an average dissipation of 8 pW per square segment of the wire and measure T_{ac} of the tSOT across the wire at different scanning heights h as shown in Figure 5c. The experimental data are in very good qualitative agreement with our numerical results in Figure 5b. In particular, the $\log(r)$ temperature decay (dashed line) is clearly reproduced, with the very weak h dependence away from the origin confirming the dominant role of heat diffusion in the substrate and the locality of the tSOT kernel. We note that the qualitative behavior is not affected significantly by the fact that the nanowire is suspended. This is due to the fact that the suspended segment is short (1.4 μm) relative to the full length of the nanowire and the suspension height

is only 117 nm. As a result, the long-range heat diffusion in the substrate is still governed by a 1D heat source, which gives rise to the observed $\log(r)$ behavior. Next, we applied a total of $I_{ac} = 0.5$ μA at 663 Hz to the three nanowires in parallel and imaged the temperature distribution at $h \cong 15$ nm as shown in Figure 6b. A line cut through the data is shown in Figure 6c. The presence of the two outer nanowire heaters is visible as shoulders in the T_{ac} profiles followed by $\log(r)$ tails in very good qualitative agreement with the numerical results in Figure 4d. Note that even though T_{ac} in the suspended segment in Figure 6b (outlined by the dotted lines) is higher than in the non-suspended regions, the $\log(r)$ decay through the substrate is essentially the same as discussed above.

We emphasize that the temperature $T_{tSOT}(x, y)$ measured by the non-contact tSOT scanning at height h above the sample reflects the local temperature profile of the sample convoluted with the height dependent kernel W. Consequently, in the case of suspended nanowires the $T_{tSOT}(x, y)$ reflects the temperature of the nanowires as well as the background temperature of the substrate in-between the wires. In contrast, contact-based vacuum SThM[11–15] would detect only the temperature of the suspended nanowires if scanning at a height corresponding to the top surface plane of the nanowires.

The above cases indicate that heat diffusion in the bulk has a dominant effect on the surface temperature distribution. This long-range contribution, however, can be significantly suppressed by two methods as follows. The first approach takes advantage of the fact that the phase of the *ac* power P_{ac} can be readily controlled. Consider a wire carrying a low frequency *ac* current $I\cos(\omega t)$, which results in power dissipation $P = P_0\cos^2(\omega t) = 0.5P_0 + 0.5P_0\cos(2\omega t) = P_{dc} + P_{ac}$. As a result, the wire creates a certain surface temperature profile $\delta T(x, t) = \tau(x) + \tau(x)\cos(2\omega t)$. Note that the temperature profile for the same wire carrying current of $I\sin(\omega t)$ will be $\delta T(x, t) = \tau(x) - \tau(x)\cos(2\omega t)$ with a negative *ac* term. Let us consider two such wires at $x = -d$ and $x = d$ carrying currents $I\cos(\omega t)$ and $I\sin(\omega t)$. The resulting temperature distribution will now be given by $\delta T(x, t) = \delta T_{dc}(x) + T_{ac}(x)\cos(2\omega t) = \big(\tau(x - d) + \tau(x + d)\big) + \big(\tau(x - d) - \tau(x + d)\big)\cos(2\omega t)$.

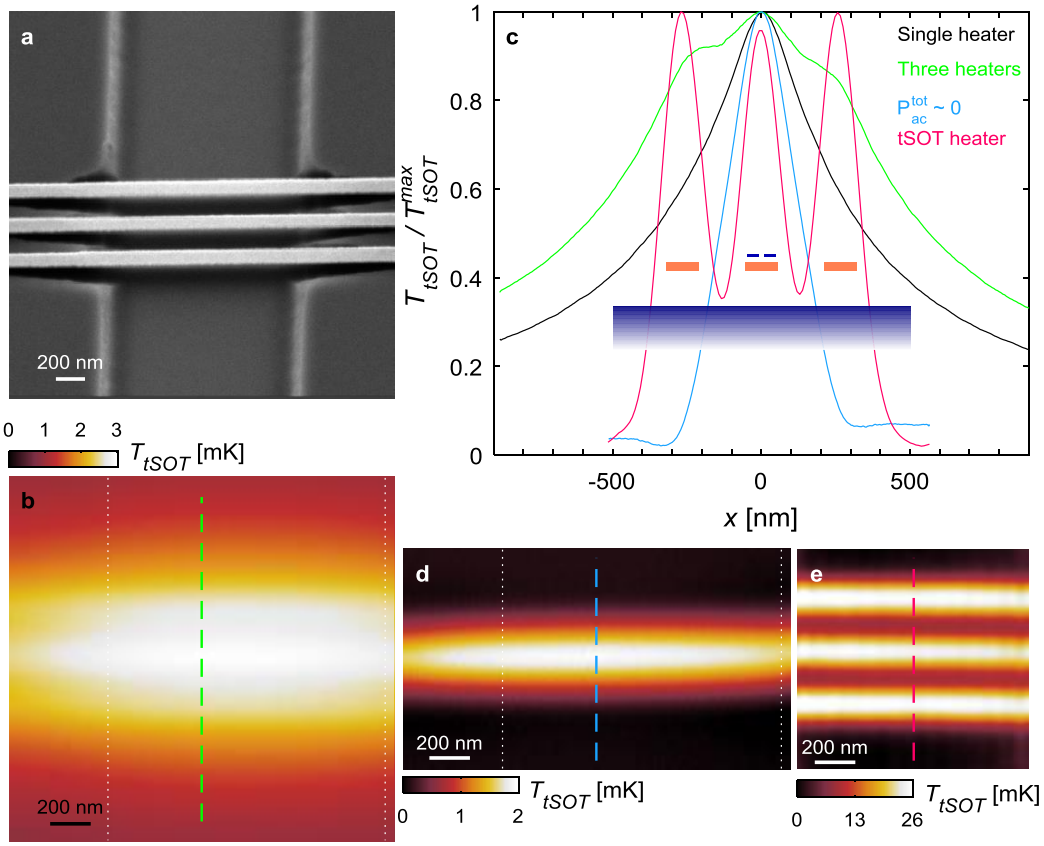

Figure 6 | Experimental demonstration of spatial resolution of tSOT.

a, SEM image (tilted at 45°) of three Pd-Au nanowire heaters (110 nm wide, 30 nm thick, 155 nm separation) suspended above a 1.4 μm wide and 117 nm deep trench etched into SiO_2/Si substrate. **b-d,** Thermal imaging $T_{tSOT}(x, y)$ of the device in three different measurement schemes using tSOT of $D = 100$ nm at scan height of $h = 15$ nm. **b,** Thermal image due to *ac* current applied in parallel to all three nanowires dissipating 3 pW per square segment of nanowire measured at the second harmonic of 663 Hz. White dotted lines indicate edges of the trench. **c,** Thermal profiles across the device for the cases of central wire heater, three wire heaters (along green line in **b**), compensated total power (along blue line in **d**), and tSOT heating (along red line in **e**, see section 3.2.11). Inset: a schematic to-scale cross section of the experimental setup including the substrate (light blue), nanowires (orange), and tSOT apex (blue). **d,** Thermal image for the case of "heat dipole" in which $P_{ac} \cong 8.7$ pW per square segment of nanowire is dissipated in the central wire while out-of-phase power of $P_{ac} \cong$ -4.2 pW and -4.5 pW per square segment of nanowire is "absorbed" in the two outer wires thus suppressing the long-range heat diffusion in the substrate (all measured at the second harmonic of 663 Hz). **e,** Thermal image with no current flowing in the wires while a larger current of 152 μA is driven through the tSOT causing dissipation in the tip apex. The resulting increase in the local temperature in the suspended nanowires during scanning is larger than in the recessed substrate as expected from the ballistic model. The scan window is within the suspended section. Time constants are 30 ms/pixel in all images, pixel sizes are 13 nm (b), 10 nm (d) and 10 nm (**e**).

Since the instantaneous P is always positive, the instantaneous $\delta T(x,t)$ and δT_{dc} are positive as well. However, $T_{ac}(x)$ can be either positive or negative. In particular, when the two wires overlap ($d = 0$), $T_{ac}(x) = 0$ everywhere and $\delta T(x,t) = 2\tau(x)$. This is because P_{ac} of the first wire is fully "absorbed" by the negative P_{ac} of the second wire. When the two wires are separated, the total P_{ac}^{tot} remains zero and the corresponding $T_{ac}(x)$ attains a "dipole" structure with positive and negative values on the two wires. As a result, the long-range $\log(r)$ decay of $T_{ac}(x)$ of a single wire is replaced by a faster $1/r$ behavior. Applying this additional degree of freedom to three wires we can produce much more local $T_{ac}(x)$ temperature profiles. We implement this concept here by driving I_{ac} in the central wire and $\sim I_{ac}/\sqrt{2}$ with a phase shift of $\pi/2$ in each of the outer wires. As a result, the power P_{ac} dissipated in the central wire is mostly "absorbed" by $-P_{ac}/2$ in each of the outer wires thus forming a "screened" local source with total $P_{ac}^{tot}\sim 0$. The resulting T_{ac} image in Figure 6d and the corresponding line profile in Figure 6c show a narrow temperature peak and the strong suppression of the $\log(r)$ tail, demonstrating the high spatial resolution of the tSOT. The above three current schemes are summarized by numerical simulations in Figure 7. The temperature distribution in the bulk of the substrate for the cases of single heater, three heaters, and $P_{ac}^{tot}\sim 0$ are shown in Figure 7a-c, and the corresponding $\delta T_{tSOT}(x)$ for $D = 100$ nm at $h = 15$ nm are presented in Figure 7d demonstrating a proper description of the experimental data. In particular, the width of the measured T_{tSOT} signal at FWHM of the $P_{ac}^{tot}\sim 0$ of 284 nm in Figure 6c is in excellent agreement with the calculated width of 270 nm in Figure 7d.

Finally, we present an alternative approach to reduce the long-range substrate heat diffusion contribution based on the fact that for the case of a point source the heat flux in the substrate drops as $1/r^2$ resulting in $1/r$ decay of the surface temperature rather than the $\log(r)$ behavior for 1D heat source. In order to implement a point source we can use the tSOT itself as a point heater (see section 3.2.11 for more information on this technique) which causes local heating of the sample surface which in turn causes a corresponding change in the tSOT temperature. In our sample geometry and in the ballistic He transport regime, the tip that scans at a constant height will locally heat up the suspended nanowires when hovering 15 nm directly above their surface. When passing above the gaps between the wires, in contrast, the local heating of the etched SiO_2 substrate that resides some 162 nm below the tip will be significantly smaller

due to the much smaller solid angle, leading to a sharp temperature contrast between the nanowires and the substrate. Figure 6e presents a thermal image of the suspended section in this "tSOT heater" mode showing three sharply resolved nanowires. The line cut through the image is presented in Figure 6c with a width of the central peak at FWHM of only 132 nm as compared to 110 nm width of the nanowire and the tSOT diameter of 100 nm. We can model this situation by approximating a step-like change in the effective surface temperature of a sample as shown in Figure 4c. In this case the rounding of the thermal signal will be determined only by the tSOT kernel. Figure 7d "step T profile" presents the calculated $\delta T_{tSOT}(x)$ profile using $h = 15$ nm and $D = 100$ nm which shows a very good correspondence with the experimental data albeit with a larger temperature modulation. Since the width of the nanowires is comparable to D the actual effective surface temperature of the sample due to the heating by the scanning tSOT is expected to be also significantly rounded explaining the reduced modulation.

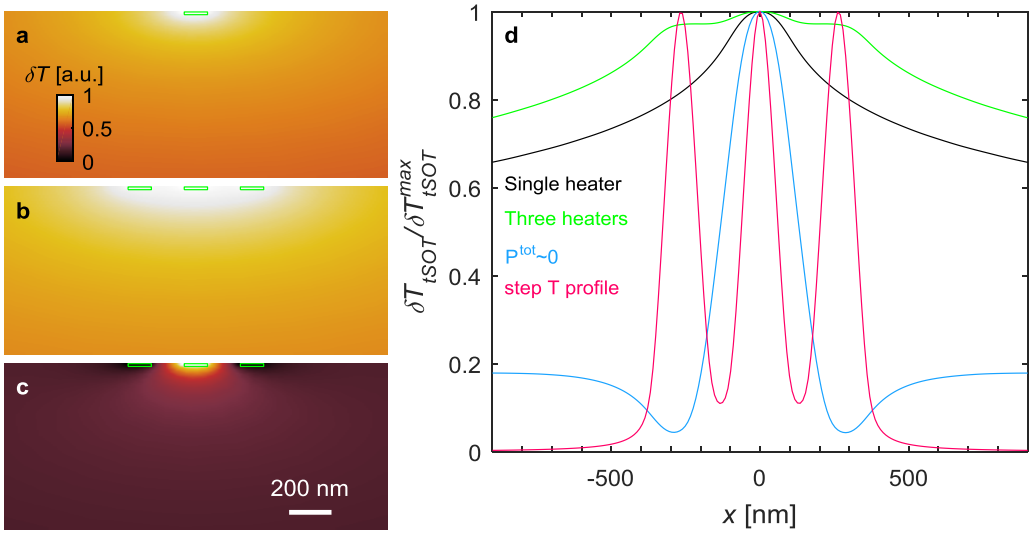

Figure 7 | Theoretical comparison of different heating schemes.

a, Temperature distribution $\delta T(x,z)$ in the bulk of the sample due to a 1D heater of 110 nm × 30 nm cross section (green outline) embedded in a semi-infinite substrate. **b,** Temperature distribution due to three such heaters separated by a gap of 155 nm. **c,** Temperature distribution in the case of a "heat dipole" with $P_{ac}^{tot}\sim 0$ in which each of the two outer heaters "absorbs" 43% of the *ac* power dissipated by the central heater (see text). **d,** Calculated temperature profiles for $D = 100$ nm tSOT scanning at $h = 15$ nm above the surface in the three cases **a-c** and for the case of surface local heating (estimated by taking step profiles as the surface temperature) by the tSOT.

Interestingly, in Figure 6e a higher T_{tSOT} temperature is attained above the suspended nanowires in contrast to what one may expect. This counter-intuitive behavior results from the height differences and the fact that the He atoms are in ballistic rather than diffusive regime. The local density of heat flow from the warm tip to the sample and the corresponding local surface temperature increase are strongly height dependent due to solid angle considerations. Since the suspended nanowires are much closer to the tip, their local temperature increase is significantly larger as compared to the temperature increase of the deeper Si substrate between the wires, leading to the increased T_{tSOT} above the nanowires. Indeed, similar measurements in the planar region where the nanowires reside on the substrate show a lower T_{tSOT} above the nanowires due to their higher heat conductivity (Figure 12b).

To conclude, the above experimental results in various dissipation schemes are well described by our numerical calculations and clearly demonstrate that the spatial resolution of the tSOT at low scanning heights is comparable to the tip diameter D.

3.2.6 Demonstration of tSOT temperature sensitivity

The features of the technique as discussed above permit non-contact sensing of the T_d of the sample with nanoscale resolution. To characterize the thermal sensitivity of the scanning tSOT, we position the sensor above a 120-nm-wide Cu nanowire on a SiO_2/Si substrate (Fig. 1d and Fig. 8); the nanowire is carrying an alternating current (*ac*), which results in an *ac* temperature modulation T_{ac} of the nanowire at 13.1 kHz. By changing the current amplitude, we measured tSOT T_{ac} versus the power P dissipated per square 120 nm × 120 nm segment of the wire (Figure 1e). Since $T_{ac} \ll T_0$, where T_0 = 4.2 K is the thermal bath temperature, the measurement is in the small signal limit and hence T_{ac} is linear in P as expected, reaching a noise level of $T_{ac} \approx 440$ nK at $P \approx 6$ fW. The green triangle in Figure 1e shows the Landauer dissipation limit of P = 40.2 fW of a qubit operating at 1 GHz at 4.2 K, which gives rise to T_{ac} = 2.6 μK in our sample. This value is indicated in Figure 1a (green triangle) along with the expected inverse scaling of the qubit temperature with its area (dashed line). Figure 8 presents two T_{ac} profiles by scanning with the 46 nm diameter tSOT across the nanowire at two levels of power dissipation P per square segment of the nanowire. The blue data were acquired at $P =$ 143 pW while the red data were measured at $P =$ 57 fW close to the Landauer limit of 40 fW for 1 GHz qubit operation. The T_{ac} profiles show a sharp peak above the nanowire and extended tails due to heat diffusion in the SiO_2/Si substrate.

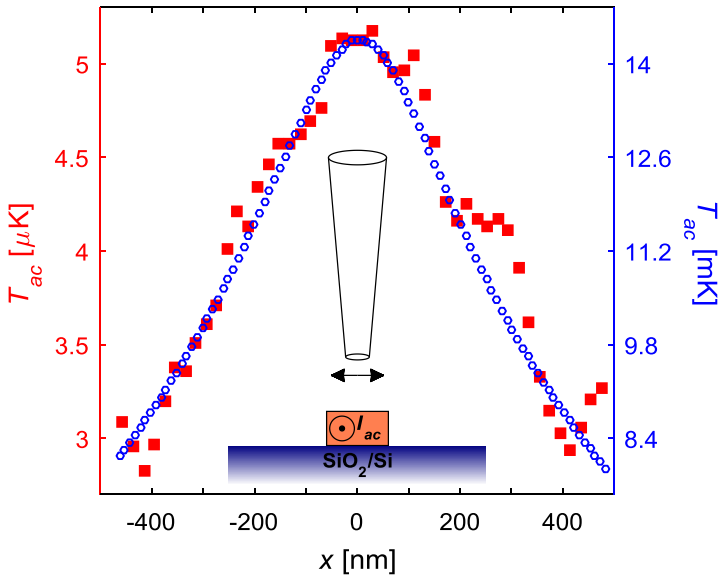

Figure 8 | Demonstration of tSOT temperature sensitivity.

T_{ac} profiles across a 120 nm wide Cu nanowire at dissipation powers of 143 pW (blue) and 57 fW (red) per square segment measured by a tSOT of 46 nm diameter. The data were acquired using lock-in amplifier time constants of 0.3 sec and 1 sec respectively at height of 120 nm above the surface. Inset: schematic diagram of the Cu nanowire sample and the scanning tSOT.

3.2.7 Simultaneous magnetic and thermal imaging

By applying a proper combination of magnetic field H_z and I_{bias}, the tSOT can be tuned to have both magnetic field and thermal sensitivity, thus providing a unique capability of simultaneous magnetic and thermal imaging. Figure 9a shows a SEM micrograph of a "zigzag" nanostructure consisting of alternating segments of 100 nm wide Cu and 80 nm wide ferromagnetic Py ($Ni_{80}Fe_{20}$) wires. An *ac* current $I_{ac} = 10$ μA is applied to the sample at $f = 6.56$ kHz and three signals are acquired simultaneously from the tSOT during scanning: time-averaged *dc* and two *ac* signals at frequencies f and $2f$ using two lock-in amplifiers. At the used bias conditions the tSOT had a thermal response of -8.6 μA/K and a simultaneous magnetic response of 91 nA/mT.

The *dc* signal provides an image of the *dc* magnetic field B_z^{dc} (Figure 9b) in presence of out-of-plane $\mu_0 H_z = 0.32$ T and an in-plane field $\mu_0 H_{||} = 0.1$ T applied parallel to the Py nanowires. The image reveals that the Py nanowires are in a single in-plane magnetization domain state giving rise to the sharp peaks in the stray field

B_z^{dc} at the ends of the nanowires. The Py nanowires also show a weaker bright signal along their length due to the out-of-plane tilting of the magnetic moments by H_z .

Figure 9c presents the first-harmonic *ac* component, which describes the *ac* magnetic signal B_z^{ac}, generated by I_{ac}. It shows that the current flows continuously along the zigzag structure avoiding the upper protruding parts of the nanostructures. This is quantitatively confirmed by the Biot-Savart law numerical simulation of B_z^{ac} in the inset, also providing an accurate estimate of the tSOT scanning height of 175 nm.

The power dissipated in a resistor R due to a sinusoidal *ac* current $I_{ac} = I_0 \cos \omega t$ is given by $P = RI_{ac}^2 = RI_0^2(1 + \cos 2\omega t)/2$ giving rise to *dc* temperature increase T_{dc} and *ac* temperature variation T_{ac} at 2ω. Figure 9d shows the resulting temperature map T_{ac} (the accompanying *dc* signal due to T_{dc} is substantially smaller than B_z^{dc} and was subtracted from Figure 9b for clarity). In contrast to the very uniform B_z^{ac} along the zigzag structure in Figure 9c, T_{ac} in Figure 9d is highly non-uniform revealing a significantly higher temperature of the Py segments. This is the result of about 40 times higher sheet resistance 18 Ω/□ in Py than in Cu nanowires, giving rise to significantly higher dissipation along the Py segments. Interestingly, the nanowire segments protruding beyond the top corners of the zigzag also display an increased temperature despite the fact that no current flows there, revealing higher thermal conductivity of the metallic nanowires as compared to the underlying substrate. The tSOT thus provides multifunctional abilities for simultaneous imaging of magnetic and thermal signals.

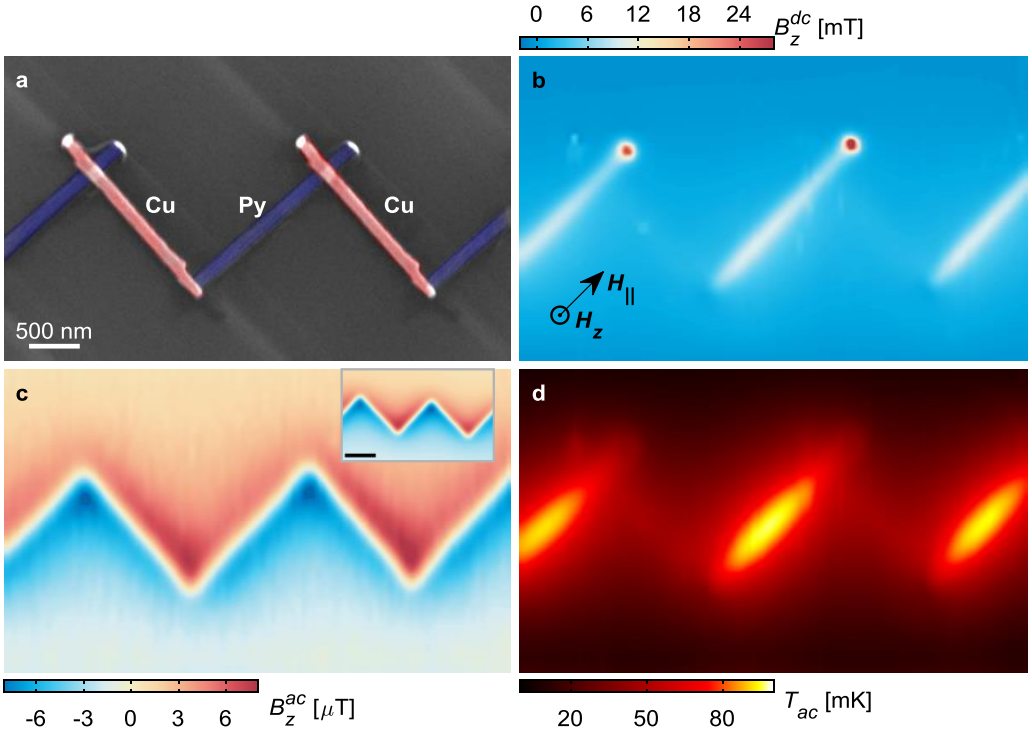

Figure 9 | Simultaneous scanning tSOT thermal and magnetic imaging.

a, False color SEM image of zigzag structure of alternating Cu (red) and Py (blue) nanowires. **b**, Image of B_z^{dc} in presence of applied magnetic fields of $\mu_0 H_z = 0.32$ T and $\mu_0 H_{||} = 0.1$ T revealing the in-plane magnetization of Py segments. **c**, B_z^{ac} due to applied $I_{ac} = 10$ µA at 6.56 kHz through the structure. Inset: Theoretically calculated B_z^{ac} 175 nm above the sample. **d**, Simultaneously measured thermal image of T_{ac} at $2f$ showing significantly higher dissipation in Py segments (pixel size 50 nm, scan speed 120 ms/pixel).

3.2.8 Bandwidth of the tSOT thermal imaging

Thermal processes at the nano-scale may have very short relaxation times and hence it is highly desirable for a nano-thermometer to have a high bandwidth (BW) to study relaxation processes. Figure 10 shows the frequency response of tSOT positioned at a relatively large distance of 500 nm above an Au thin film heater in He exchange gas pressure of 26 mbar. The figure shows the measured T_{ac} vs. the frequency f of the heat signal (second harmonic) for two values of the *ac* power in the heater demonstrating BW of over 200 kHz which was limited by the BW of our electronic readout circuit.

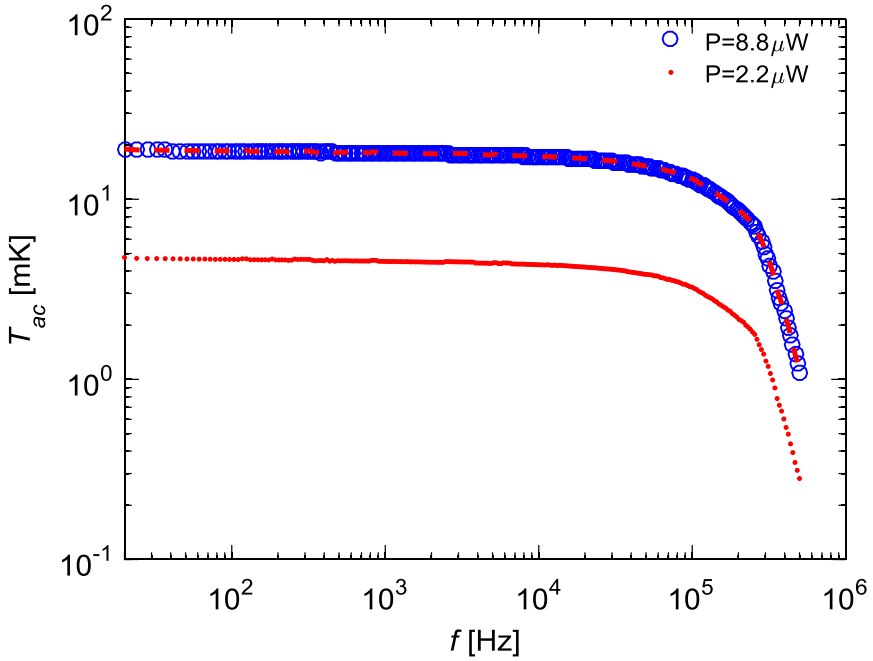

Figure 10 | Bandwidth characterization of the tSOT.

Frequency dependence of T_{ac} measured by a tSOT 500 nm above Au heater for *ac* heater powers of 8.8 μW and 2.2 μW. Dashed red line shows the data collapse by multiplying the low power signal by 4. The bandwidth of 200 kHz is limited by external readout electronics.

We can estimate the intrinsic thermal BW of the tSOT as following. The thermal time constant of the tSOT driven by the heat source in the sample should be given by the sensor's heat capacity times the sensor-heater thermal resistance R_{sd}. The mass of the Pb apex of a tSOT with diameter D = 100 nm and thickness of 10 nm is approximately 10^{-18} Kg and therefore has a heat capacity of about C = 10^{-18} J/K, taking Pb specific heat[42] as 0.042 cal/Kg · mole. For R_{sd} that is typically below 10^{10} K/W, the resulting intrinsic tSOT bandwidth is therefore above 10 MHz.

3.2.9 Approaching the sample

One of the technical challenges in setting up a tSOT measurement of a sample is to navigate in three dimensional space and safely bring the tSOT to nanometric distances above a known position of the sample. While the vacuum can is open at room temperature, one can optically attempt to position the tSOT, but once the can is closed, no visual information is available, and one has to rely on other means. Originally, dedicated navigation patterns were designed on samples to provide directions toward the region of interest in the sample, for instance, using the Oersted magnetic field due to running current through the sample, and analyzing the observed

magnetic features. This proved to be cumbersome, time-consuming, and set strict constraints on sample design. Using the thermal sensitivity of the tSOT, a more robust and straightforward navigation scheme was implemented. As a rule of thumb, 1 μW of energy, dissipated as Joule heating over a few hundred nms wide constriction (by running an *ac* current at low frequencies – up to few tens of Hz) can be detected from a distance of roughly 500 μm. As the heater becomes more resistive and narrow, the signal can be detected from even larger distances. For instance, in the CNT case described below, the heat signal from running a current through the CNT was used for navigation purposes, and was detected from a 1 mm distance from the sample. The above can be achieved by introducing about 6 mbar of He exchange gas. As the gas pressure increases the signal becomes more localized, and thus the approach signal is lost. Therefore, the first phase of the measurement, the approach stage, is performed at a relatively low pressure of a few mbar's. First the tip is coarse scanned along X and Y axis in search for a peak in thermal signal, prior to approaching in Z. Upon reaching the sample the pressure is increased to an order of 50 mbar, to improve coupling with the sample, and reaching the required thermal properties (see section 3.2.2).

3.2.10 Tuning-fork based height control

In many of the measurements performed throughout this work (graphene measurements and the tSOT spatial resolution measurement, as mentioned) scan heights above the sample were controlled by mechanically attaching the tSOT to a quartz tuning-fork (TF). The used TF is a quartz oscillator with nominal frequency of 32.768 kHz (product number TB38 of HM international). The TF was filed along three planes to adapt it to scanning constraints without violating the inversion symmetry of its two prongs. The filing shifted the resonant frequency to about 37 kHz. The tSOT protruded beyond the TF by a few tens of μm as demonstrated in Figure 11. The TF was mechanically excited using a piezo-electric crystal as a dither. The TF's response was read electrically through the voltage on its electrodes, which was pre-amplified at room temperature and fed into a lock-in amplifier. This assembly has a quality factor of ~30,000 at a temperature of 4.2 K and vacuum conditions. As the tSOT approaches heights of ~10 nm above the surface of the sample its electrostatic interaction with the surface affects the resonant frequency of the TF. By applying a phase-locked loop (PLL) this frequency shift is monitored and used to

determine the proximity of the tip to the sample. The scanning is then performed at a constant z-plane at a determined height above the sample surface. In a different scan mode, the PLL was not used, but the TF phase signal was directly tracked without feedback and used to assess the height above the sample. The TF was used both as a safety and height control mechanism and as a measurement technique in order to get a high signal-to-noise ratios for *dc* measurements (for instance, in the case of the graphene measurements) as described in section 4.2.3.

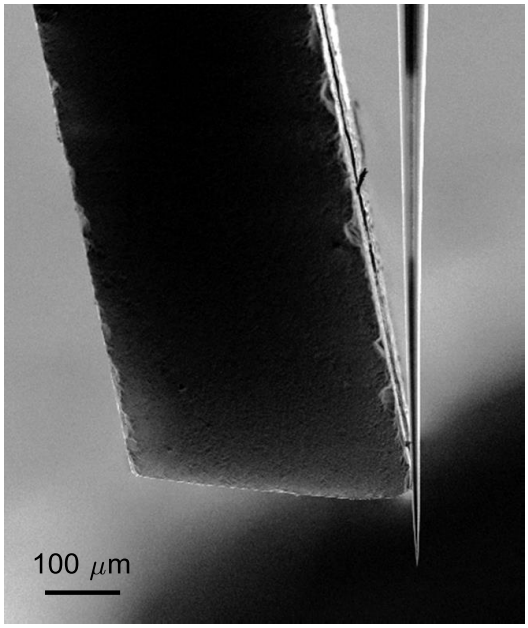

Figure 11 | Quartz crystal tuning fork resonator for tSOT height control.
A SEM image showing a side view of the filed TF with the attached tSOT pipette. The tSOT protrudes typically 50 to 100 μm beyond the TF.

3.2.11 tSOT heater measurement mode

In the 'tSOT heater' measurement mode we use the tSOT itself as a point heater by driving a current through the tip, significantly larger than the critical current, thus causing a local heating of the tSOT apex. This point-like heater will cause local heating of the sample surface which in turn causes a corresponding change in the tSOT temperature. A similar mechanism is commonly used in SThM schemes in which a warm scanning tip acts as a local heat source[21,23]. In our case, however, the probe is not in contact with the sample, but relies on heat transfer by the exchange gas. The 'tSOT heater' measurement mode was used in section 3.2.5 (Figure 6c,e and text therein) in order to demonstrate the actual limit on spatial resolution of the tSOT sensor, as opposed to the spatial resolution of the thermal images which were

dominated by heat conduction into the sample substrate. This mode proved to be very useful, being highly sensitive to the topography of the sample, and even to material composition, as demonstrated in the following two examples. Figure 12a presents a SEM image of the suspended gold nano-wires sample that was used in the spatial resolution demonstration of Figure 6. Three zoomed-in SEM images of the three trenches were taken (Figure 12c-e), which requires an exposure of the sample surface to a higher dosage of the electron beam. Remarkably, these higher exposure regions are resolved by the tSOT heater image of Figure 12b, pointing at an improved heat flow from the tSOT when over these regions compared to the un-exposed substrate. This is possibly due to a coating of the sample surface with a thin layer of carbon atoms during exposure to the e-beam, which apparently affects the Kapitza resistance, and reduce the thermal resistance between the tip and the sample.

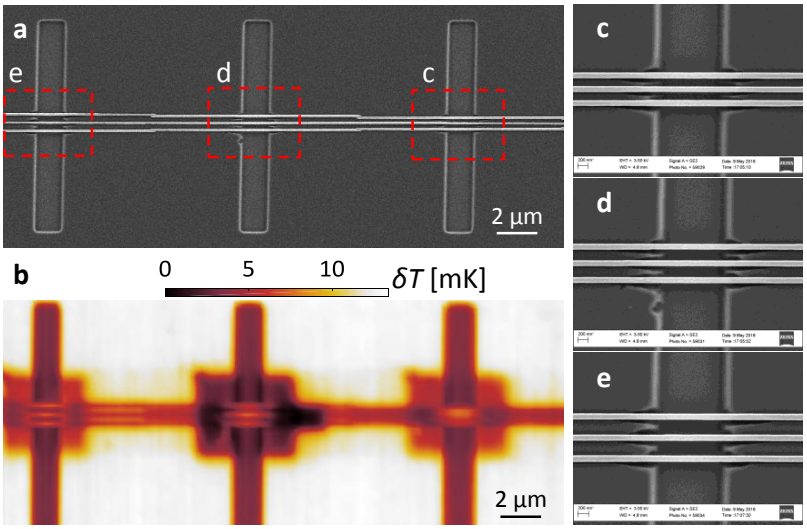

Figure 12 | tSOT heater measurement mode: Resolving topography.

tSOT is used as a point heater giving high contrast at different interfaces, corresponding to local differences in effectivity in removing heat from the tSOT. **a**, SEM image of the sample, which is the same sample of the spatial resolution demonstration (section 3.2.5). Three gold nano-wires are suspended over trenches that were etched in SiO_2. **b**, tSOT heater measurement of the sample at a height of 50 nm. **c-e**, High resolution SEM images of the regions marked by dashed rectangles in (a), which were resulted in higher local exposure of the sample to the e-beam. Even beyond resolving the trenches and the nano-wires (as more clearly visible in Figure 6e of section 3.2.5), the tSOT heater measurement mode can remarkably resolve the e-beam exposed regions.

The second demonstration focuses on measuring graphene devices by tSOT heater mode. In Figure 13a a graphene flake on top of a SiO_2 surface is imaged. The technique can clearly resolve a mono-layer of graphene over the SiO2 background and small defects along the edges of the flake. Surprisingly, the technique can even resolve a transition between a mono-layer and a bi-layer as indicated in the optical image at the inset of Figure 13a. Perhaps more significant is the capability to track heat conduction pathways, as apparent in the imaging of an hBN encapsulated graphene structure of Figure 13b. When imaging the structure in this measurement mode a 'cold' rim appears along the edges of the hBN. Since a buried graphene edge does not show this feature, we are led to assign this feature to the hBN. It suggests an improved heat conduction between the tSOT and the hBN flake through the edges as opposed to the bulk.

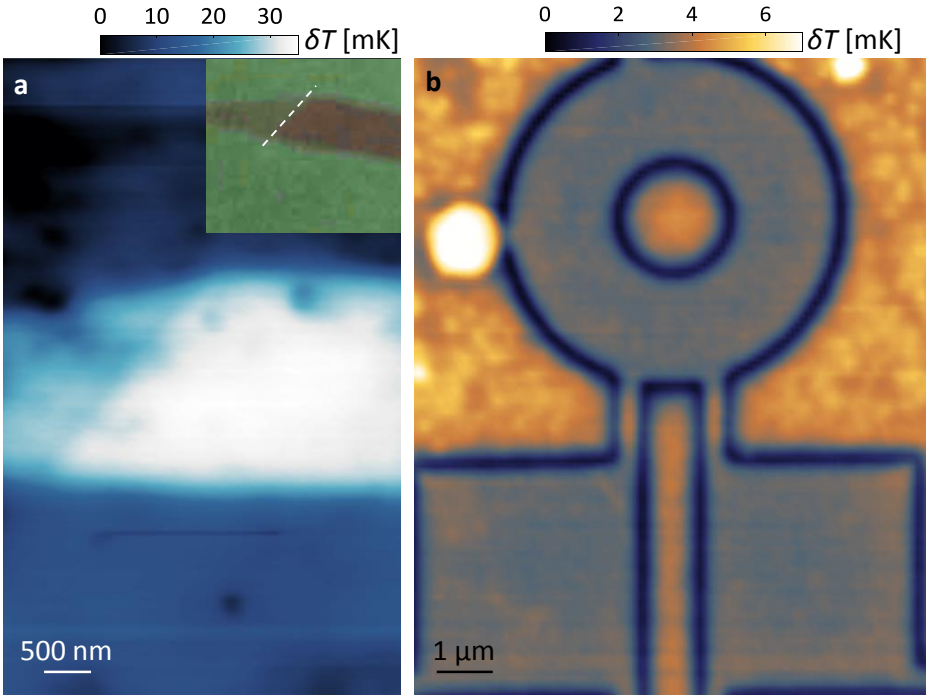

Figure 13 | tSOT heater measurement of graphene.

a, tSOT heater measurement of a graphene flake on SiO_2. The inset shows an optical image of a segment of the flake with a transition (dashed line) between a monolayer (left) to a bi-layer segment (right). Image taken at an estimated height of order 100 nm (no TF used). The measurement can clearly resolve the graphene from the SiO2 and even the transition between the monolayer and the bi-layer graphene. **b**, tSOT heater measurement of an hBN encapsulated graphene heterostructure, taken 50 nm above the structure (see section 4.2.1), resolving SiO_2 structure, trapped bubbles and a clear cold looking edge (dark) revealing a more effective heat pathway by the edges of the structure.

3.3 Results - Thermal imaging of dissipation in Carbon nanotube devices

We used the tSOT for nanoscale thermal imaging of quantum matter. Figure 14a, b shows T_{ac} images of two single-walled carbon nanotubes (CNTs) carrying an alternating current of few nA (see Appendix 3 for more information). Each CNT is wound into a loop[43], as outlined by the dotted trajectories and shown by SEM images in Figure 14d,e. The thermal signal in Figure 14a tracks the CNT, revealing the current-driven dissipation along the entire length of the CNT. Surprisingly, and in contrast to the above, Figure 14b shows an absence of heating in the circular part of the loop. The T_{ac} image thus reveals that the applied current bypasses the loop, exposing an electrically shorted junction between the two crossing sections of the CNT. This observation illustrates the capacity of the tSOT for fault detection in operating nano-devices.

A striking feature evident in Figure 14a, b is ring-like fine structures: a zoomed-in T_{ac} image of one of these is shown in Figure 14c. These features resemble the Coulomb blockade rings observed in scanning gate microscopy[44], in which the conductance through a quantum dot is measured as a function of the position of a conducting AFM tip. In the scanning gate microscopy case, the characteristic equipotential rings (corresponding to the periodic conditions of Coulomb blockade peaks governed by single-electron charging of the quantum dot[45]) originate from the tip acting as a local gate. Since the tSOT is conducting, it can also serve as a nanoscale scanning gate. The disordered substrate potential in our long CNTs on the SiO_2/Si substrate gives rise, however, to carrier localization and formation of a series of electronic quantum dots, resulting in CNT resistances in excess of 10 MΩ. As a result, no detectable change in CNT conductance is observed while scanning the tSOT. The unique feature of the tSOT, however, is that in addition to functioning as a scanning gate it simultaneously operates as a nanoscale thermometer that detects minute changes in the local dissipation resulting from its own controllable local gating. The T_{ac} ring in Figure 14c with a cross-sectional width of 20 nm (Figure 14f) thus reveals μK-range changes of the temperature of a quantum dot resulting from the modulation of its single-electron Coulomb blockade conductance peaks by the scanning tSOT (see Appendix 4 for additional details).

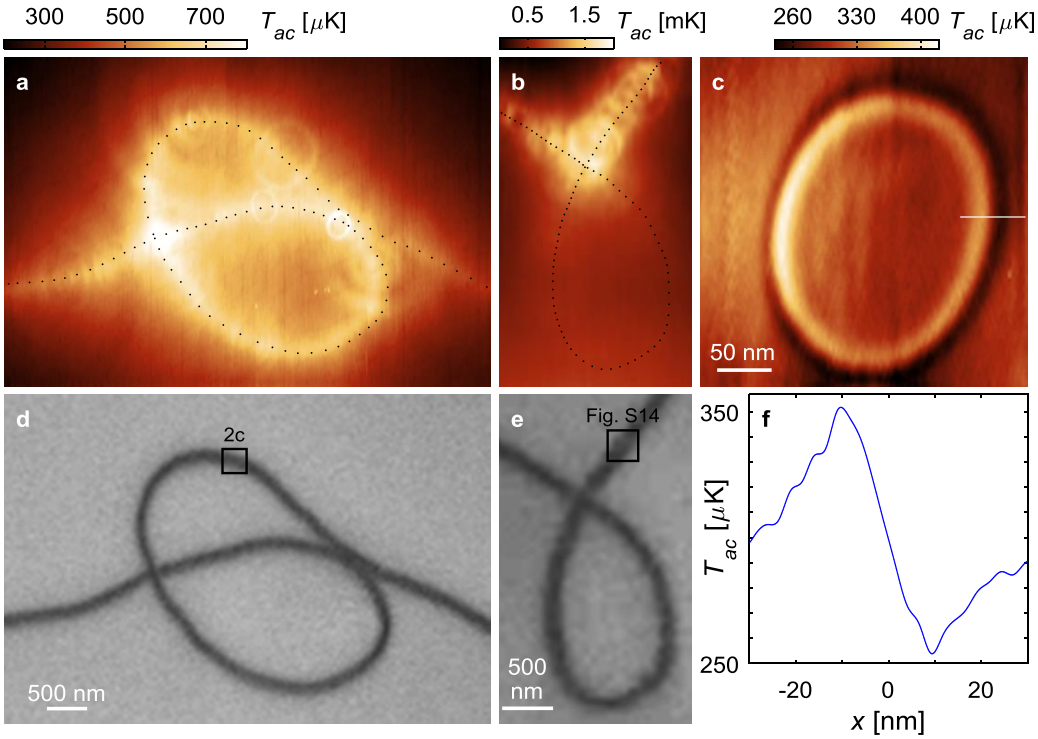

Figure 14 | Thermal imaging of single-walled carbon nanotubes and scanning gate thermometry of quantum dots.

a-b, Thermal images of two CNT devices with loop geometry carrying I_{ac} of 12 nA (a) and 3 nA (b) revealing an electrical short at the loop intersection point in (b). The $T_{ac}(x, y)$ was acquired by tSOT of 104 nm diameter at scanning heights of about 65 nm (a) and 150 nm (b). The ring-like structures in T_{ac} result from variations in dissipation due to modulations in the single-electron charging of individual QDs as described in (c). **c**, Zoomed-in scanning gate thermometry image of a single QD in the area marked in (d) at a scan height of about 35 nm. Variations in the chemical potential of the QD induced by the scanning tSOT give rise to changes of the temperature of the QD at the Coulomb blockade peak conditions along the equipotential ring-like contour. **d-e**, SEM images of the devices in (a) and (b). **f**, Line-cut across the line marked in (c).

In addition to the scanning *dc* gate thermometry demonstrated in Figure 14 in which the potential of the tSOT was kept constant while an *ac* current was applied to the CNT, we have performed scanning *ac* gate thermometry with an *ac* voltage of 80 mV at 130 Hz applied to the tSOT, while a *dc* current of 1.7 nA flowed through the CNT device 2. In this case the heat signal at the excitation frequency is generated only locally due to the small induced changes in the local conductance, reducing the background signal due to the overall *ac* heating of the CNT observed in Figure 14a,b. Figure 15a-c present the T_{ac} images produced by this technique at three different heights h of the tSOT above a CNT segment marked by square in Figure 14e. The height h was incremented by 2 nm between the images. As expected, the diameter of

the Coulomb blockade rings of the QDs grows with h. Clearly the ring structure is far from circular. In all cases, the short axis of the asphericity of the rings is aligned with the direction of the CNT; a feature that may be explained by partial screening of the tSOT potential by neighboring QDs along the CNT. In addition, during the scan of Figure 15b an abrupt change occurred, which caused some rings to shrink by one period while other rings remained unchanged (scans are along vertical lines from right to left). This observation reveals instability, typical for QDs, in which the charge of one QD is abruptly changed without affecting the rest of the QDs, demonstrating the ability of scanning gate thermometry to resolve changes in dissipation arising from variations in single electron occupancy of a QD.

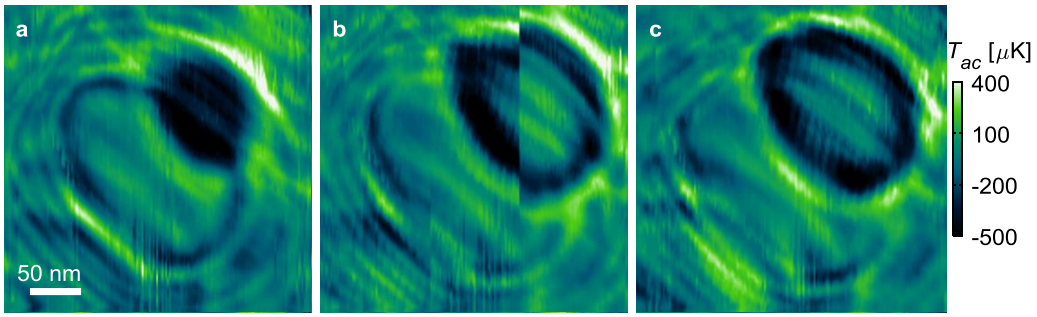

Figure 15 | Thermal imaging by scanning *ac* gate thermometry of quantum dot dissipation in SWCNT.

a-c, T_{ac} images of a segment along CNT device 2 (marked by square in Figure 14e) arising from changes in QDs dissipation induced by an *ac* potential applied to the tSOT in presence of *dc* current of 1.7 nA in the CNT. The height of the tSOT above the CNT was increased by 2 nm between the consecutive images, starting from about 15 nm in (a), resulting in expansion of the Coulomb blockade rings. During scan (b) an abrupt jump in the charge occupancy of one of the QDs occurred without affecting the dissipation in other QDs. Pixel size 1.8 nm and scan speed 10 nm/s.

3.4 Discussion

The tSOT can be used as a highly sensitive thermometer, with unprecedented sensitivity (section 3.2.2). Its unique thermal properties allow, in contrast to other scanning thermal microscopy techniques, to make a non-invasive thermal measurement. Consequently, the temperature reading of the tSOT is in congruence with the local temperature (section 3.2.4). The scan is performed without contact, where heat flow between sample and tSOT is performed by ballistic flow of helium atoms. At scanning heights, such a measurement scheme provides a spatial resolution comparable to the tSOT diameter (section 3.2.5). The bandwidth of the measurement is much larger than other SThM techniques, and in principle can be significantly

improved by using different electronics (section 3.2.8). The attachment of the tSOT to a tuning-fork resonator allowed height control of the scans (mostly in part II of the work) down to a few nm's above the sample surface.

Several measurement schemes were demonstrated:

- Simultaneous measurement of magnetic and thermal signals (section 3.2.7).
- 'tSOT heater' mode, which can be used to probe topography, material interfaces and heat pathways in samples (section 3.2.11).
- 'Scanning gate thermometry': allowing nanoscale manipulation of the potential and study of the induced changes in the local scattering processes and dissipation that are inaccessible by other methods (this technique was widely used in Part II).

The tSOT thus has great promise for uncovering the microscopic origins of dissipation in novel states of matter. Part II presents a work on dissipation processes in graphene heterostructures. Other systems of interest are topologically protected surface states, edge states in quantum spin and anomalous quantum Hall systems, and surface states in Weyl semimetals. By choosing appropriate superconducting materials[28,29,33] it should be possible to extend the operating temperature range of the tSOT from tens of mK to tens of K (Figure 2d) thus allowing investigation of a wide range of quantum systems. In addition, the operation of the tSOT at elevated magnetic fields combined with the multifunctional abilities of magnetic sensing and scanning gate thermometry opens the way to nanoscale investigation and imaging of intricate thermoelectric and thermomagnetic phenomena including Nernst effect, thermal Hall effect, thermoelectric nanoscale cooling and quantum heat conductance.

4 Part II - Imaging and controlling dissipation from individual atomic defects in graphene

4.1 Introduction

Understanding microscopic mechanisms of momentum and energy dissipation is a central problem in the fields ranging from condensed matter to particle physics. It is also of keen interest for designing new approaches to handle, convert, and utilize energy in a bid to address key technological challenges. Dissipation pathways are particularly intriguing in ultrapure materials of current interest, such as graphene[46], because of tight restrictions on the phase space for electron-phonon scattering[47–49]. Furthermore, unlike particle physics where a particular decay process of interest can be "staged" in a collider, in condensed matter physics we are interested in microscopically concealed processes within the material. This, along with the minute power released in such processes, poses a key challenge for experimentally probing dissipation at the nanoscale. In this part we employ the developed nano-thermometry technique to probe these subtle effects in ballistic graphene. Graphene, owing to its exceptional cleanliness and the two-dimensional nature of its electrons and phonons[46], is an excellent platform to study electron-phonon relaxation. In our measurement, we directly observe inelastic electron scattering from single-atomic defects, gaining a unique insight into the microscopic dissipation processes in this material.

Our key finding[50] is that the dissipation process in pristine graphene is dramatically affected by the extrinsic mechanisms due to disorder. Our scanning thermometry technique allows us to identify individual atomic-scale defects which mediate the energy transfer between electrons and phonons. As discussed below, the observed characteristics of the defect-dominated dissipation lend strong support to a microscopic model which involves exotic electronic states of "sp^3 band vacancies" originating from an adatom bonding to a single C atom and transforming its sp^2 orbital to an sp^3 state[51–54]. These defects host nearly particle-hole-symmetric zero mode states forming sharp resonances at energies near the Dirac point[55,56]. While such defects have been extensively investigated[57,58], their prominent role in dissipation has not been anticipated by previous work.

4.2 Methods

4.2.1 Sample fabrication

Our measurements were performed on ballistic graphene encapsulated between hexagonal Boron Nitride (hBN) layers and designed to inject electrons from narrow constrictions into a micron-scale "electron chamber" (Figure 19a,b). The samples were fabricated by Dr. Moshe Ben-Shalom at the group of Prof. Andre Geim at the University of Manchester. Transport measurements in such samples routinely show ballistic signatures over a wide range of temperatures and charge densities[59–61]. The graphene device was made from single-layer graphene placed atop a relatively thick (~30 nm) crystal of hexagonal boron nitride (hBN), and covered by a thinner (~10 nm) hBN. The heterostructures are assembled using the dry-peel technique on top of an oxidized Si wafer (90 nm of SiO2) which served as a back gate, and then annealed at 300 C in Ar-H_2 atmosphere for 3 hours. After this, a PMMA mask is designed by electron beam lithography to define the heterostructures' boundaries and, in a similar step, to define the metal contacts positions. The exposed heterostructure is etched by a reactive ion plasma combination of CHF_3 and O_2. The contacts (~50 nm of superconducting Nb) were deposited onto exposed graphene edges that were a few nm wide and located far from the imaging chamber (~10 μm away). Such quasi-one-dimensional contacts to graphene have notably low contact resistance[62], reducing local heating at the contacts. On the other hand, the etching parameters for defining the imaging chamber geometry, was optimized to minimize the step in graphene to about 1 nm.

The fabrication procedure results in high-quality samples with momentum-relaxation mean free path that is limited by the chamber dimensions over a wide range of carrier concentrations and temperatures[61]. The studied sample in Figure 19 consisted of a square-shaped chamber of 4×4 μm^2 with three constrictions connected to external electrical contacts (right square chamber in Figure 13b). The three contact points to the chamber are insufficient to perform a four-probe measurement of its transport properties. The top constriction, however, had additional contacts above it (see Figure 13b), which allowed us to carry out four-probe measurement of its magnetoresistance as a function of V_{bg} as shown in Figure 16. The quantum Hall oscillation data allow us to extract the back-gate capacitance to the graphene $C_{bg} =$

$1.25 \cdot 10^{11}$ 1/cm^{2}V and the charge neutrality point (CNP) of the constriction, $V_{bg}^{CNP} = -0.26$ V. The CNP of the 500 nm wide constriction, however, may differ from the CNP in the square bulk chamber which we estimate to be $V_{bg}^{CNP} = 0.48$ V as described in section 4.4.1 below.

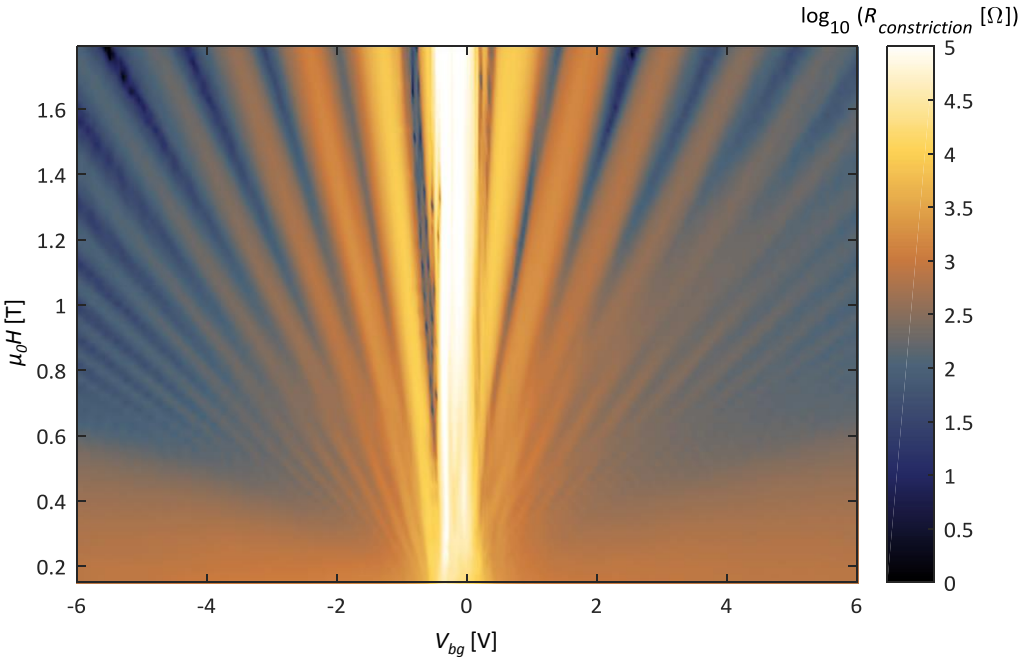

Figure 16 | Magneto transport characterization of the graphene sample.

Four-probe measurement of R_{xx} of the top constriction of the sample in Fig. 1B vs. back gate voltage V_{bg} and the perpendicularly applied magnetic field H at $T = 4.2$ K, showing quantum Hall oscillations. A linear fit to the QH minima results in back gate capacitance of $C_{bg} = 2 \cdot 10^{-4}$ F/m^2.

4.2.2 Characterization of tSOT device used for part II

For the following measurement we used a tSOT with an effective diameter of 33 nm and thermal sensitivity of 510 nK/Hz$^{1/2}$ at 4.2 K, to obtain an image of the local temperature variations $\delta T(x, y)$ upon scanning at a height h of 10 to 40 nm above the sample surface. The tip is mounted on a quartz tuning fork (section 3.2.10) which can vibrate the tSOT parallel to the sample surface with a controlled amplitude x_{ac}, at a frequency of ~37 kHz. The resulting *ac* signal, $T_{ac}(x, y) = x_{ac}\partial\delta T(x, y)/\partial x$, renders higher sensitivity imaging (Figure 19c) by avoiding the low-frequency $1/f$ noise of the tSOT (see section 4.2.3 for more on thermal imaging schemes). We control the carrier density in graphene globally by back-gate biasing the Si/SiO$_2$

substrate by V_{bg} and locally by applying V_{tg} potential to the tSOT (Figure 19a). Description of sample fabrication is provided in section 4.2.1 above.

Figure 17a shows a SEM image of the tSOT device used for part II. The I-V characteristics of the tSOT at 4.2 K are shown in Figure 17c at various applied magnetic fields. The electrical scheme (inset of Figure 17c) was slightly modified relative to Figure 2b to allow applying a controlled gate voltage with the tSOT. The interference pattern of the critical current $I_c(H)$ in Figure 17d shows the central lobe of period 2.4 T corresponding to effective tSOT diameter $d = 33$ nm. The higher lobes are suppressed and truncated by the upper critical field $H_{c2} = 1.73$ T of the Pb film. The magnetic and thermal sensitivities of the tSOT were characterized as described earlier and in Refs. 28,30. The flux noise of the tSOT in the white noise region above about 1 kHz at 4.2 K was 145 $n\Phi_0/Hz^{1/2}$ at applied field $\mu_0 H = 0.56$ T corresponding to spin noise of 0.85 $\mu_B/Hz^{1/2}$, and the thermal noise at zero field was 510 $nK/Hz^{1/2}$. The thermal coupling between the tSOT and the sample was provided by 60 mBar of He exchange gas[30].

The tSOT was attached to a quartz tuning fork (TF) as shown in Figure 17b, with a resonance frequency $f_{TF} = 36.9867$ kHz. As the tip approaches the sample surface to within a few nm, a shift in f_{TF} and in the phase is detected and used as a feedback for height control (see section 3.2.10). Scanning was performed at a fixed height h of 10 to 40 nm above the surface of the hBN with the TF feedback switched off.

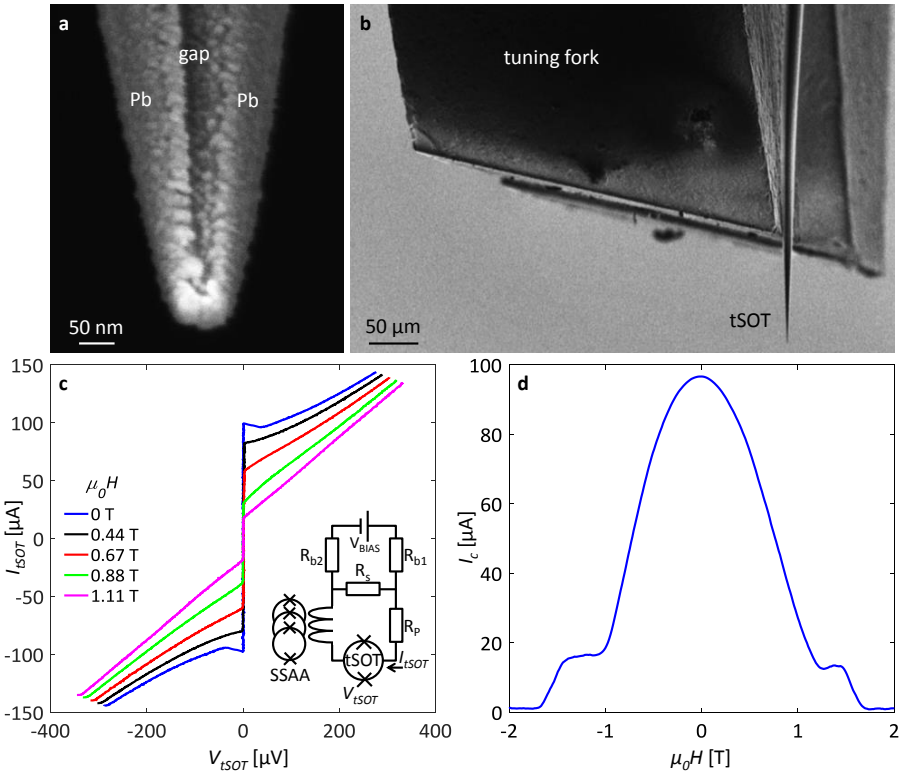

Figure 17 | tSOT of part II characterization.

a, SEM image of the tSOT used in this work showing two Pb leads connecting to the Pb ring at the apex of the tip and the gap between them. **b**, SEM image of the tSOT pipette attached to one tine of the quartz tuning fork. **c**, I-V characteristics of the tSOT at 4.2 K and various applied magnetic fields. The inset shows a simplified measurement circuit which includes the bias source V_{BIAS}, bias resistors $R_{b1} = R_{b2} = 11$ kΩ, shunt resistor $R_s = 5.4$ Ω, parasitic resistance $R_p = 0.6$ Ω, and the inductively coupled SSAA. **d**, Quantum interference pattern of the critical current $I_c(H)$ showing a period of 2.4 T corresponding to effective diameter $d = 33$ nm of the tSOT. The higher lobes of the interference pattern are suppressed by H_{c2} of Pb.

4.2.3 Thermal imaging schemes

In order to avoid the $1/f$ noise of the tSOT, in addition to the *dc* δT measurement, the studies presented in this part employed T_{ac} measurements using two methods. The first method uses the spatial *ac* oscillation of the tSOT, x_{ac}, parallel to the sample surface due to the excitation of the TF at its resonance frequency f_{TF}. The resulting measured T_{ac}^{TF} reflects the local temperature gradient along the vibration direction of the TF, $T_{ac}^{TF}(x,y) = x_{ac}\partial\delta T(x,y)/\partial x$. If x_{ac} is sufficiently small and $T_{ac}^{TF}(x,y)$ is imaged over a sufficiently large area, the *dc* temperature variation can be reconstructed by integration $\delta T(x,y) = \int^{x} dx' T_{ac}^{TF}(x',y)\,/x_{ac}$. Such integration,

however, is usually unnecessary since the essential information can be readily extracted directly from T_{ac}^{TF}.

In the second method we apply an *ac* potential V_{tg}^{ac} to the tip in addition to the *dc* V_{tg}, which measures the change in the local temperature in response to a change in the tip potential, $T_{ac}^{tg}(x,y) = V_{tg}^{ac} d\delta T(x,y)/dV_{tg}$. By measuring T_{ac}^{tg} vs. V_{tg} at a fixed tip position the *dc* temperature variation $\delta T(V_{tg})$ can be attained by integration, $\delta T(V_{tg}) = \int^{V_{tg}} dV'_{tg} T_{ac}^{tg}(V'_{tg})$ which provides direct spectroscopic information on the LDOS of the dissipative states. The data presented in Figure 21d,e were attained by this method.

Simultaneous application of the three nanothermometry measurement methods is demonstrated in Figure 18, where the dissipation ring of defect 'C' (see Figure 19 and following discussion therein for more information regarding defects' induced dissipation in graphene heterostructures) was imaged by the tSOT while applying $x_{ac} = 2.7$ nm rms at $f_{TF} = 36.9829$ kHz and $V_{tg}^{ac} = 0.2$ V rms at $f = 1.09$ kHz. The *dc* thermal image $\delta T(x,y)$ in Figure 18a shows a ring of enhanced temperature as described schematically by the solid red line in Figure 22b. The *ac* signal in Figure 18b is given by $T_{ac}^{TF}(x,y) = x_{ac} d\delta T(x,y)/dx$ and described by the blue line in Figure 22b. Note that even though the span of T_{ac}^{TF} signal in Figure 18b is about three times lower than of δT in Figure 18a, the signal to noise ratio (S/N) is much higher due to the 1/f noise of the tSOT at low frequencies[28]. We therefore refrained from using the *dc* method in this work. Figure 18c shows thermal imaging using the *ac* tip gating method. Since varying tip potential V_{tg} changes the radius R of the ring, the resulting signal can be expressed as $T_{ac}^{tg}(x,y) = V_{tg}^{ac} dT(x,y)/dV_{tg} = (dR/dV_{tg}) V_{tg}^{ac} dT(r,\theta)/dr$, where r is the radial distance from the center of the ring. The two *ac* methods are thus equivalent to measuring two spatial derivatives of the *dc* image, $T_{ac}^{TF}(x,y) \propto dT(x,y)/dx$ and $T_{ac}^{tg}(x,y) \propto dT(r,\theta)/dr$.

In the studies presented in the results of part II we have mainly employed the TF *ac* method (Figure 18b) due to its superior S/N performance and operational convenience. Due to its frequent use throughout part II, T_{ac}^{TF} data is often referred to as T_{ac} for brevity.

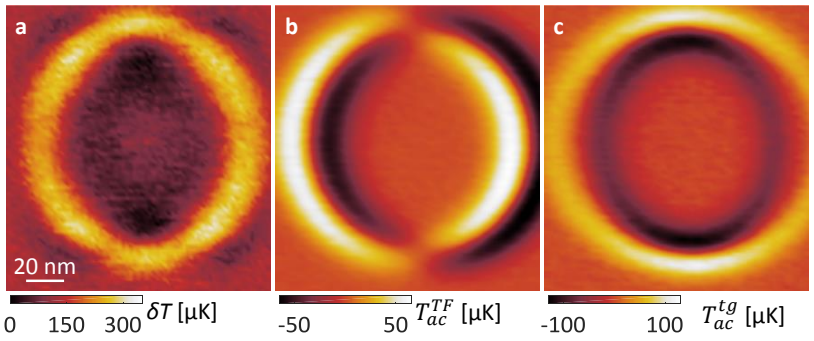

Figure 18 | Demonstration of simultaneous measurement by three thermal imaging methods.

a, A dc thermal image $\delta T(x,y)$ of the dissipation ring of defect 'C' (after background subtraction). **b**, An *ac* thermal image using the TF x_{ac} tip oscillation, $T_{ac}^{TF}(x,y) = x_{ac} d\delta T(x,y)/dx$. **c**, An ac thermal image using V_{tg}^{ac} tip gate modulation, $T_{ac}^{tg}(x,y) = V_{tg}^{ac} dT(x,y)/dV_{tg}$. Scan area 140 × 150 nm^2, pixel size 1.9 nm, scan speed 20 ms/pixel, $h = 20$ nm, $V_{bg} =$ -2 V, $V_{tg} = 5$ V, $I_{dc} = 3$ μA, $x_{ac} = 2.7$ nm, $V_{tg}^{ac} = 0.2$ V.

4.3 Results

4.3.1 Dissipation sources in a graphene heterostructure

Next we performed tSOT (of section 4.2.2) thermal imaging of the hBN encapsulated graphene sample described earlier (section 4.2.1). Figure 19c shows the thermal signal $T_{ac}^{TF}(x,y)$ measured while applying a fixed current $I_{dc} = 3$ μA through two of the constrictions as shown in Figure 19b. The image reveals a complex array of fine rings along the edges of the heterostructure. In addition, three isolated rings are observed in the bulk of graphene labeled 'A', 'B', and 'C'. The bulk rings are rare and have comparable diameters, in sharp contrast to the rings at the edges that are dense and display widely varying sizes as demonstrated in Figure 20. The sharp ring-like structures have the same origin as the ring-like patterns in CNT in Figure 14a-c, unveiling the presence of electronic localized resonant states at the edges of graphene. This suggests one of two options: The first is that as in the case of CNT the current is forced through these states. However, no magnetic field was applied throughout the measurements of Part II, so we have no reason to suspect that the edges might be dominant channels of conduction. We expect the bulk to shunt the device in case conduction along the edges decreases, and therefore such dissipation features should not appear along the edges. Since dissipation happens not where the current flows we are lead to consider a second possibility, that this observation is governed by

collisions of ballistic electrons. Indeed, we show below that the rings mark dissipation from single atomic defects positioned at their centers.

Another apparent feature in Figure 19c is a strip of bright background $T_{ac}^{TF}(x,y)$ signal along the left edge of the sample and a negative strip along the right edge. This suggests the bulk of the sample has a uniform background $\delta T(x,y)$ temperature (not affected by the local tip gating) that is slightly higher than that of the surrounding SiO_2 substrate. This small step-wise change in $\delta T(x,y)$ at the sample edges translates accordingly to the observed features of $T_{ac}^{TF}(x,y)$.

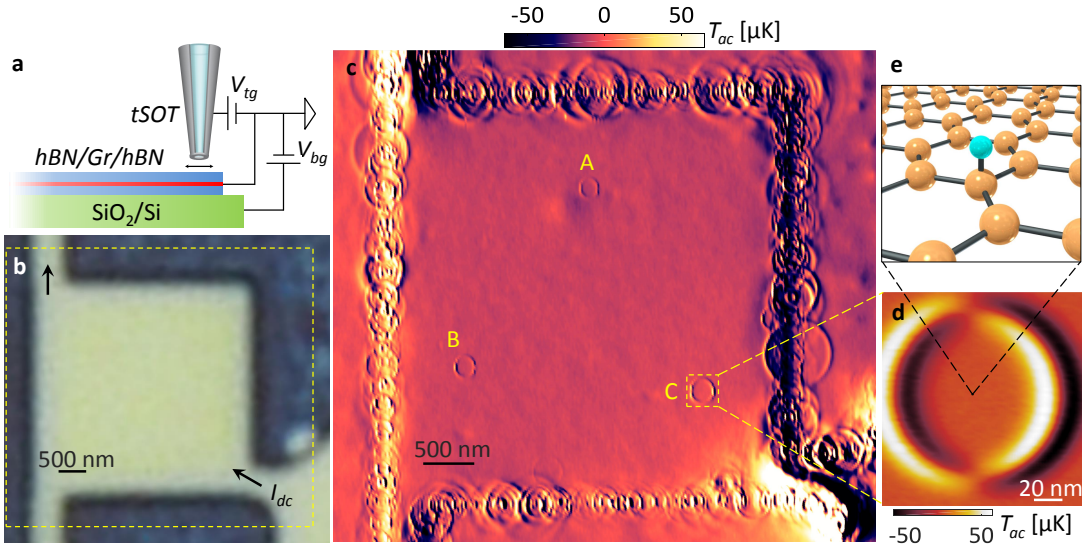

Figure 19 | Observing individual dissipation sources in a graphene heterostructure.

a, Schematic side view of the measurement setup with hBN-graphene-hBN heterostructure and SQUID-on-tip nanothermometer (tSOT). **b**, Optical image of the device patterned into 4×4 μm^2 square chamber (bright). A fixed current $I_{dc} = 3$ μA is driven through the connecting constrictions (arrows). **c**, Scanning ac nanothermometry $T_{ac}^{TF}(x,y)$ of the 5.5 × 5 μm^2 area outlined in (B) at $V_{bg} = -2$ V and $V_{tg} = 9$ V at 4.2 K. The tSOT is scanned while oscillating with amplitude $x_{ac} =$ 2.7 nm at 12° to x axis (pixel size 18 nm, scan-speed 20 ms/pixel, $h = 20$ nm, $I_{dc} =$ 3 μA). The sharp rings (marked 'A','B','C') uncover three isolated sources of dissipation in the bulk of graphene in addition to a dense array of resonances along the graphene edges. **d**, Zoom-in on defect 'C' at $V_{tg} = 5$ V. **e**, Schematic image of an adatom to graphene that creates a localized resonant dissipative state at the center of the ring.

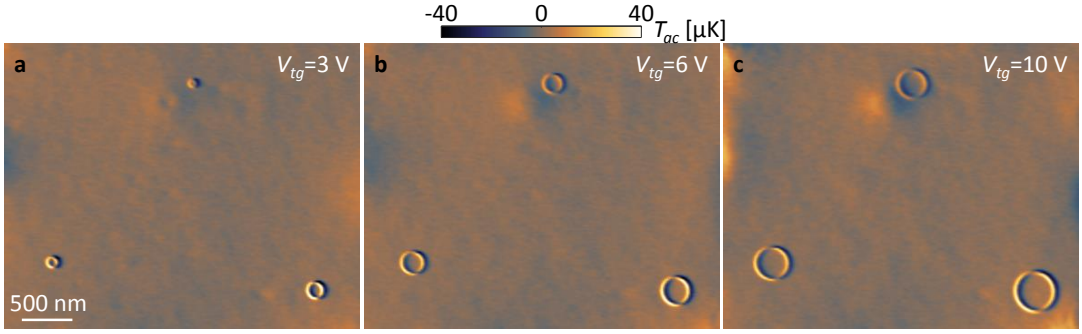

Figure 20 | Thermal imaging of resonant dissipation of three bulk localized states.

$T_{ac}(x, y)$ of the central part of hBN/graphene/hBN sample. Three resonant dissipation rings appear and expand upon increasing V_{tg} for 3V (a), 6V (b) and 10 V (c). Inelastic electron scattering from three individual atomic defects is revealed. The small differences in the onset potential of the rings can be ascribed to long-range substrate potential disorder modifying the local CNP. $V_{bg} = -1$ V, $I_{dc} = 3$ μA, $h = 20$ nm, $x_{ac} = 2.7$ nm, scan area 3.5 × 2.8 μm^2, pixel size 17.5 nm, scan-speed 20 ms/pixel.

4.3.2 Dissipative localized states in graphene heterostructures

We start with comparing possible dissipation pathways in graphene. Owing to the exceptional stiffness of the carbon bonds, scattering by optical phonons in graphene is inefficient below room temperature. Moreover, the small size of the electron's Fermi surface restricts the phase volume for scattering by acoustic phonons, blocking the intrinsic electron-lattice relaxation pathway[47–49]. Disorder, however, can significantly ease the electron-phonon scattering[49]. A disorder-related localized state (LS) can produce inelastic electron scattering at a rate proportional to the local density of states (LDOS) $D_{LS}(E)$ near the Fermi energy E_F, as illustrated schematically in Figure 21a-c. By parking the tSOT above a defect and varying V_{tg} we can induce local band bending and shift the $D_{LS}(E)$ with respect to E_F (see Appendix 5). The resulting variation in measured temperature $\delta T(V_{tg})$ due to changes in the inelastic scattering rate will thus provide a spectroscopic measurement of the $D_{LS}(E)$ (Figure 21b). Tuning E_F by the back-gate V_{bg} will further reveal the peaks in $D_{LS}(E)$ in the form of diagonal resonant lines in the $\delta T(V_{tg}, V_{bg})$ map as exemplified in Figure 21c.

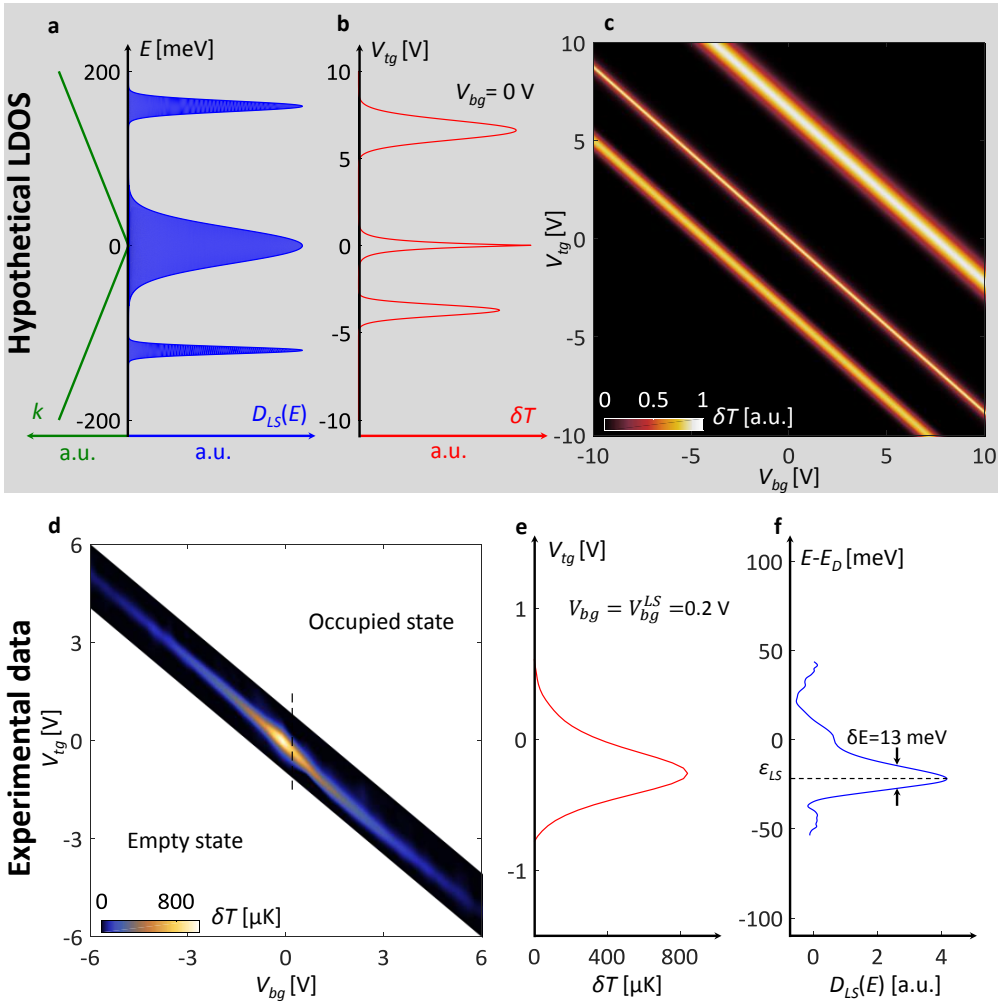

Figure 21 | Thermal nanospectroscopy of dissipative localized states.

a, A hypothetical spectrum of density of localized states $D_{LS}(E)$ (blue) and the graphene Dirac dispersion relation (green). **b**, The expected temperature variation $\delta T(V_{tg})$ measured above the defect vs. tip potential V_{tg} providing nanoscale spectroscopy of $D_{LS}(E)$ by tip-induced band bending. **c**, The expected $\delta T(V_{bg}, V_{tg})$ showing diagonal resonance lines that map the peaks in $D_{LS}(E)$. **d**, The experimental $\delta T(V_{bg}, V_{tg})$ measured by the tSOT at $h = 10$ nm above defect 'C' in presence of $I_{dc} = 3$ µA, revealing a single resonance dissipation line. **e**, A zoomed-in line cut $\delta T(V_{tg})$ along the dashed line in (**d**) at $V_{bg} = V_{bg}^{LS} = 0.2$ V. **f**, The spectral density, $D_{LS}(E)$, derived from measurement of the resonant dissipation ring (section 4.4.2) showing a single sharp peak near the Dirac point at $\varepsilon_{LS} = -22$ meV.

The experimental $\delta T(V_{tg}, V_{bg})$ map of defect 'C' is presented in Figure 21d. Interestingly, it displays a sharp resonance (Figure 21e) along a single diagonal line, which passes closely to the origin in the V_{tg}-V_{bg} plane. This resonance is due to the presence of a LS with a narrow single peak in $D_{LS}(E)$ (Figure 21f) close to the Dirac energy E_D (section 4.4.1). Such LS's give rise to the sharp thermal rings observed in

Figure 19c as follows. In order for the LS to cause inelastic electron scattering its energy level E_{LS} has to be aligned with the energy of the impinging electrons, $E_e \cong E_F$. For a given tip potential V_{tg} this resonant condition occurs when the tip is located at a distance R from a LS (Figure 22a and Appendix 5). As a result, each LS displays a sharp peak in $\delta T(x,y)$ and $T_{ac}(x,y)$ along a ring of radius R as shown in Figure 22b, describing the ring formations in Figure 19c and Figure 22c (also see Appendix 4). The tip gating combined with the resonant nature of the LS thus render a unique ability of local on and off switching of the inelastic electron scattering by individual defects allowing control of dissipation at the nanoscale.

We now focus on the spectroscopic analysis of bulk defect C revealed by its dissipative ring in Figure 18, as a mean to extract the energy level and the LDOS of the LS. By repeatedly scanning the tSOT along the line crossing the defect and incrementing V_{tg} we derive the tip-gate dependence of the ring radius $R(V_{tg})$ as shown in Figure 23a-c. In the case of $V_{bg} = 2.5$ V (Figure 23c), the concave trace reflects the situation exemplified in Figure 22 where in absence of tip potential E_{LS} resides below E_F and hence the LS is occupied and does not dissipate until a negative V_{tg} brings it into resonance with E_e. Decreasing V_{tg} further empties the state and brings E_{LS} above E_e thus preventing dissipation again. However, by moving the tip away from the defect the resonance is restored at a distance $R(V_{tg})$ that grows with decreasing V_{tg}. For $V_{bg} = -1$ V (Figure 23a), the opposite situation occurs in which the empty state does not dissipate because it is well above E_e and a positive V_{tg} is required for bringing it into resonance resulting in a convex trace. The transition from convex to concave traces upon varying V_{bg} is presented in Figure 23b. Alternatively, the tSOT can be scanned through the defect while incrementing V_{bg} at constant V_{tg} (Figure 23d-f). In this case the traces are bell-shaped with diverging R when $V_{bg} = V_{bg}^{LS}$. These data are summarized in Figure 23g showing the ring radius R in the V_{bg}-V_{tg} plane. In the white areas no dissipation is present since E_{LS} is far from resonance. In the colored regions inelastic scattering occurs depending on the tip position. The transition line maps the resonant conditions when the tip is positioned directly above the defect ($R = 0$) as in Figure 21d, while the red color reflects the conditions for diverging R. The black dot describes the bare resonance point V_{tg}^{FB}, V_{bg}^{LS} at which V_{tg} corresponds to flat-band conditions of the tip and V_{bg} aligns E_{LS} with E_e in absence of tip potential.

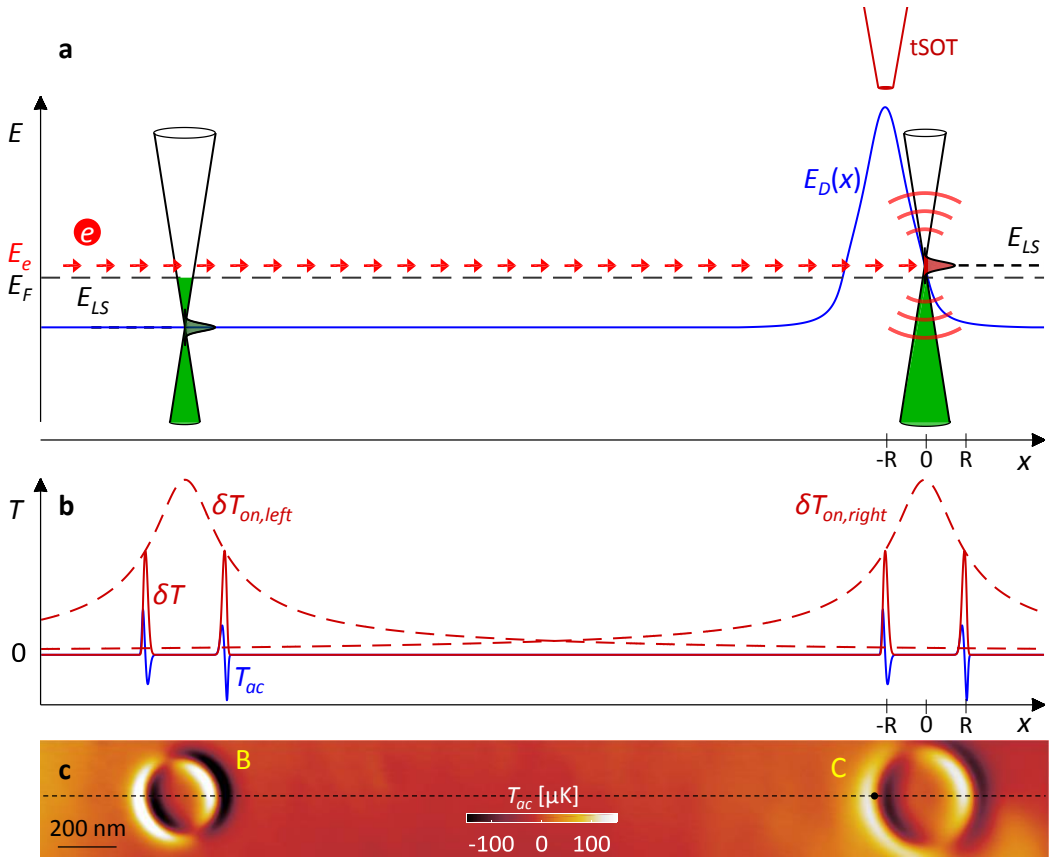

Figure 22 | Origin of the resonant ring structures.

a, Schematic description of the systems' energy levels corresponding to tip position marked by black point in (**c**): Two localized states with a peak in LDOS at E_{LS} pinned to Dirac energy E_D. The tip potential V_{tg} induces band-bending resulting in the calculated position-dependent $E_D(x)$ (blue). The left LS is off resonance while the tSOT positioned at $x = -R$ brings the right LS into resonance for inelastic scattering of electrons injected at energy E_e (red arrows). The result is a point-source of phonon emission (red arcs). The Fermi energy E_F (dashed) is determined by the back gate voltage V_{bg}. **b**, Dashed: Schematic temperature profiles $\delta T_{on}(x)$ at resonance conditions for inelastic scattering from the LS's. Red: Calculated temperature variation $\delta T(x)$ as would be measured by the scanning tSOT that brings the LS into resonance at a distance $\pm R$ from each defect. Blue: Calculated $T_{ac}(x) = x_{ac} dT(x)/dx$ measured by the tSOT vibrating parallel to the surface. **c**, $T_{ac}(x, y)$ measured in the central region of Figure 19c showing dissipation rings around defects 'B' and 'C' (scan area 3.5 × 0.4 μm^2, pixel size 8 nm, scan-speed 20 ms/pixel, $h = 20$ nm, $V_{bg} =$ -0.3 V, $V_{tg} = 5.5$ V, $I_{dc} = 6$ μA and $x_{ac} = 2.7$ nm). The dashed line describes the scan direction depicted in (a). The direction of x_{ac} tip oscillation was at 18° to the x-axis.

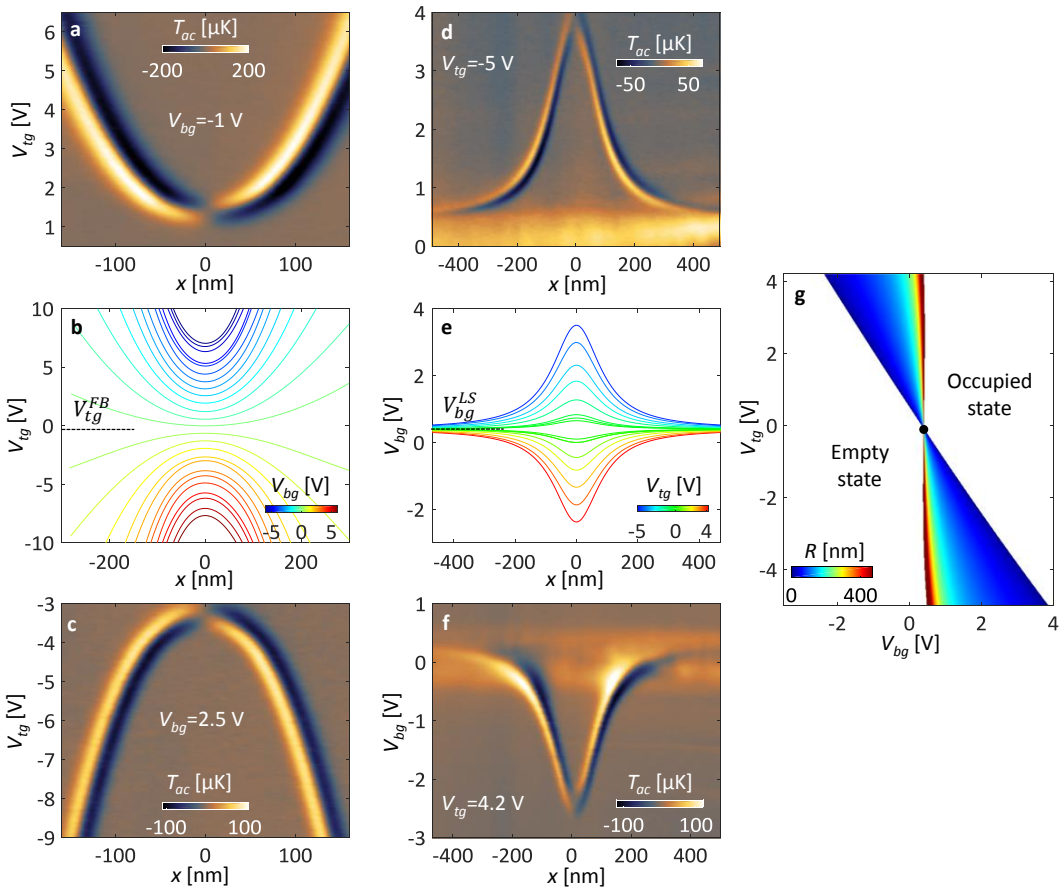

Figure 23 | Thermal spectroscopy of a single localized state.

a, Map of $T_{ac}(x)$ line scans through the center of the ring upon varying V_{tg} at constant $V_{bg} = -1$ V. Pixel width 3 nm, pixel height 50 mV, scan-speed 60 ms/pixel, $h = 20$ nm. **b**, The resulting resonance traces $R(V_{tg})$ for various values of V_{bg}. The transition from convex to concave traces occurs at V_{bg}^{LS}, V_{tg}^{FB}. **c**, Map of $T_{ac}(x)$ line scans as in (a) at $V_{bg} = 2.5$ V. **d**, Map of $T_{ac}(x)$ line scans through the LS upon varying V_{bg} at constant $V_{tg} = -5$ V. Pixel width 5 nm, pixel height 30 mV, scan-speed 20 ms/pixel, $h = 20$ nm. **e**, The resulting bell-shaped resonance traces $R(V_{bg})$ for various values of V_{tg} that change their polarity at V_{bg}^{LS}, V_{tg}^{FB}. **f**, Map of $T_{ac}(x)$ line scans as in (d) at $V_{tg} = 4.2$ V. **g**, Measured dissipation ring radius $R(V_{bg}, V_{tg})$ of the LS along with the V_{bg}^{LS}, V_{tg}^{FB} point (black dot).

4.4 Discussion

4.4.1 Derivation of local CNP and of energy level of bulk localized state

The LS resonance line in Figure 21d provides a valuable tool for determining the local charge neutrality point (CNP) in terms of V_{bg}^{CNP} and the energy level E_{LS} of the LS in terms of V_{bg}^{LS}. To describe the derivation method we carry out numerical simulations of the resonance line, which is the critical line at which the dissipation ring nucleates from $R = 0$.

We first assume that the LS's energy is pinned to the Dirac point, $\varepsilon_{LS} = E_{LS} - E_D = 0$ (as predicted in the literature[51] due to electron-hole symmetry). In this case the resonance curve is defined by the geometric place of all the V_{bg}, V_{tg} pairs for which the $E_D(x)$ profile (the CNP profile) at the tip location $x = 0$ is equal to the Fermi energy $E_F = 0$ as shown in Figure 24a, such that the impinging electrons with energy $E_e \cong E_F$ are at resonance with the LS. The resulting $R = 0$ resonance curves are shown in Figure 24b for various heights z_{tip} of the tip above the graphene. The slope of the curves away from the CNP reflects the ratio between the effective capacitances C_{bg}/C_{tg} of the back and tip gating and is thus affected by z_{tip}. The intersection point of the curves defines the flat-band conditions of the tip V_{tg}^{FB} which depends on its work function and was taken to be zero in the simulations. At V_{tg}^{FB} the tip has no effect on the sample, $E_D(x)$ is constant, and the resonance occurs at $V_{bg} = V_{bg}^{LS}$ independent of the tip height. The crossing point thus determines the energy of the LS in terms of V_{bg}^{LS}.

The resonance curves are not straight and show a kink which is clearly resolved by plotting their derivatives (Figure 24c). This kink is the result of quantum capacitance and reflects the change in effectiveness of graphene in screening the tip potential at different V_{bg}. The kink occurs at the charge neutrality point V_{bg}^{CNP}, which is taken to be zero in the simulations, and is defined by the location of the minimum of the dV_{tg}/dV_{bg} curves (Figure 24c). In the $\varepsilon_{LS} = 0$ case, $V_{bg}^{LS} = V_{bg}^{CNP} = 0$ and hence the crossing point of the resonance curves coincides with the kink location, however, in the general case these two features are separated as demonstrated in Figure 24d-f for $\varepsilon_{LS} = 30$ meV. Here the crossing point of the curves is determined by the top-gate flat-band condition $V_{tg}^{FB} = 0$ at which $V_{bg} = V_{bg}^{LS}$, while the kink is fixed by the back gate CNP, $V_{bg}^{CNP} = 0$ (Figure 24e-f).

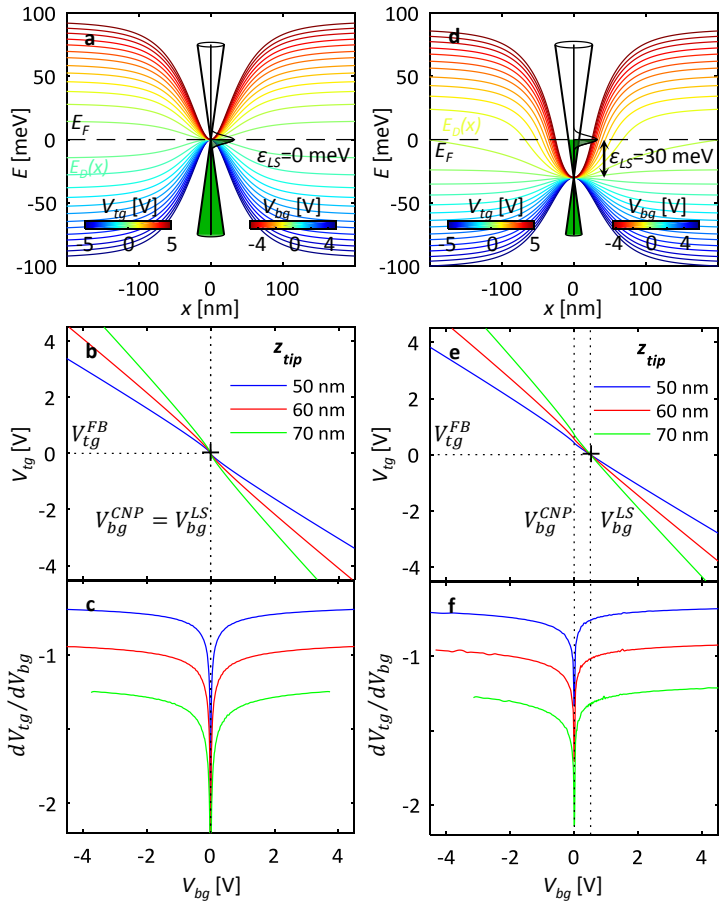

Figure 24 | Numerical simulation of resonance lines of LS.

a, Band bending $E_D(x)$ induced in graphene by the tSOT located at $x = 0$ at z_{tip} = 60 nm above the graphene for critical (V_{bg}, V_{tg}) pairs such that $E_D(x = 0) = 0$ providing resonance conditions for inelastic scattering from LS with $\varepsilon_{LS} = 0$ (all other simulation parameters are identical to Figure A5). Inset: Schematic Dirac cone with LS aligned with E_F. **b**, The resulting $R = 0$ resonance curves for different z_{tip} heights. The curves intersect at flat-band conditions determined by V_{tg}^{FB} and V_{bg}^{LS} (cross). **c**, Derivative of the resonance curves showing the kink location determined by the local CNP, V_{bg}^{CNP}. For $\varepsilon_{LS} = 0$ the crossing point coincides with the kinks. **d**, Same as (a) for the case of $\varepsilon_{LS} = 30$ meV. The resonance conditions are attained when $E_D(x = 0) = -30$ meV. **e-f**, Same as (b-c) for the case of ε_{LS} =30 meV. The kink and the crossing point are well separated and their difference, $V_{bg}^{LS} - V_{bg}^{CNP}$, provides a direct measure of ε_{LS}.

In the experimental resonance lines of defect 'C' in Figure 25d (and their derivative in Figure 25e) the two features are well resolved with resulting $V_{bg}^{LS} \cong 200$ mV and $V_{bg}^{CNP} \cong 480$ mV. We can use these values to get the carrier density (using C_{bg} as measured in section 4.2.1) of $n = C_{bg}\left|V_{bg}^{LS} - V_{bg}^{CNP}\right| = 3.5 \cdot 10^{10}\ {}^{1}/_{cm^2}$. And using the dispersion relation of graphene we derive the energy level of the LS to be

$\varepsilon_{LS} = E_{LS} - E_D = sign\left(V_{bg}^{LS} - V_{bg}^{CNP}\right)\sqrt{\pi}\hbar v_F\sqrt{n} \cong -22$ meV.

Figure 25a-c shows the corresponding numerical simulations for the case of $\varepsilon_{LS} = -20$ meV reproducing the experimental features. In order for the LS to be at resonance with the electrons at E_F the tip potential has to induce $E_D(x)$ profile such that $E_D(0) - E_F = 20$ meV (Figure 25a).

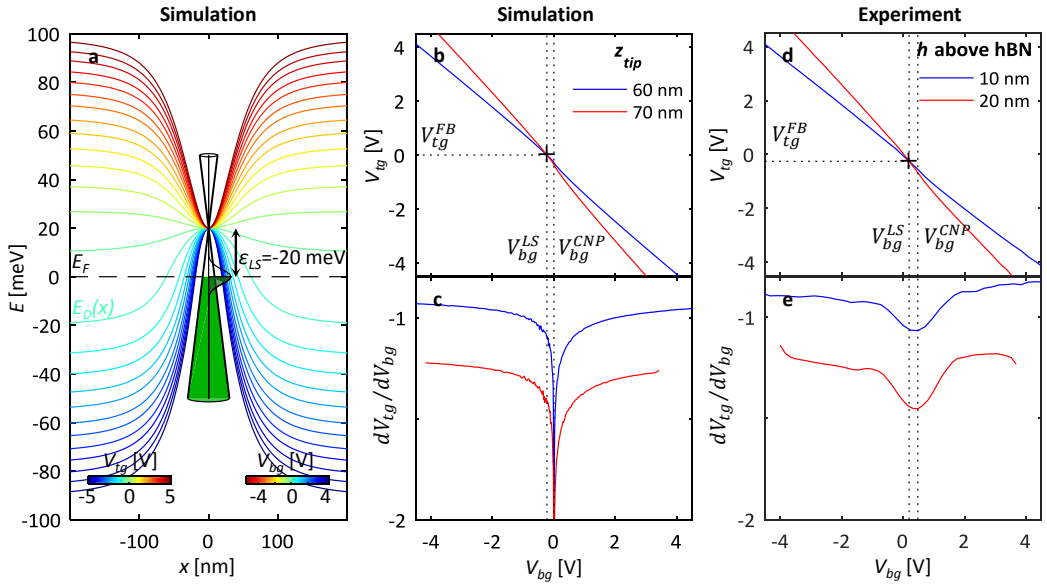

Figure 25 | Calculated and measured resonance lines of LS.

a, Calculated band bending $E_D(x)$ induced in graphene by the tSOT as in Figure 24 for the case of $\varepsilon_{LS} = -20$ meV. Inset: Schematic Dirac cone with LS aligned with E_F at resonance conditions. **b-c**, The resulting calculated resonance curves for different z_{tip} values **(**b**)** and the derivatives of the curves (c), showing the intersection and the kink points V_{bg}^{LS} and V_{bg}^{CNP}. **d**, Experimental resonance lines of defect 'C' extracted from the data of Figure 21d and a similar measurement performed at $h = 20$ nm above the hBN surface with otherwise the same measurement parameters, and their numerical derivatives (e). A kink is apparent at the local change neutrality point, $V_{bg}^{CNP} = 0.48$ V, defined by the minima in (e). Experimental curves intersect at $V_{bg}^{LS} = 0.2$ V and $V_{tg}^{FB} = -0.26$ V (indicated by the cross in (d)), resulting in $\varepsilon_{LS} = -22$ meV.

Theoretical calculations[52,53] have shown that hydrogen atoms on graphene give rise to sharply localized state at 30 meV below the Dirac point. Our derived $\varepsilon_{LS} \cong -22$ meV thus suggests that the observed resonant inelastic scattering in the bulk of graphene may arise from individual hydrogen adatoms.

Note that in graphene heterostructures the CNP is known to be hysteretic with respect to V_{bg}. Accordingly, V_{bg}^{CNP} and V_{bg}^{LS} are slightly dependent on the span of previously applied V_{bg} and on its sweep direction, giving rise to small variations in the apparent V_{bg}^{LS} in Figure 23d-f and Figure A6a-c. Since ε_{LS} is determined only by the difference $V_{bg}^{LS} - V_{bg}^{CNP}$ the above described procedure diminishes the effect of hysteresis by measuring the two quantities in a single continuous V_{bg} sweep.

4.4.2 Derivation of the LDOS of the localized state

Our thermal spectroscopy allows evaluation of the broadening δE of the energy level of the LS and derivation of its LDOS $D_{LS}(\varepsilon)$ as follows. For a LS that is pinned to the Dirac point, $E_{LS} = E_D$, a finite spectral width δE of the LS translates into a finite width of the back gate voltage δV_{bg}, $\delta E = 2\sqrt{\pi/e}\hbar v_F \sqrt{C_{bg}\delta V_{bg}/2}$, over which the dissipation occurs. This broadening translates into a finite width $\delta x = \delta V_{bg}/(dV_{bg}/dx)$ of the dissipation ring as described in Figure 26. In addition to the intrinsic broadening, however, there is an extrinsic broadening due to a finite energy distribution of the injected energetic carriers and the tSOT modulation x_{ac} by the TF.

In order to assess the extrinsic broadening and to minimize its contribution, we performed the measurements presented in Figure 26. Figure 26a shows the bell-shaped dissipation trace of defect 'B' at $V_{tg} = -10$ V. The back-gate voltage was then fixed to $V_{bg} = 5.3$ V, where the slope of the bell-shaped trace was $dV_{bg}/dx = 47$ mV/nm, as shown in Figure 26a. Next, we performed line scans through the LS and measured the width of the ring δx (Figure 26d) as a function of the rms amplitude of the tip oscillation x_{ac} as shown in Figure 26b. The resulting δx decreases linearly with decreasing x_{ac}, as expected when tip oscillation is larger than the intrinsic width of the ring, and saturates for $x_{ac} \lesssim 1.5$ nm. The average energy of the injected electrons $\varepsilon_e = E_e - E_D$ and the width of their energy distribution, which should be comparable to ε_e, is determined by R_c and the *dc* current I_{dc} by $\varepsilon_e = eR_cI_{dc}$, where $R_c = 890\ \Omega$ is resistance of the constriction at $V_{bg} = 5.3$ V (see Figure 16). Figure 26c shows that the ring width δx decreases with decreasing I_{dc} and saturates for $I_{dc} \lesssim$

5 μA. The corresponding dissipation ring measured in the limit of low tip oscillation of $x_{ac} = 0.5$ nm and low current $I_{dc} = 2$ μA is presented in Figure 26d (note the T_{ac} scale of just 1 μK). The cross section $T_{ac}(x)$ of the ring (Figure 26e) shows ring width of $\delta x = 7$ nm.

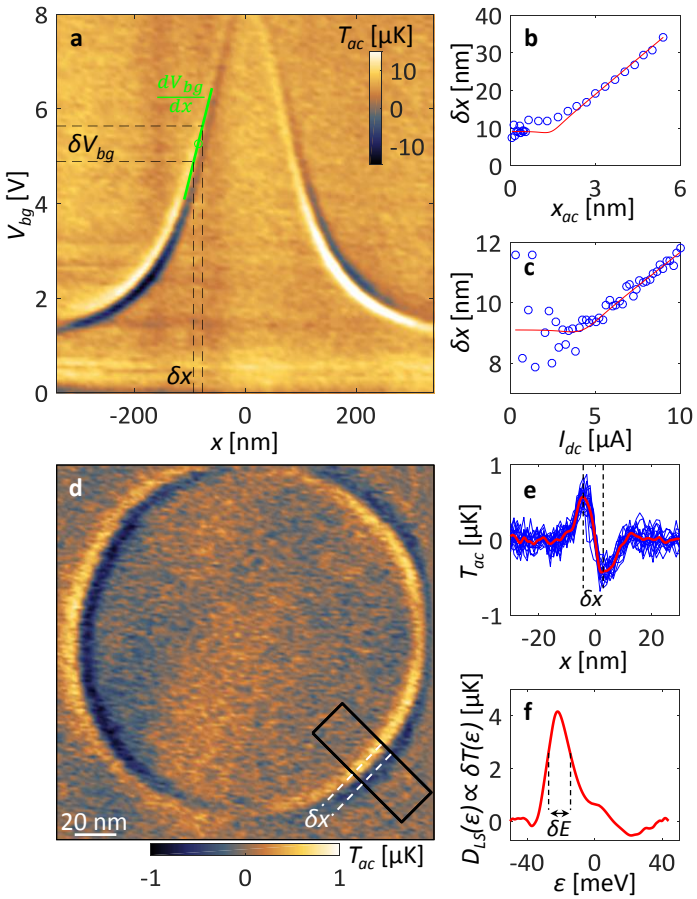

Figure 26 | Estimating the spectral width of the localized state.

a, Bell-shaped T_{ac} dissipation trace of defect 'B' at $V_{tg} = -10$ V, $h = 20$ nm, $x_{ac} = 2.7$ nm, and $I_{dc} = 3$ μA. The slope of the trace dV_{bg}/dx (at $V_{bg} = 5.3$ V, green line) translates the width of the ring, δx, into corresponding width δV_{bg} and δE of the LS. **b**, Width δx of the dissipation ring vs. the tip vibration rms amplitude x_{ac} at $I_{dc} = 3$ μA (red curve is a guide to the eye). **c**, Width δx of the dissipation ring vs. I_{dc} at $x_{ac} = 0.5$ nm. **d**, T_{ac} dissipation ring at $V_{tg} = -10$ V, $V_{bg} = 5.3$ V, $h = 20$ nm, $x_{ac} = 0.5$ nm, and $I_{dc} = 2$ μA (Scan area 180 × 180 nm^2, pixel size 1.2 nm, scan-speed 600 ms/pixel). **e**, Several line-cuts in the rectangle in (c) (blue, x-axis parallel to the long edge of the rectangle), and the average of the profiles (red) determining the width of the ring $\delta x = 7$ nm. **f**, The corresponding integrated $\delta T(x)$ that describes the LDOS of the LS, $D_{LS}(\varepsilon)$, with $\delta E = 13$ meV.

Assuming that the energy distribution of the impinging electrons is sufficiently narrow and the inelastic scattering rate is proportional to the density of states of the LS, we can directly derive the LDOS from the spectroscopic thermal signal, $D_{LS}(\varepsilon) \propto \delta T(\varepsilon)$. To attain this, we integrate the $T_{ac}(x)$ profile of Figure 26e to derive $\delta T(x) = \int^{x} dx' T_{ac}(x') / x_{ac}$, and use coordinate transformation to translate the lateral tip position x into the induced energy shift of the LS given by $|\varepsilon| = \sqrt{\pi/e}\hbar v_F \sqrt{C_{bg}\left|V_{bg}^{LS} - V_{bg}^{CNP} + x\, dV_{bg}/dx\right|}$, where dV_{bg}/dx is determined from Figure 26a, the origin of x is defined in Figure 26e, and $V_{bg}^{LS} - V_{bg}^{CNP}$ was taken from section 4.4.1 above. The resulting $\delta T(\varepsilon)$ is presented in Figure 26f and describes the LDOS of the LS, $D_{LS}(\varepsilon) \propto \delta T(\varepsilon)$, which shows a sharp peak with spectral width of $\delta E = 13$ meV. Since $\varepsilon_e = eR_c I_{dc} = 1.8$ meV $\ll \delta E$, the observed δE reflects an upper bound on the intrinsic broadening of the energy level of the LS. The derived $D_{LS}(\varepsilon)$ is presented in Figure 21f.

4.4.3 Summary of conclusions regarding localized states in graphene heterostructures

Our spectroscopic analysis of bulk LS's leads to the following conclusions: a) The LS's energy resides slightly below the Dirac point, $\varepsilon_{LS} = E_{LS} - E_D \cong -22$ meV, as derived from the analysis of the resonance lines (section 4.4.1). b) The spectral width of the localized state is no more than 13 meV (Figure 21f), as extracted from the minimal ring width of 7 nm (section 4.4.2). c) No additional LS energy levels are observed at least 180 meV above and below ε_{LS}. If present, additional concentric rings and bell-shaped traces would have formed. However, these are absent for the entire V_{bg} and V_{tg} applied range of ± 10 V (Appendix 6). d) This level spacing puts an upper bound on the spatial extent of the LS of less than 2 nm (Appendix 6). e) The sharp energy level and nanometer spatial extent of the LS closely resemble the characteristic features of atomic defects in graphene observed by STM[55,56] in contrast to more extended non-resonant "puddles" originating from disordered substrate potential[63,64]. f) The resonant character of the defects and the proximity of their energy level to Dirac point are consistent with the sp^3 band vacancy model. In particular, hydrogen adatoms are known to form LS at an energy value comparable with the observed value[53,55] and thus are strong candidates for the observed bulk defects.

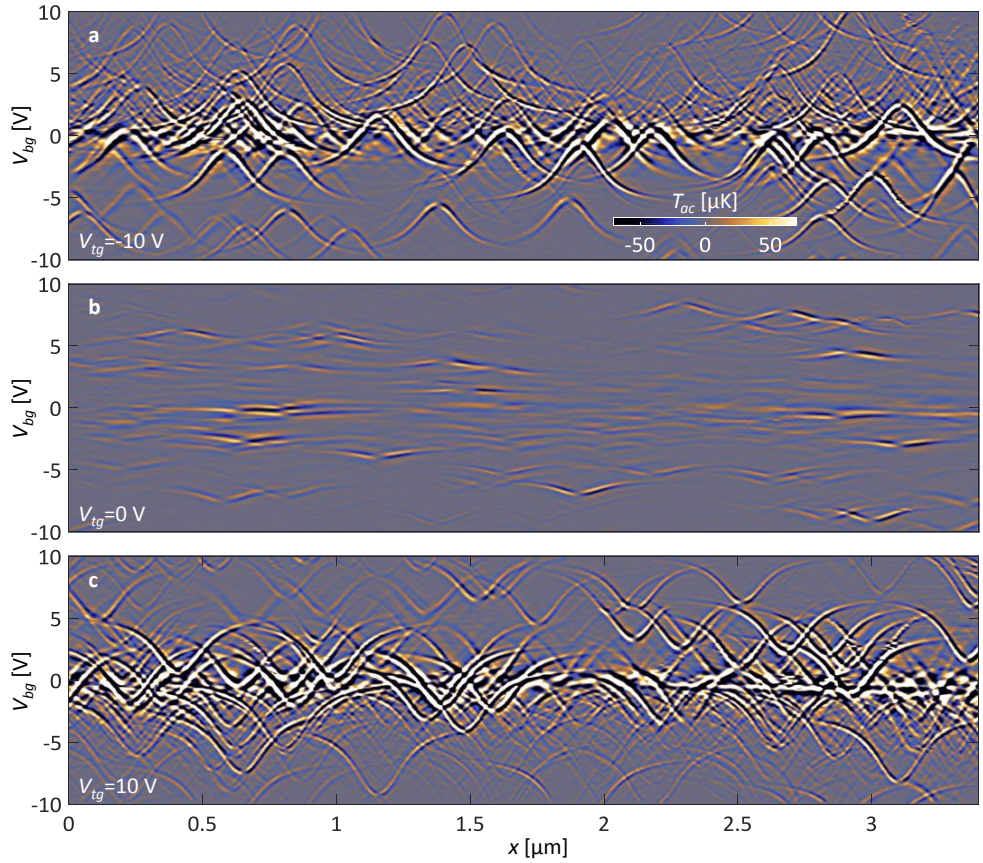

Figure 27 | Thermal spectroscopy of individual edge localized states.

Maps of $T_{ac}^{TF}(x)$ line scans along the bottom edge of the square graphene sample in Figure 19c at $V_{tg} = -10$ V (a), 0 V (b) and 10 V (c). Each bell-shaped trace originates from a single dissipative atomic defect. $I_{dc} = 3$ μA, $h = 20$ nm, and $x_{ac} =$ 2.7 nm, pixel width 4 nm, pixel height 100 mV, scan-speed 60 ms/pixel. High-pass filtering was used to enhance the features for presentation purposes.

4.4.4 Prevalence of localized states at the edges of graphene structures

The above conclusions are reinforced by examining the LS's along the edges of graphene, which display spectroscopic features very similar to those of the bulk defects, albeit with some notable differences. Figure 27 shows tSOT line scans along the bottom edge of the sample crossing through numerous LS's, while increasing V_{bg}. Each LS is visible as a bell-shaped trace similar to the ones in Figure 23d-f, indicating the same microscopic origin of different LS's. In contrast to LS's in the bulk, the edge LS's are extremely dense with some adjacent states only about 1 nm apart. This puts an additional bound on their spatial extent (Appendix 7). We ascribe their origin to the carbon dangling bonds near the edge with high affinity to adatoms and molecules, giving rise to resonance states formed by the resulting sp^3 vacancies[51–54]. Notably, the LS's display vast variations in E_{LS} values, manifested in Figure 27 by the vertical

spread of the bell-shaped traces over entire V_{bg} range of 20 V. This translates into 250 meV spread in E_{LS}, limited by our bias range. Remarkably, we resolve states that are less than 2 nm apart, but differ in their E_{LS} by as much as 160 meV (Appendix 7). Such large energy-level variation may arise from a more diverse chemical origin of the atomic defects at the chemically etched edges as compared to native bulk defects of graphene, like hydrogen bonds[52,55,57]. An alternative explanation is Coulomb interaction between the charged defects. Indeed, charging a LS by just one electron would shift the energy of a neighboring LS at a distance of 2 nm by ~240 meV which agrees with our observations (Appendix 6).

It is also interesting to note that the average intensity of the rings along the boundaries in Figure 19c appears to be uniform. This means that the electrons bounce within the sample numerous times before relaxation takes place, thus pointing to the LS's as the main dissipation pathway. Had another significant dissipation mechanism existed in the bulk, the rings' intensity should have decayed away from the carrier injecting constriction, in contrast to our observations. Disorder-assisted pathway relieving the intrinsic electron-lattice relaxation bottleneck is in agreement with theoretical predictions[49].

4.4.5 Summary

The observation of sharply localized LS's and their role in dissipation should have significant implications for thermal[22], magnetic[51,55,65], chemical[66,67] and transport[68–76] properties of graphene. The observed states are quite different from the smoother and more extended edge states anticipated for crystalline graphene edges[65]. The high density and the very large spread in the energies of the LS's imply that at any doping there are active resonant LS's near the edge that provide atomic-scale coupling between the electronic and phononic baths in graphene. This mode of dissipation is distinctly different from the conventional non-resonant picture of electron-phonon coupling[47–49], posing interesting questions for future experimental and theoretical work. Furthermore, in addition to serving as the main source for inelastic electron-phonon scattering, the LS, even when off resonance, can induce strong elastic scattering reducing the mobility of ballistic bulk carriers[58] and affecting edge transport characteristics[62,77,78]. The resonant states, localized at the edge and in the bulk, thus emerge as a dominant factor governing the dissipation and limiting carrier mobility in clean graphene.

Appendix 1: Thermodynamic limit of the thermal noise

We would like to estimate the thermodynamic limit of the thermal noise due to energy fluctuations, of a tSOT sensor as an ultimate lower bound on thermal sensitivity. We assume the sensor has a specific heat capacity (per unit mass) c_p, density ρ, heat conductivity κ and that it is in thermal equilibrium with a bath of temperature T. Following eq. 89.25 of [79] after some unit difference adaptation, and substitution of $\delta T = \frac{T}{c_p}\delta s$ we get an expression for the temperature fluctuation:

$$(\delta T^2)_{\omega,\boldsymbol{k}} = k_B \frac{2T^2}{\rho c_p} \frac{\frac{\kappa}{\rho c_p}k^2}{\omega^2 + \left(\frac{\kappa}{\rho c_p}k^2\right)^2}$$

The notation $(\cdot)_{\omega,\boldsymbol{k}}$ is defined as (eq. 122.11 of [80]):

$$\left(x_i x_j\right)_\omega \equiv \int dt \, \langle x_i(0) x_j(t)\rangle e^{i\omega t}$$

Applying for our case we get:

$$(\delta T^2)_{\omega,\boldsymbol{k}} \equiv \int dt \int d^3r \, \langle \delta T(0,0)\delta T(t,\boldsymbol{r})\rangle e^{i(\omega t - \boldsymbol{k}\cdot\boldsymbol{r})}$$

Transforming back to real space would give:

$$(\delta T^2)_\omega(\boldsymbol{r}) = \frac{1}{(2\pi)^3}\int d^3k \, (\delta T^2)_{\omega,\boldsymbol{k}} e^{i\boldsymbol{k}\cdot\boldsymbol{r}}$$

Since $r = |\boldsymbol{r}_1 - \boldsymbol{r}_2|$ is the distance between two points in space, $\boldsymbol{r}_1$ and $\boldsymbol{r}_2$, for which the correlation is calculated, we will consider the average of this expression when $\boldsymbol{r}_1$ and $\boldsymbol{r}_2$ are confined within a sphere of a typical length-scale R (we also mark $V = \frac{4\pi}{3}R^3$), and take the square root to get an estimate for the thermal noise in $\frac{K}{\sqrt{Hz}}$:

$$N_T(\omega, R) \equiv \sqrt{\frac{1}{V^2}\int_{r_1<R} d^3r_1 \int_{r_2<R} d^3r_2 (\delta T^2)_\omega(\boldsymbol{r}_1 - \boldsymbol{r}_2)} = \sqrt{\frac{1}{(2\pi)^3}\int d^3k (\delta T^2)_{\omega,\boldsymbol{k}} F_R(\boldsymbol{k}) F_R(-\boldsymbol{k})}$$

Where $F_R(\boldsymbol{k})$ is a function of $\boldsymbol{k}$, defined by:

$$F_R(\boldsymbol{k}) \equiv \frac{1}{V}\int_{r<R} d^3r e^{i\boldsymbol{k}\cdot\boldsymbol{r}}$$

After some algebra one can show that:

$$F_R(\boldsymbol{k}) = \sqrt{w(kR)}$$

Where:

$$w(u) \equiv \left(\frac{3}{u^3}(sin(u) - u\cdot cos(u))\right)^2$$

Next we substitute in the expression for $N_T(\omega, R)$:

$$N_T(\omega, R) = \sqrt{\frac{3k_B T^2}{5\pi\kappa R}\Lambda\left(\frac{\rho c_p \omega R^2}{\kappa}\right)}$$

Where $\Lambda(\alpha)$ is a unit-less function defined by:

$$\Lambda(\alpha) \equiv \frac{5}{3\pi}\int_0^\infty du \frac{u^4}{\alpha^2+u^4} w(u)$$

Note that $\Lambda(0) = 1$ and it falls monotonically to 0 as α increases. By identifying the poles of the integrand and performing contour integration, $\Lambda(\alpha)$ can be formulated explicitly as:

$$\Lambda(\alpha) = \frac{15}{2(2\alpha)^{\frac{3}{2}}}\left(1-\frac{1}{\alpha}+e^{-\sqrt{2\alpha}}\left(\left(1+\sqrt{\frac{8}{\alpha}}+\frac{1}{\alpha}\right)cos\left(\sqrt{2\alpha}\right)+\left(1-\frac{1}{\alpha}\right)sin\left(\sqrt{2\alpha}\right)\right)\right)$$

However, for all practical material values we can consider the *dc* limit and approximate:

$$N_T(\omega, R) = \sqrt{\frac{3k_B T^2}{5\pi\kappa R}}$$

This estimate is not strongly dependent on the chosen parameters. Taking $R = 100\ nm$ as the diameter of a tSOT, and the specific heat of Pb at the base temperature as 0.042 $\mathrm{cal/Kg \cdot mole}$ [42] and thermal conductance ranging from 1 to 100 $\frac{W}{m \cdot K}$ would give a thermal noise ranging from 2 to 20 $\frac{nK}{\sqrt{Hz}}$.

Appendix 2: Assessment of thermal resistances of the tSOT

Experimental assessment

Figure 1d shows a simplified low-frequency thermal model of the tSOT scanning system. Evaluation of R_{sd} and R_{ss} is thus highly desirable for proper utilization and optimization of the tSOT sensor. In the following we assess theoretically the sensor-device thermal resistance R_{sd} and then determine experimentally the corresponding sensor-support resistance R_{ss}.

Since at 4.2 K and 1 mbar pressure the mean free path of He atoms is ~3 μm we consider for our scanning heights a molecular flow regime in which He atoms flow ballistically between the sample surface and the apex of the tSOT sensor. According to Kennard's law [41], the net power flux Ω per unit temperature hitting a unit area under this regime is $\Omega = \left(\alpha\frac{\gamma+1}{\gamma-1}\sqrt{\frac{R}{8\pi MT}}\right)p \equiv \beta p$. Here α is the accommodation coefficient (here taken as unity), γ is the adiabatic constant, R is the universal gas constant, M is the molar mass, p the gas pressure, and $T = 4.2$ K the surface temperature (assumed to be much larger than the induced *ac* temperature variations) resulting in $\beta = 18$ m/s/K. R_{sd} is then given by $R_{sd} = 1/(\beta S p)$, where $S = \pi D^2/4$ is the surface area of a tSOT of diameter D. Figure A1 shows the resulting $R_{sd}(p)$ calculated for $D = 240$ nm tSOT vs. the He pressure p. R_{sd} can be readily varied from about 1.6×10^{10} K/W at 1 mbar to 5×10^{8} K/W at 30 mbar.

Solving the effective circuit of Figure 1d, the relation between the *ac* temperatures T_{ac}^{s} of the tSOT and T_{ac}^{d} of the device is given by $T_{ac}^{s}/T_{ac}^{d} = [1 + R_{sd}/R_{ss}]^{-1} = [1 + (R_{ss}\beta S p)^{-1}]^{-1}$. A tSOT sensor of 240 nm diameter was held at a height of 100 nm above the surface of a metallic thin film heater of 170 Ω resistance driven by an *ac* current of 10 μA at 3.7 kHz and the T_{ac}^{s} was measured as a function of the He pressure p as shown in Figure A1 (blue circles). The dashed line shows an excellent fit to the data using the above equation with resulting $T_{ac}^{d} = 10.4$ mK and $R_{ss} = 0.9\times10^{10}$ K/W. Such remarkably high thermal resistance between the sensor and the supporting quartz pipette, even for the extreme case of a large tSOT (relative to other tSOT devices used throughout the presented work), cannot be explained by naively taking into account the bulk thermal conductivity of quartz. The nanoscale cross

section of the pipette, however, quenches the radial phonon degrees of freedom resulting in quantum-limited thermal conductance[34,81,82] (see theoretical estimate below that further supports this claim). A 1D channel with a single phonon mode has a quantum thermal resistance of $R_0 = 3h/(\pi^2 k^2 T) = 2.52\times10^{11}$ K/W at 4.2 K. The derived R_{ss} thus implies about 28 quantum channels of thermal conductance in our 240 nm diameter tSOT. The 46 nm tSOT in used in Part I may thus support only one or two channels resulting in R_{ss} in excess of 10^{11} K/W.

An additional insight can be drawn from the presented pressure dependence of the thermal signal regarding the governing heat transfer processes. Since the signal vanishes in the low pressure limit, the possible contribution of near-field radiative processes to the heat transfer between the sample and the tSOT is apparently negligible under the presented working conditions.

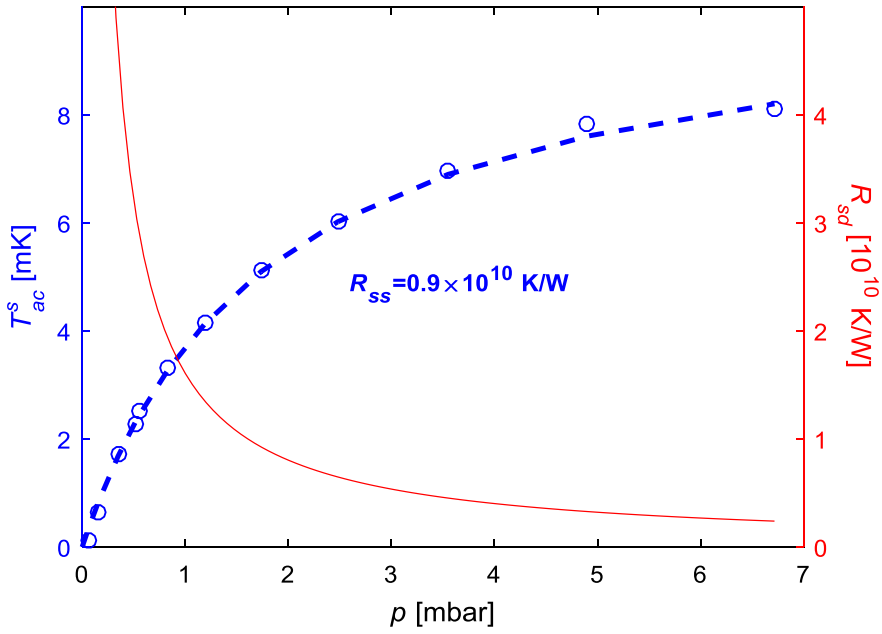

Figure A1 | Thermal resistances of tSOT.

Red: Calculated thermal resistance R_{sd} between the sensor and the sample device for 240 nm tSOT vs. the He pressure p in the molecular flow regime. Blue circles: measured tSOT *ac* temperature T^s_{ac} at height of 100 nm above a thin film heater vs. He pressure. Dashed blue line is a theoretical fit resulting in thermal resistance between the tSOT sensor and its quartz support structure of $R_{ss} = 0.9\times10^{10}$ K/W.

Theoretical estimate

As shown in section 3.2.4 and supported by the experimental assessment of the thermal resistance of the tSOT sensor in the previous section, at scanning conditions the tSOT signal follows the temperature fluctuation of the sample surface, up to a discrepancy of roughly 30%, that could be attributed to a temperature discontinuity due to Kapitza resistance in the gas-solid interface. The sensor would not have reached this performance if the heat flow between the sample surface and the sensor was not the dominant mechanism, i.e. $R_{ss} \gg R_{sd}$. An attempt to give a theoretical justification to the remarkably high thermal resistance of the device using bulk values for conductivities of the materials of the sensor would give a thermal resistance of order $10^6 \frac{K}{W}$. Taking into account a geometrical correction to the conductivities, due to typical length-scales being smaller than the phonon mean free path, following [83], would give a better estimate of order $10^9 \frac{K}{W}$, still missing the estimated value by 2 orders of magnitude. However, the sharp hollow elongated geometry of the sensor may effectively quench the radial degrees of freedom. We assume a thin cylindrical shell of radius r. Heat can flow in z, but is discretized in the tangential direction such that the acoustic modes follow the following dispersion relation: $\omega(k) = c_s k$ where $k = \sqrt{{k_z}^2 + {k_{\varphi,n}}^2}$ and we assume $k_{\varphi,n} = n/r$. c_s is the speed of sound in the material, and we define $\omega_0 = c_s/r$. The energy flux between a temperature T and T' would be $W(T,T') = W(T) - W(T')$, where:

$$W(T) = \int_0^\infty \frac{dk_z}{2\pi} \sum_{n=0}^{\infty} \frac{c_s k_z}{k} \hbar\omega(k) f_{BE}(T, \hbar\omega(k))$$

Where $f_{BE}(T,\varepsilon)$ is the Bose-Einstein distribution at temperature T with energy ε. After some algebra we get (using $d\omega = \frac{c_s k_z}{k} dk_z$):

$$W(T) = \sum_{n=0}^{\infty} \int_{n\omega_0}^{\infty} \frac{d\omega}{2\pi} \hbar\omega \frac{1}{e^{\frac{\hbar\omega}{k_B T}} - 1} = \frac{(k_B T)^2}{h} \sum_{n=0}^{\infty} \int_{n\frac{\hbar\omega_0}{k_B T}}^{\infty} dx x \frac{1}{e^x - 1}$$

After some algebra one can show that:

$$\sum_{n=0}^{\infty} \int_{nx_0}^{\infty} dx x \frac{1}{e^x - 1} = \sum_{n=1}^{\infty} \frac{1}{n^2} f(nx_0)$$

Where:

$$f(x) = \frac{1 + (x-1)e^{-x}}{(1 - e^{-x})^2}$$

$$W(T) = \frac{(k_B T)^2}{h} \sum_{n=1}^{\infty} \frac{1}{n^2} f\left(n \frac{\hbar \omega_0}{k_B T}\right)$$

Where k_B is Boltzmann's constant. In the low temperature limit this expression converges to the 1D limit presented in [34] which scales as T^2 and as T^3 for the high temperature limit. Taking typical tSOT parameters of *r*=50 nm and $c_s = 2 \cdot 10^3 \ m/s$ this derivation yields a thermal resistance of $0.8 \cdot 10^{10} \ K/W$ at liquid helium temperature. Still an order of magnitude short from the measured value. It is possible that an additional mechanism suppresses the thermal conduction through the tSOT device even further.

Appendix 3: Carbon nanotube fabrication

The SWCNT devices were fabricated on p-doped Si (100) with a thermally grown oxide layer of 300 nm, as reported in Ref. [43]. Briefly, parallel stripes (25 μm wide, 25 nm thick) of amorphous SiO_2 coated by a thin layer (nominally 0.3 nm) of Fe growth catalyst were deposited on the substrate by standard photolithography and electron-beam evaporation. The samples were introduced into a tube furnace and were heated to 550° C for 20 min in air to remove organic contaminations. The SWCNT were grown by CVD: samples were heated to 900° C in an atmosphere of 300 sccm Ar and 200 sccm H_2, followed by introduction of 1 sccm C_2H_4. Growth time was 45 min, by the end of which samples were left to cool in Ar. Electrodes for transport measurements were subsequently patterned by electron beam lithography, followed by deposition of 20 nm of Pd for Ohmic contacts and 10 nm of Au.

Figure A2 presents the electrical characterization of the two SWCNT devices discussed in section 3.3 as a function of the applied back gate voltage V_g. Both devices are highly disordered, forming a series of quantum dots, resulting in very low conductance and large fluctuations of the conductance vs. V_g. Device 1 (Figure A2 and Figure 14a) shows a metallic behavior with finite conductance at all values of V_g, while device 2 (Figure A2b and Figure 14b) shows a semiconducting behavior.

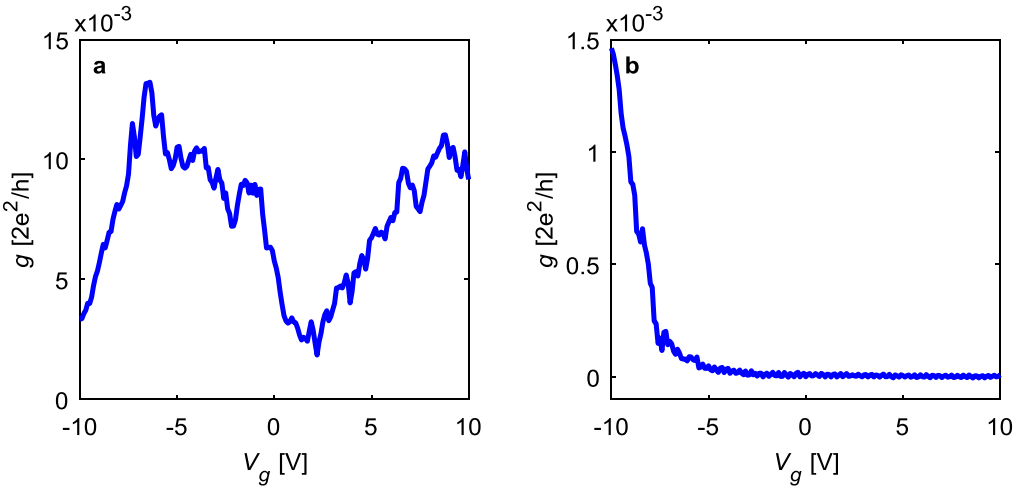

Figure A2 | Gate dependence of SWCNT conductance at 4.2 K.

a, Device 1 measured with applied ac voltage of 80 mV at 31.5 Hz showing a highly disordered metallic behavior. **b**, Device 2 measured with *ac* voltage of 110 mV at 28.9 Hz showing a semiconducting behavior.

Appendix 4: Ring-like patterns in scanning gate thermometry due to localized states

In order to provide qualitative description of the characteristic ring-like patterns in scanning gate thermometry as seen in thermal imaging of CNT and graphene devices throughout the work, we performed 3D heat diffusion simulations using COMSOL. The CNT was modeled as a nanowire in a substrate with looped form matching the actual shape in Figure 14d. Due to numerical limitations the CNT was modeled with a cross section of 50×50 nm^2 and the heat conductivity of the CNT (1100 $W \cdot m^{-1}K^{-1}$ for 5 nm diameter CNT [84]) was rescaled accordingly to give an equivalent heat flow along the CNT. Similarly, the graphene was modelled as 50 nm thick with rescaled heat conductivity equivalent to 2000 $W \cdot m^{-1}K^{-1}$ for thickness of 0.3 nm [84] with geometry as in Fig. 3a. The heat conductivity of semi-infinite SiO_2 substrate was taken as 0.08 $W \cdot m^{-1}K^{-1}$ [85]. The qualitative features presented below are insensitive to the values of thermal conductivities, which mainly determine the overall temperature scale.

Figure A3a shows the surface temperature distribution due to dissipation per unit length in the CNT of 20 pW/μm showing the enhanced temperature along the CNT and the heat diffusion in the substrate on a typical length scale of 1 μm, similar to the experimental data in Figure 14a (in the simulation straight segments of dissipating CNT extend 7 μm on each side beyond the displayed area). Figure A3b shows the surface temperature distribution caused by a localized resonant QD state on the CNT (located as marked by the right blue dot in Figure A3a), modeled as a region with 20 nm diameter dissipating 20 pW giving rise to a heat spot diffusing into the substrate. The visible anisotropic shape of the surface temperature is due to higher heat conductivity along the CNT. In the case of reduced heat conductivity along the CNT the heat spot will be isotropic with universal $1/r$ decaying temperature profile determined by heat diffusion in an isotropic substrate. Temperature distribution due to another independent QD is shown in Figure A3c.

When the QDs are not in resonance the thermal image acquired by the scanning tSOT will be described by Figure A3a. On the other hand, if one of the QDs is at resonance the excess dissipation will result in a thermal image that is given by the sum of Figure A3a and Figure A3b or of Figure A3a and Figure A3c accordingly.

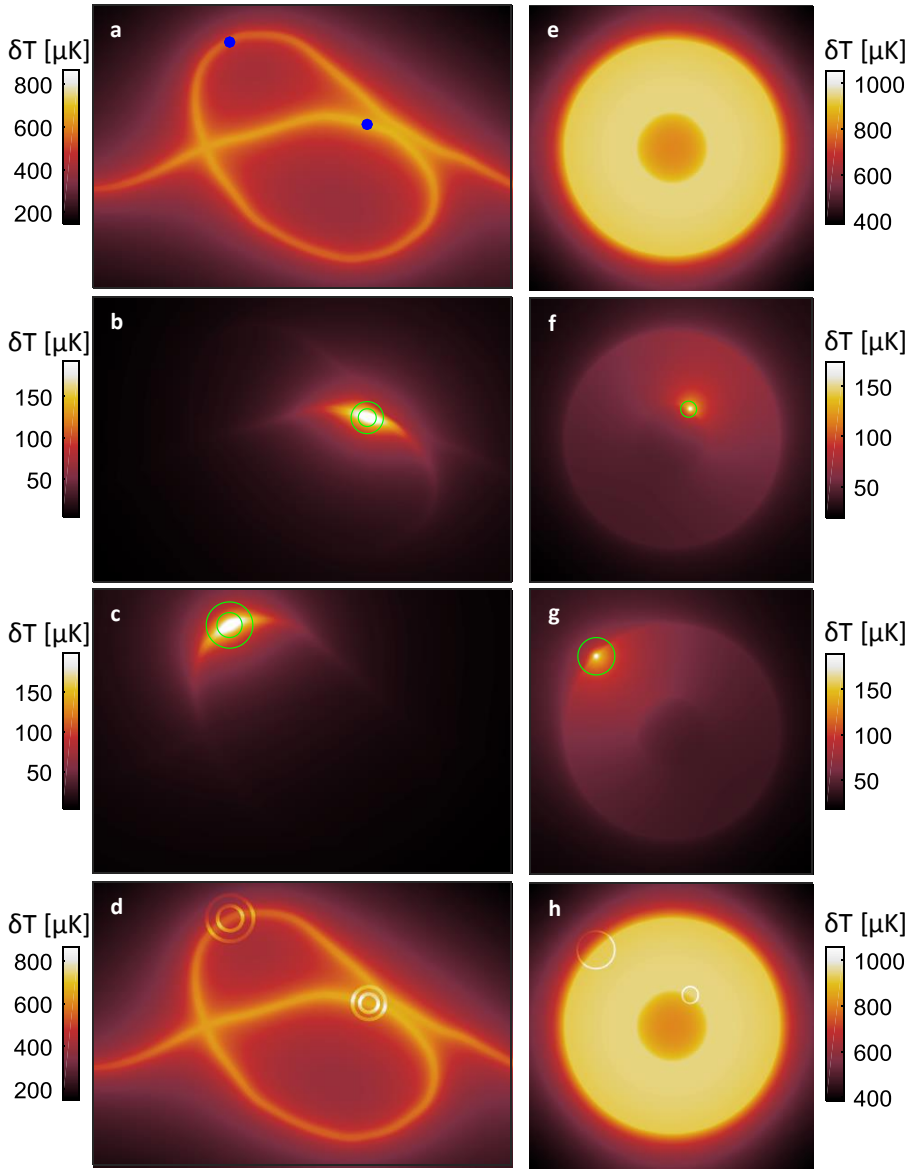

Figure A3 | Numerical simulations of thermal ring-like structures due to resonant states in CNT and graphene.

a, Surface temperature distribution $\delta T(x,y)$ due to 20 pW/μm power dissipation in a looped CNT on a SiO_2 substrate. **b,** $\delta T(x,y)$ due to 20 pW dissipation at a point on the CNT marked in blue in (a). **c,** Similar $\delta T(x,y)$ due to the left point heat source marked in (a). **d,** Surface temperature distribution resulting from adding $\delta T(x,y)$ values along the green rings in (b) and (c) to $\delta T(x,y)$ of (a). **e,** Surface temperature $\delta T(x,y)$ due to 40 pW/μm^2 power dissipation in a washer shaped graphene structure on a SiO_2 substrate. **f,** $\delta T(x,y)$ due to 60 pW dissipation at a point in the graphene marked in blue in (e). **g,** Similar $\delta T(x,y)$ due to the heat source at left point marked in (e). **h,** Surface temperature attained by adding $\delta T(x,y)$ values along the green rings in (f) and (g) to $\delta T(x,y)$ of (e).

However, the excess dissipation is present only when the QD is tuned into its *n*-th Coulomb blockade resonance by the tip potential. This occurs when the tSOT is at some lateral distances R_n from the QD (which depends among other things on the scanning height and the tip potential V_{tSOT}). As a result, the excess dissipation in the QD is present only when the tSOT is located along concentric rings of radius R_n shown by the green circles in Figure A3b,c (only a pair of R_n rings is shown for each QD for clarity). Each QD will have a different set of R_n depending on the local potential structure, doping, and the QD capacitance as observed by scanning gate AFM[44,69,86–88]. The width of the rings is determined by the broadening of the Coulomb blockade energy levels of the QD and was taken to be 50 nm in the simulations.

The thermal image attained by the scanning tSOT will therefore be composed as following. At any location except at the rings, the image will be given by Figure A3a. When the tip is on one of the rings of the right QD, however, the QD dissipates and hence the image will be given by the sum of Figure A3a and Figure A3b. Similarly, when the tSOT is scanned across the left QD, the measured temperature along the green circles will be given by addition of Figure A3a and Figure A3c. The resulting combined thermal image is presented in Figure A3d providing a qualitative description of the experimental results in Figure 14 and Figure 15. The same process is presented in Figure A3e-h for the case of washer shaped graphene structure on a SiO_2 substrate (inner/outer diameters of 2 and 6 μm respectively), where a heat of 40 pW/μm^2 was dissipated uniformly in the graphene. The resulting surface temperature of the sample is presented in Figure A3e showing a uniform temperature in the graphene and a decaying distribution outside the washer and in the central aperture due to heat diffusing in the substrate, similar to the experimental data in Figure 19c. Figure A3f and Figure A3g present the thermal map due to 60 pW dissipation over dots with a diameter of 20 nm, representing localized resonant states, positioned at locations indicated by blue dots in Figure A3e. Similarly to the case of CNT the excess dissipation at the localized states occurs only when the scanning tip is located at lateral distance R marked by the green circles in Figure A3f-g. The resulting thermal image attained by a scanning tSOT will therefore appear as shown in Figure A3h.

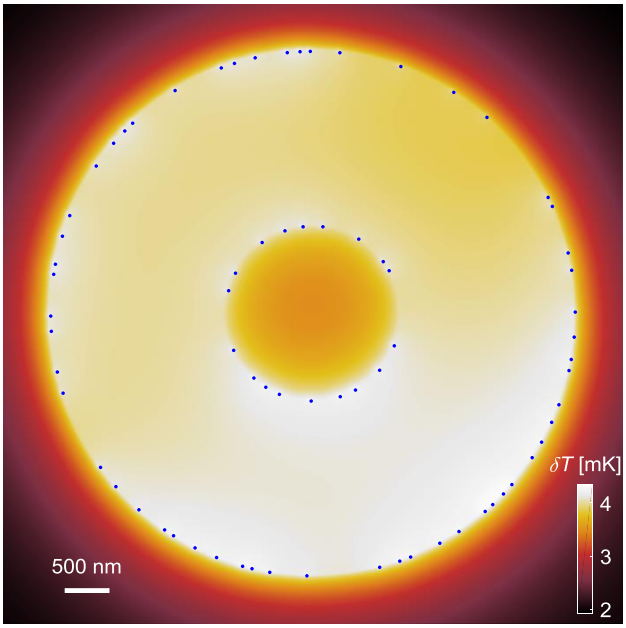

Figure A4 | Numerical simulation of an ensemble of point heat sources in graphene.

Simulation of the surface temperature $\delta T(x,y)$ due to random distribution of point heat sources along the washer-shaped graphene edges on SiO_2 substrate. The locations of the sources are marked by blue dots with an average density of 3 points/μm, which is sparser compared to the experimental findings. A power of 60 pW is dissipated at each point, resulting in a smeared image in which the ability to resolve the individual heat sources is lost, in contrast to Figure 19c.

Even though the ring structures may seem like a measurement artifact, they in fact provide a powerful spectroscopic tool that allows detection of the QDs or other resonant dissipative states which would not be possible otherwise. Figure A4 shows the calculated surface temperature distribution of the graphene washer similar to Figure A3e in which instead of a uniform bulk heating all the dissipation arises due to isolated point heat sources, like in Figure A3f,g, randomly distributed along the edges with even sparser average density (3 sources/μm) as compared to the experimental findings of Figure 19c. The resulting $\delta T(x,y)$ shows smooth inhomogeneities due to variations in the local average density of the point sources, smeared by the long-range heat conductivity, with essentially no visible signature of the individual sources. The scanning gate ability of the tSOT, in contrast, allows controllable switching of each of the point sources thus providing a unique tool for their individual detection and characterization.

Appendix 5: Simulations of the electrostatic interaction between the tSOT and the sample

The powerful spectroscopic capabilities of the tSOT nanothermometry arise from the local electrostatic interaction between the tip and sample. In this section we derive this interaction and provide some simulations by numerical solution of Laplace's equation for the potential $\varphi(r,z)$ in an axial-symmetric geometry.

Our simulated space consisted of graphene residing in $z=0$ plane while the tSOT was modeled for simplicity as a disc with outer diameter d_0 and thickness t located at a height z_{tip} above the graphene. A fixed voltage boundary condition of V_{tg} was applied to the disc and a fixed voltage boundary condition of V_{bg} was applied at $z=-d_{bg}$ to account for the back gate. The entire space above and below the graphene was taken to be homogeneous with dielectric constant ϵ to simplify the numerics. Zero Neumann boundary conditions were used at large r and z. The surface charge density $\sigma(r)$ in the graphene at $z=0$ was solved self-consistently as follows. The tip potential induces a local band bending $E_D(r)$ of the graphene Dirac energy and changes the local chemical potential $\mu(r)=E_F-E_D(r)$, while the electro-chemical potential E_F remains constant throughout the graphene and fixed to $E_F=0$. Unlike in an ideal metal, a finite in-plane field can be present in graphene. Equilibrium conditions require that a test charge experiences a zero net in-plane force. This dictates that the in-plane field is balanced by the gradient of the chemical potential, which results in a boundary condition $E_D(r)=-e\varphi(r,z=0)+E_{D,\infty}$, where $E_{D,\infty}$ is the global band bending due to the back-gate voltage V_{bg}. Considering the Dirac density of states $D(\varepsilon)=\partial n/\partial\varepsilon=2\varepsilon\left(\sqrt{\pi}\hbar v_F\right)^{-2}$ (where $\varepsilon=|E_F-E_D|$), which results in: $|\varepsilon(n)|=\sqrt{\pi}\hbar v_F\sqrt{n}$. In terms of charge density, σ, this would be: $\varepsilon(\sigma)=-sign(\sigma)\sqrt{\frac{\pi}{e}}\hbar v_F\sqrt{|\sigma|}$. Using the geometrical capacitance between the two parallel plates (graphene and back gate) we can write an equation for the energy to take a charge the graphene from moving charges from the back-gate to a charge density σ_∞, $eV_{bg}=\varepsilon(\sigma_\infty)-\frac{e\cdot d_{bg}}{\epsilon\epsilon_0}\sigma_\infty$. From this and using, $sign(\sigma_\infty)=-sign\left(V_{bg}\right)$, it is straightforward to derive at an analytic expression for $n_\infty=\frac{1}{e}|\sigma_\infty|$:

$$n_\infty = \left(\sqrt{\left(\frac{\epsilon\epsilon_0 \sqrt{\pi}\hbar v_F}{2e^2 d_{bg}} \right)^2 + \frac{\epsilon\epsilon_0}{e \cdot d_{bg}} |V_{bg}|} - \frac{\epsilon\epsilon_0 \sqrt{\pi}\hbar v_F}{2e^2 d_{bg}} \right)^2$$

From which, we get: $E_{D,\infty} = -\varepsilon(\sigma_\infty) = -sign(V_{bg})\sqrt{\pi}\hbar v_F \sqrt{n_\infty}$.

On the other hand, $\sigma(r)$ is determined by $E_D(r)$ through $D(\varepsilon)$, resulting in $\sigma(r)$ that is given by the relation $E_D(r) - E_F = \text{sign}(\sigma(r))\sqrt{\pi/e}\hbar v_F \sqrt{|\sigma(r)|}$, resulting in a closed set of equations that can be self-consistently solved.

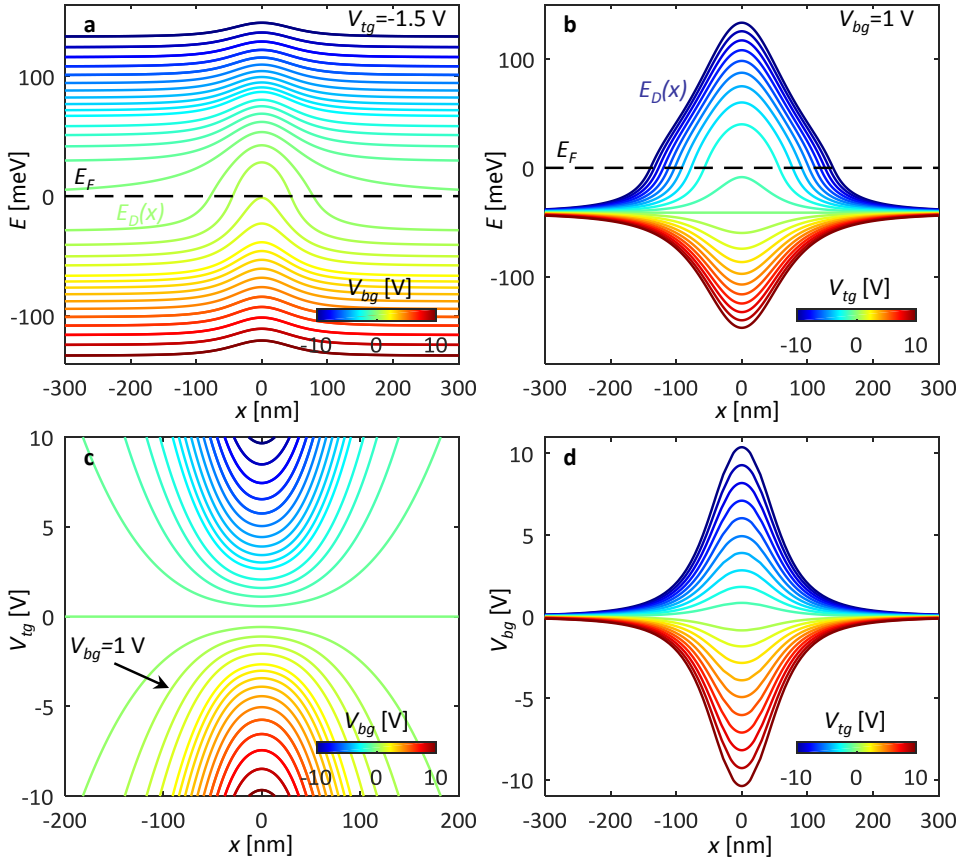

Figure A5 | Numerical simulations of tip-induced potentials and spectroscopy.

a, Band bending $E_D(x)$ induced in graphene by the tSOT located at $x = 0$ at potential V_{tg} = -1.5 V for various back gate voltages V_{bg}. **b**, Band bending $E_D(x)$ in graphene at V_{bg} = 1 V and different values of V_{tg}. **c**, Resonant dissipation traces describing the lateral displacement x of the tSOT from the defect at which resonant conditions for inelastic scattering are met as a function of V_{tg} for various values of V_{bg} depicting the experimental results in Figure A6b. **d**, Resonant dissipation bell-shaped traces as a function of V_{bg} for various values of V_{tg} describing the experimental results in Figure A6e.

In the simulation results of Figure A5 the following parameter values were used: outer tip diameter $d_0 = 50$ nm, tip thickness $t = 5$ nm, $\epsilon = 3, v_F = 10^6$ m/s, d_{bg} was set to 125 nm to match the experimentally derived C_{bg} (see section 4.2.1), and z_{tip} was set to 57 nm to attain comparable C_{tg} and C_{bg} capacitances as in the experiment. The graphene band bending $E_D(x)$ is shown in Figure A5a for tip potential $V_{tg} = -1.5$ V for various back gate voltages V_{bg}. The $E_D(x)$ curve in Figure 22 was derived for $V_{tg} = -3$ V and $V_{bg} = 0.25$ V. The strongest tip-induced band bending occurs when $E_D(x)$ crosses zero where the graphene is incompressible. At high values of V_{bg} the bending is reduced due to a more effective screening. Figure A5b shows similar results for a constant $V_{bg} = 1$ V and different values of V_{tg}. From these results we can calculate the evolution of the radius R of the dissipation ring assuming that the LS is pinned to the Dirac point, $E_{LS} = E_D(x)$, where x is the tip distance to the defect, and the carriers are injected close to the Fermi energy $E_e \cong E_F = 0$. Figure A5c shows the resonant dissipation traces as a function of V_{tg} for various values of V_{bg} which are akin to the experimental results in Figure A6a-c. The points along the traces indicate the lateral displacement x of the tSOT from the defect at which resonant conditions for inelastic scattering are met for various values of V_{tg} and V_{bg}. For example, for $V_{bg} = 1$ V, as described in Figure A5b, the resonant conditions occur only for negative $V_{tg} < -1$ V for which $E_D(x)$ crosses $E_F = 0$. The distance $2R$ between the crossing points grows with decreasing V_{tg} resulting in the resonance trace marked by an arrow in Figure A5c. Figure A5d presents the resonant bell-shaped traces as a function of V_{bg} for various values of V_{tg} describing the experimental results in Figure A5a-c.

Appendix 6: Search for additional energy levels of a localized state

In this appendix we explore the widest energy range for searching for additional possible energy levels of the LS. By repeatedly scanning the tSOT along the line crossing defect 'C' and incrementing V_{bg} we derive the resonant traces describing the evolution of the radius of the dissipation ring $R(V_{tg})$ as shown in Figure A6a-c (in a similar manner to Figure 23d-f). These traces correspond to the numerical results presented in Figure A5d. The traces are bell-shaped, in which R diverges when $V_{bg} = V_{bg}^{LS}$ as expected (Figure A5d). Figure A6a,c shows the bell-shaped resonance traces at $V_{tg} = 10$ V and $V_{tg} = -10$ V over the entire range of $V_{bg} = \pm 10$ V. Traces at various intermediate values of V_{tg} are presented in Figure A6b. These data are summarized in Figure A6d showing the ring radius R in the V_{bg}-V_{tg} plane. In the white areas no dissipation is present since E_{LS} is far from resonance. In the colored regions inelastic scattering occurs depending on the tip position. The transition line (dark blue) maps the resonant conditions when the tip is positioned directly above the defect ($R = 0$) as in Figure 21d, while the red color reflects the conditions for diverging R. The black dot describes the bare resonance point V_{bg}^{LS}, V_{tg}^{FB} at which V_{tg} corresponds to flat-band conditions of the tip and V_{bg} aligns E_{LS} with $E_e \cong E_F$ in absence of tip potential. This is the point at which the resonant traces switch their polarity and V_{bg}^{LS} describes the position of the LS energy level E_{LS}.

The slope of the $R = 0$ resonance line in Figure A6d (dark blue) describes the ratio between the back gate and the tip capacitances C_{bg}/C_{tg} that is affected by the tip height h as described in Appendix 5. With $C_{bg} = 1.25 \cdot 10^{11}$ 1/cm^{2}V attained from the magneto-transport data of section 4.2.1, we derive $C_{tg} = 1.3 \cdot 10^{11}$ 1/cm^{2}V at $h =$ 12 nm.

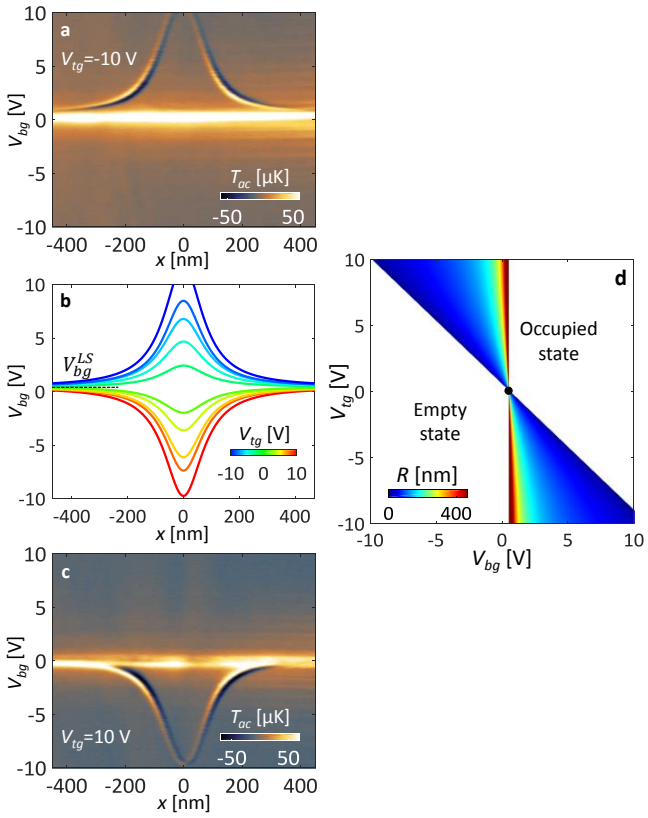

Figure A6 | Search for additional energy levels of a localized state.

a, Map of $T_{ac}(x)$ line scans through the center of defect 'C' showing the bell-shaped resonance trace at $V_{tg} = -10$ V over the full range of $V_{bg} = \pm 10$ V at $h = 12$ nm, $x_{ac} = 2.7$ nm, and $I_{dc} = 6$ μA. The bright strip at $V_{bg} \approx 0$ V arises from enhanced heating at the nearby constriction, the resistance of which becomes very large close to CNP. **b**, The resulting fitted bell-shaped resonance traces $R(V_{bg})$ for various values of V_{tg} that change their polarity at V_{bg}^{LS}, V_{tg}^{FB}. **c**, Same as (d) at V_{tg} =10 V. The fact that only a single resonance trace is observed in (a) and (c) shows that the LS has only one energy level in the accessible range of V_{tg} and V_{bg}. **d**, The dissipation ring radius $R(V_{bg}, V_{tg})$ of the LS over the entire range of tip and back gate voltages with the V_{bg}^{LS}, V_{tg}^{FB} point marked by black dot.

The fact that only a single resonance trace is visible in Figure A6d,f shows that the LS has just one energy level in this range of $\pm V_{tg}^{max}$ and $\pm V_{bg}^{max}$. This translates into a range of carrier concentrations of $\pm(C_{tg}V_{tg}^{max} + C_{bg}V_{bg}^{max}) = \pm 2.6 \cdot 10^{12}$ cm^{-2} and corresponding energy span of ± 186 meV. These results show that the LS has just a single energy level E_{LS} near the Dirac point with no additional levels in the range of at least ΔE = ± 186 meV from E_D. From this lower bound on the level spacing and taking into account the charging energy we can derive the maximal effective size of the LS as $d_{LS} = (4\pi\varepsilon_{hBN}\varepsilon_0)^{-1} e^2/\Delta E = 2.4$ nm, where $\varepsilon_{hBN} \cong 3$ is the dielectric constant of hBN.

Appendix 7: Analysis of localized states along the graphene edges

The numerous LS along the graphene edges were analyzed as described in Figure A7. The tSOT was scanned along the bottom edge of the graphene sample and the bell-shaped resonance traces were acquired by sweeping the back gate V_{bg} at different V_{tg} (see Figure 27). Figure A7a shows the data at $V_{tg} = -10$ V reproduced here from Figure 27a for clarity. Figure A7b presents the same data with overlaid fits to the traces (black) of empirical form $V_{bg}(x) = V_{bg}^{LS} - V_{bg}^{CNP} + V_p/(1 + (x - x_i)^2/w^2)$ with four fitting parameters: $V_{bg}^{LS} - V_{bg}^{CNP}$ is the V_{bg} value corresponding to the energy E_{LS} of the LS, V_p describes the height of the bell shape determined by V_{tg}, w is the width of the bell shape governed by the scanning height h of the tSOT, and x_i is the location of the LS along the edge.

Our numerical algorithm detected $m = 135$ traces along $L = 3.5$ μm long graphene edge which reflects only a fraction of the total number of LS's. The average density of the identified LS's is $\rho = m/L = 38.6$ μm^{-1}. Analysis of the distances Δx_{nn} between the nearest neighbors (Figure A7c) reveals that the probability density of Δx_{nn} is described by Poisson distribution $P(\Delta x_{nn}) = \rho e^{-\Delta x_{nn}\rho}$ (black curve) indicating that LS's are distributed randomly, excluding presence of clustering or long-range spatial correlations.

Figure A7d presents the V_{bg}^{LS} values of the different LS's that shows a very wide distribution with no apparent correlations. Such a large random variability over very short length-scales is inconsistent with the possibility that the variations in V_{bg}^{LS} result from formation of "puddles" due to long-range substrate potential disorder[64] and support the Coulomb repulsion scenario. Moreover, the V_{bg}^{LS} values appear to be uniformly distributed, without visible clustering around specific values that may characterize particular adatom defects. Chemical variability of adatoms is therefore not a likely explanation of the large variability of the energy of the LS's. The difference in V_{bg}^{LS} between the nearest neighbors $\Delta_{nn} V_{bg}^{LS}$ (Figure A7e) reaches ± 15 V, limited by our accessible V_{bg} span, and seems to be independent of the distance Δx_{nn} between the neighbors from sub nm to 100 nm distances. Note, however, that we analyze only a fraction of the defects. Remarkably, we detect neighboring defects that

are separated on nm scale while showing variation of up to 10 V in their V_{bg}^{LS} energy. Examples of such pairs of nearest neighbors are marked in color in Figure A7b. The green traces show an example of five LS's within a segment of 8 nm along the graphene edge with significantly different energies.

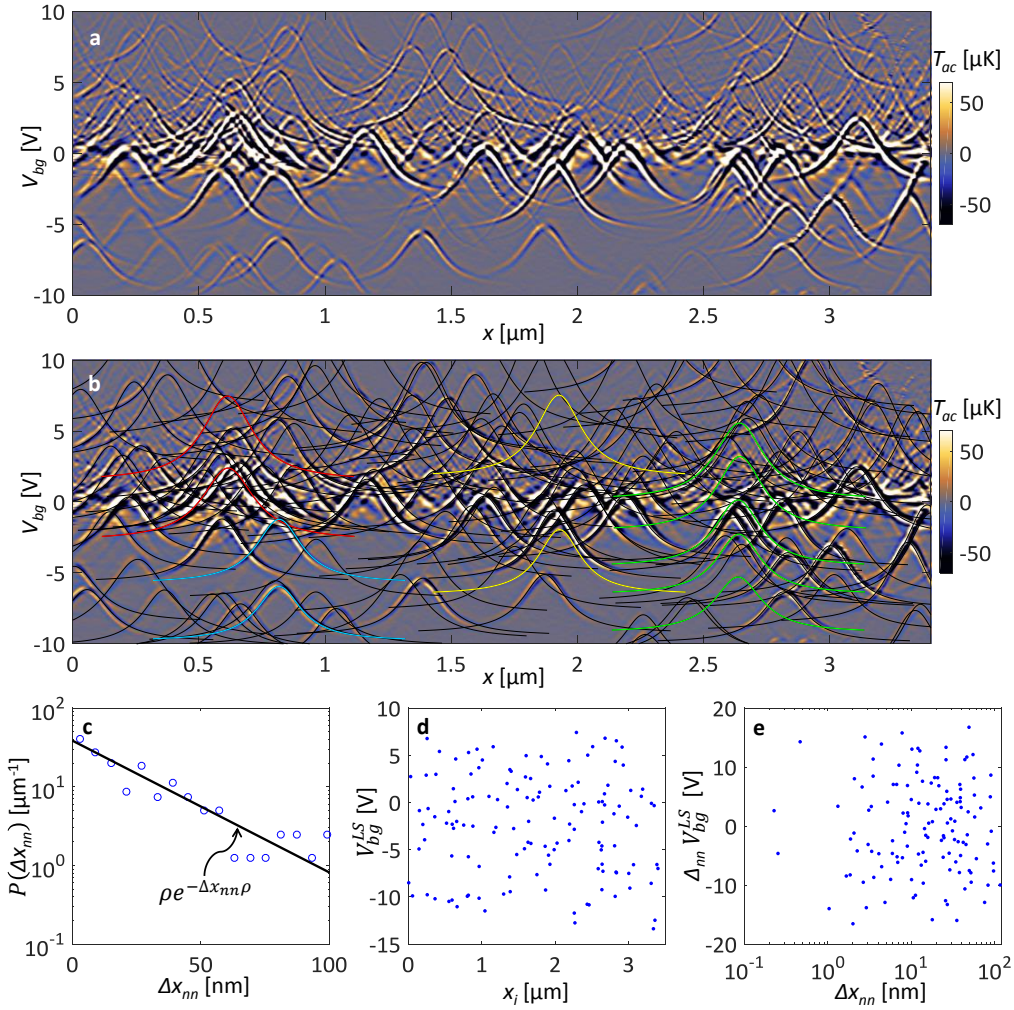

Figure A7 | Spectroscopic thermal imaging of the localized edge states.

a, Map of $T_{ac}(x)$ line scans along the bottom edge of the graphene sample (reproduced from Figure 27a) vs. V_{bg} at $V_{tg} = -10$ V showing bell-shaped resonant dissipation traces of the individual LS's. **b**, Numerical fits (black) to the bell-shaped traces of 135 clearly resolved LS's. The asymptotic values of the traces V_{bg}^{LS} describe the energy E_{LS} of the LS's. The colored traces (red, blue and yellow) show examples of pairs of adjacent neighbors with significantly different energy V_{bg}^{LS}. The green traces show an example of five LS's within 8 nm interval. **c**, Probability density of the nearest neighbor distances Δx_{nn} between the LS's (20 bins) and the theoretical exponential decay for random distribution (black). **d**, V_{bg}^{LS} values of the resolved states vs. their location x_i along the edge showing large uncorrelated variation in the energy of the LS's. **e**, The difference in V_{bg}^{LS} between the nearest neighbors $\Delta_{nn} V_{bg}^{LS}$ vs. the distance Δx_{nn} between the neighboring LS's.

5 Bibliography

1. Yue, Y. & Wang, X. Nanoscale thermal probing. *Nano Rev.* **3,** 11586 (2012).
2. Giazotto, F., Heikkilä, T. T., Luukanen, A., Savin, A. M. & Pekola, J. P. Opportunities for mesoscopics in thermometry and refrigeration : Physics and applications. *Reviews* **78,** 217–274 (2006).
3. Jin, C. Y., Li, Z., Williams, R. S., Lee, K. & Park, I. Localized temperature and chemical reaction control in nanoscale. *Nano Lett.* **11,** 4818–4825 (2011).
4. Kucsko, G. *et al.* Nanometre-scale thermometry in a living cell. *Nature* **500,** 54–8 (2013).
5. Mecklenburg, M. *et al.* Nanoscale temperature mapping in operating microelectronic devices. *Science* **347,** 629–632 (2015).
6. Teyssieux, D., Thiery, L. & Cretin, B. Near-infrared thermography using a charge-coupled device camera: Application to microsystems. *Rev. Sci. Instrum.* **78,** 34902 (2007).
7. Toyli, D. M., de Las Casas, C. F., Christle, D. J., Dobrovitski, V. V & Awschalom, D. D. Fluorescence thermometry enhanced by the quantum coherence of single spins in diamond. *Proc. Natl. Acad. Sci. U. S. A.* **110,** 8417–8421 (2013).
8. Neumann, P. *et al.* High-precision nanoscale temperature sensing using single defects in diamond. *Nano Lett.* **13,** 2738–2742 (2013).
9. Reparaz, J. S. *et al.* A novel contactless technique for thermal field mapping and thermal conductivity determination : Two-Laser Raman Thermometry. *Rev. Sci. Instrum.* **85,** 34901 (2014).
10. Brites, C. D. S. *et al.* Thermometry at the nanoscale. *Nanoscale* **4,** 4799–4829 (2012).
11. Majumdar, A. Scanning thermal microscopy. *Annu. Rev. Mater. Sci.* **29,** 505–585 (1999).
12. Menges, F. *et al.* Temperature mapping of operating nanoscale devices by scanning probe thermometry. *Nat. Commun.* **7,** 10874 (2016).
13. Kim, K., Jeong, W., Lee, W. & Reddy, P. Ultra-high vacuum scanning thermal microscopy for nanometer resolution quantitative thermometry. *ACS Nano* **6,** 4248–4257 (2012).
14. Sadat, S., Tan, A., Chua, Y. J. & Reddy, P. Nanoscale thermometry using point contact thermocouples. *Nano Lett.* **10,** 2613–2617 (2010).

15. Grosse, K. L., Bae, M., Lian, F., Pop, E. & King, W. P. Nanoscale Joule heating , Peltier cooling and current crowding at graphene – metal contacts. *Nat. Nanotechnol.* **6,** 287–290 (2011).
16. Pekola, J. P. Towards quantum thermodynamics in electronic circuits. *Nat. Phys.* **11,** 118–123 (2015).
17. Landauer, R. Irreversibility and heat generation in the computing process. *IBM J. Res. Dev.* **5,** 183–191 (1961).
18. Bérut, A. *et al.* Experimental verification of Landauer's principle linking information and thermodynamics. *Nature* **483,** 187–189 (2012).
19. Herr, Q. P., Herr, A. Y., Oberg, O. T. & Ioannidis, A. G. Ultra-low-power superconductor logic. *J. Appl. Phys.* **109,** 103903 (2011).
20. Kuhn, K. J. *et al.* The ultimate CMOS device and beyond. *IEEE Int. Electron Device Meet.* 8.1.1-8.1.4 (2012).
21. Jeong, W., Kim, K., Kim, Y., Lee, W. & Reddy, P. Characterization of nanoscale temperature fields during electromigration of nanowires. *Sci. Rep.* **4,** 4975 (2014).
22. Menges, F., Riel, H., Stemmer, A., Dimitrakopoulos, C. & Gotsmann, B. Thermal transport into graphene through nanoscopic contacts. *Phys. Rev. Lett.* **111,** 205901 (2013).
23. Worbes, L., Hellmann, D. & Kittel, A. Enhanced near-field heat flow of a monolayer dielectric island. *Phys. Rev. Lett.* **110,** 134302 (2013).
24. Yu, Y. *et al.* High-resolution spatial mapping of the temperature distribution of a Joule self-heated graphene nanoribbon. *Appl. Phys. Lett.* **99,** 183105 (2011).
25. Dubi, Y. & Di Ventra, M. Colloquium: Heat flow and thermoelectricity in atomic and molecular junctions. *Rev. Mod. Phys.* **83,** 131–155 (2011).
26. Chung, J. *et al.* Quantitative temperature measurement of an electrically heated carbon nanotube using the null-point method. *Rev. Sci. Instrum.* **81,** 114901 (201AD).
27. Faivre, T., Golubev, D. & Pekola, J. P. Josephson junction based thermometer and its application in bolometry Josephson junction based thermometer and its application in bolometry. *J. Appl. Phys.* **116,** 94302 (2014).
28. Vasyukov, D. *et al.* A scanning superconducting quantum interference device with single electron spin sensitivity. *Nat. Nanotechnol.* **8,** 639–44 (2013).
29. Finkler, A. *et al.* Self-aligned nanoscale SQUID on a tip. *Nano Lett.* **10,** 1046–1049 (2010).

30. Halbertal, D. *et al.* Nanoscale thermal imaging of dissipation in quantum systems. *Nature* **539,** 407–410 (2016).
31. Finkler, A. *et al.* Scanning superconducting quantum interference device on a tip for magnetic imaging of nanoscale phenomena. *Rev. Sci. Instrum.* **83,** 73702 (2013).
32. Huber, M. E. *et al.* DC SQUID series array amplifiers with 120MHz bandwidth (corrected). *IEEE Trans. Appl. Supercond.* **11,** 4048–4053 (2001).
33. Lachman, E. O. *et al.* Visualization of superparamagnetic dynamics in magnetic topological insulators. *Sci. Adv.* **1,** e1500740 (2015).
34. Schwab, K., Henriksen, E. A., Worlock, J. M. & Roukes, M. L. Measurement of the quantum of thermal conductance. *Nature* **404,** 974–7 (2000).
35. Ovadia, M., Kalok, D., Sacepe, B. & Shahar, D. Duality symmetry and its breakdown in the vicinity of the superconductor-insulator transition. *Nat. Phys.* **9,** 415–418 (2013).
36. Embon, L. *et al.* Probing dynamics and pinning of single vortices in superconductors at nanometer scales. *Sci. Rep.* **5,** 1–9 (2014).
37. Anahory, Y. *et al.* Three-Junction SQUID-on-Tip with Tunable In-Plane and Out-of- Plane Magnetic Field Sensitivity. *Nano Lett.* **14,** 6481–6487 (2014).
38. Anahory, Y. *et al.* Emergent nanoscale superparamagnetism at oxide interfaces. *Nat. Commun.* **7,** (2016).
39. Pollack, G. L. Kapitza resistace. *Rev. Mod. Phys.* **41,** 48–81 (1969).
40. Mate, C. F. & Sawyer, S. P. Kapitza effect in gaseous helium. *Phys. Rev. Lett.* **20,** 834–837 (1968).
41. Kennard, E. H. *Kinetic theory of gases*. (McGraw-Hill book co. Inc., 1938).
42. Horowitz, M., Silvidi, A. A., Malaker, S. F. & Daunt, J. G. The specific heat of lead in the temperature range 1°K to 75°K. *Phys. Rev.* **88,** 1182–1186 (1952).
43. Shadmi, N., Geblinger, N., Ismach, A. & Joselevich, E. Formation of ordered vs disordered carbon nanotube serpentines on anisotropic vs isotropic substrates. *J. Phys. Chem.* **118,** 14044–14050 (2014).
44. Woodside, M. T. & McEuen, P. L. Scanned probe imaging of single-electron charge states in nanotube quantum dots. *Science* **296,** 1098–1101 (2002).
45. Devoret, M. H. & Grabert, H. Single charge tunneling: Coulomb blockade phenomena in nanostructures. in *Nato Science Series B, Vol. 294* (Springer, 2013).
46. Castro Neto, A. H., Guinea, F., Peres, N. M. R., Novoselov, K. S. & Geim, A.

K. The electronic properties of graphene. *Rev. Mod. Phys.* **81,** 109–162 (2009).

47. Bistritzer, R. & Macdonald, A. H. Electronic cooling in graphene. *Phys. Rev. Lett.* **102,** 206410 (2009).
48. Tse, W. K. & Das Sarma, S. Energy relaxation of hot Dirac fermions in graphene. *Phys. Rev. B* **79,** 235406 (2009).
49. Song, J. C. W., Reizer, M. Y. & Levitov, L. S. Disorder-assisted electron-phonon scattering and cooling pathways in graphene. *Phys. Rev. Lett.* **109,** 106602 (2012).
50. Halbertal, D. *et al.* Imaging and controlling dissipation from individual atomic defects in graphene. *Under Rev.* (2017).
51. Pereira, V. M., Guinea, F., Lopes dos Santos, J. M. B., Peres, N. M. R. & Castro Neto, A. H. Disorder induced localized states in graphene. *Phys. Rev. Lett.* **96,** 36801 (2006).
52. Boukhvalov, D. W., Katsnelson, M. I. & Lichtenstein, A. I. Hydrogen on graphene: Electronic structure, total energy, structural distortions and magnetism from first-principles calculations. *Phys. Rev. B* **77,** 35427 (2008).
53. Wehling, T. O., Katsnelson, M. I. & Lichtenstein, A. I. Impurities on graphene: Midgap states and migration barriers. *Phys. Rev. B* **80,** 85428 (2009).
54. Shytov, A. V., Abanin, D. A. & Levitov, L. S. Long-range interaction between adatoms in graphene. *Phys. Rev. Lett.* **103,** 16806 (2009).
55. Gonzales-Herrero, H. *et al.* Atomic-scale control of graphene magnetism by using hydrogen atoms. *Science* **352,** 437–441 (2016).
56. Mao, J. *et al.* Realization of a tunable artificial atom at a supercritically charged vacancy in graphene. *Nat. Phys.* **12,** 545–550 (2016).
57. Ni, Z. H. *et al.* On resonant scatterers as a factor limiting carrier mobility in graphene. *Nano Lett.* **10,** 3868–3872 (2010).
58. Titov, M., Ostrovsky, P. M., Gornyi, I. V., Schuessler, A. & Mirlin, A. D. Charge transport in graphene with resonant scatterers. *Phys. Rev. Lett.* **104,** 76802 (2010).
59. Dean, C. R. *et al.* Boron nitride substrates for high-quality graphene electronics. *Nat. Nanotechnol.* **5,** 722–726 (2010).
60. Mayorov, A. S. *et al.* Micrometer-scale ballistic transport in encapsulated graphene at room temperature. *Nano Lett.* **11,** 2396–2399 (2011).
61. Bandurin, D. A. *et al.* Negative local resistance caused by viscous electron backflow in graphene. *Science* **351,** 1055–1058 (2016).

62. Zhu, M. J. *et al.* Edge currents shunt the insulating bulk in gapped graphene. *Nat. Commun.* **8,** 14552 (2017).
63. Wong, D. *et al.* Characterization and manipulation of individual defects in insulating hexagonal boron nitride using scanning tunnelling microscopy. *Nat. Nanotechnol.* **10,** 949–953 (2015).
64. Martin, J. *et al.* Observation of electron-hole puddles in graphene using a scanning single electron transistor. *Nat. Phys.* **4,** 144–148 (2008).
65. Tao, C. *et al.* Spatially resolving edge states of chiral graphene nanoribbons. *Nat. Phys.* **7,** 616–620 (2011).
66. Dauber, J., Terres, B., Volk, C., Trellenkamp, S. & Stampfer, C. Reducing disorder in graphene nanoribbons by chemical edge modification. *Appl. Phys. Lett.* **104,** 83105 (2014).
67. Georgakilas, V. *et al.* Functionalization of graphene: Covalent and non-covalent approaches, derivatives and applications. *Chem. Rev.* **112,** 6156–6214 (2012).
68. Bischoff, D. *et al.* Localized charge carriers in graphene nanodevices. *Appl. Phys. Rev.* **2,** 31301 (2015).
69. Garcia, A. G. F., König, M., Goldhaber-Gordon, D. & Todd, K. Scanning gate microscopy of localized states in wide graphene constrictions. *Phys. Rev. B* **87,** 85446 (2013).
70. Han, M. Y., Brant, J. C. & Kim, P. Electron transport in disordered graphene nanoribbons. *Phys. Rev. Lett.* **104,** 56801 (2010).
71. Jung, S. *et al.* Evolution of microscopic localization in graphene in a magnetic field from scattering resonances to quantum dots. *Nat. Phys.* **7,** 245–251 (2011).
72. Bischoff, D., Libisch, F., Burgdörfer, J., Ihn, T. & Ensslin, K. Characterizing wave functions in graphene nanodevices: Electronic transport through ultrashort graphene constrictions on a boron nitride substrate. *Phys. Rev. B* **90,** 115405 (2014).
73. Evaldsson, M., Zozoulenko, I. V., Xu, H. & Heinzel, T. Edge-disorder-induced Anderson localization and conduction gap in graphene nanoribbons. *Phys. Rev. B* **78,** 161407 (2008).
74. Gallagher, P., Todd, K. & Goldhaber-gordon, D. Disorder-induced gap behavior in graphene nanoribbons. *Phys. Rev. B* **81,** 115409 (2010).
75. Martin, I. & Blanter, Y. M. Transport in disordered graphene nanoribbons.

Phys. Rev. B **79,** 235132 (2009).

76. Pieper, A., Schubert, G., Wellein, G. & Fehske, H. Effects of disorder and contacts on transport through graphene nanoribbons. *Phys. Rev. B* **88,** 195409 (2013).
77. Allen, M. T. *et al.* Spatially resolved edge currents and guided-wave electronic states in graphene. *Nat. Phys.* **12,** 128–133 (2016).
78. Chae, J. *et al.* Enhanced carrier transport along edges of graphene devices. *Nano Lett.* **12,** 1839–1844 (2012).
79. Landau, L. D. & Lifshitz, E. M. *Course of theoretical physics volume 9: Statistical physics part 2*. *Pergamon* (1980).
80. Landau, L. D. & Lifshitz, E. M. *Course of theoretical physics volume 5: Statistical physics part 1*. (Butterworth-Heinemann, 1980).
81. Meschke, M., Guichard, W. & Pekola, J. P. Single-mode heat conduction by photons. *Nature* **444,** 187–190 (2006).
82. Jezouin, S. *et al.* Quantum limit of heat flow across a single electronic channel. *Science* **342,** 601–604 (2013).
83. Gyory, E. & Márkus, F. Size dependent thermal conductivity in nano-systems. *Thin Solid Films* **565,** 89–93 (2014).
84. Balandin, A. A. Thermal properties of graphene and nanostructured carbon materials. *Nat. Mater.* **10,** 569–581 (2011).
85. Zeller, R. C. & Pohl, R. O. Thermal conductivity and specific heat of non-crystalline solids. *Phys. Lett. B* **4,** 2029–2041 (1971).
86. Xue, J., Dhall, R., Cronin, S. B. & Leroy, B. J. Scanning gate microscopy of ultra clean carbon nanotube quantum dots. *arXiv preprint* arXiv:1508.05462 (2015). at <http://arxiv.org/pdf/1508.05462v1.pdf>
87. Schnez, S., Guttinger, J., Stampfer, C., Ensslin, K. & Ihn, T. The relevance of electrostatics for scanning-gate microscopy. *New J. Phys.* **13,** 53013 (2011).
88. Huefner, M. *et al.* Spatial mapping and manipulation of two tunnel-coupled quantum dots. *Phys. Rev. B* **83,** 235326 (2011).

6 List of publications derived from the doctoral research

1. **Halbertal, D.**, Cuppens, J., Ben Shalom, M., Embon, L., Shadmi, N., Anahory, Y., Naren, H. R., Sarkar, J., Uri, A., Ronen, Y., Myasoedov, Y., Levitov, L. S., Joselevich, E., Geim, A. K. & Zeldov, E. 'Nanoscale thermal imaging of dissipation in quantum systems', *Nature* **539**, 407–410 (2016), doi:10.1038/nature19843.
2. **Halbertal, D.**, Ben Shalom, M., Uri, A., Bagani, K., Meltzer, A. Y., Myasoedov, Y., Birkbeck, J., Levitov, L. S., Geim, A. K. & Zeldov, E., 'Imaging and controlling dissipation from individual atomic defects in graphene'. Submitted (2017).